The Pennsylvania State University

The Graduate School

The Graduate Program in Acoustics

SYNTHETIC APERTURE SONAR IMAGE STATISTICS

A Dissertation in

Acoustics

by

Shawn F. Johnson

Submitted in Partial Fulfillment
of the Requirements
for the Degree of

Doctor of Philosophy

May 2009

The dissertation of Shawn F. Johnson was reviewed and approved* by the following:

Anthony P. Lyons
Professor of Acoustics
Senior Scientist
Dissertation Advisor
Chair of Committee

Karl M. Reichard
Assistant Professor of Acoustics
Research Associate

Ram M. Narayanan
Professor of Electrical Engineering

Timothy J. Kane
Professor of Electrical Engineering

Anthony A. Atchley
Professor of Acoustics
Associate Dean of Engineering
Head of the Graduate Program in Acoustics

*Signatures are on file in the Graduate School

ABSTRACT

Synthetic Aperture Sonar (SAS) systems are capable of producing photograph quality seafloor imagery using a lower frequency than other systems of comparable resolution. However, as with other high-resolution sonar systems, SAS imagery is often characterized by heavy-tailed amplitude distributions which may adversely affect target detection systems. The constant cross-range resolution with respect to range that results from the synthetic aperture formation process provides a unique opportunity to improve our understanding of system and environment interactions, which is essential for accurate performance prediction. This research focused on the impact of multipath contamination and the impact of resolution on image statistics, accomplished through analyses of data collected during at-sea experiments, analytical modeling, and development of numerical simulations. Multipath contamination was shown to have an appreciable impact on image statistics at ranges greater than the water depth and when the levels of the contributing multipath are within 10 dB of the direct path, reducing the image amplitude distribution tails while also degrading image clarity. Image statistics were shown to depend strongly upon both system resolution and orientation to seafloor features such as sand ripples. This work contributes to improving detection systems by aiding understanding of the influences of background (*i.e.* non-target) image statistics.

TABLE OF CONTENTS

LIST OF FIGURES

LIST OF TABLES

ACKNOWLEDGEMENTS

The following pages represent the culmination (thus far) of six years of work. As with many research projects, the end destination was arrived at by way of several tangents with new questions and explorations along the way. Albert Einstein said it best, "If we knew what we were doing, it wouldn't be called research. Would it?" There are several groups and specific people that have helped through this process that deserve my thanks:

With much gratitude I acknowledge my thesis advisor, Dr. Anthony P. Lyons. His foresight concerning an emerging technology and interest in statistics enabled me to enter on the 'ground floor' of a topic that is presently of much interest in the field. His support and encouragement to participate in unique opportunities has enabled me to be a contributing member of our society while still a student. The assistance of Dr. Douglas A. Abraham has been instrumental in developing the statistical methods presented here and in several co-authored publications. Thank you to Dan Brown for his assistance improving beamforming algorithms and several inspiring conversations. I also thank my other committee members for challenging me during the dissertation process, and lending their expertise and advice.

Thank you to Dr. Kevin Williams and others at the Applied Physics Lab – University of Washington for the use of their SAS data from the SAX04 experiment. Thank you to Dr. Kerry Commander and others at Naval Surface Warfare Center –

Panama City for the use of SSAM data. These two data sets made validation of the modeling methods, presented in this thesis possible, and provided unique opportunities to explore the interplay of Sonar and the environment.

I also gratefully acknowledge the financial support of the National Defense Science and Engineering Graduate Fellowship, the National Defense Industrial Association, the Office of Naval Research Code 32, and the Applied Research Laboratory at the Pennsylvania State University. Also, thank you to the professors and staff of the Graduate Program in Acoustics and the Environmental Acoustics Group at the Applied Research Laboratory for promoting and enabling a fantastic program.

Most importantly I acknowledge my parents, whose loving support has made this endeavor possible. For their financial sacrifice to enable my education, and always being available to lend positive advice when the task seemed insurmountable, I am forever indebted.

"The common goal in this noise inquiry is to see more noise patterns as signals… This change in perspective involves a step up in understanding… Insight grows along with an implied signal-to-noise ratio when more noise counts as signal. The shift from noise to signal starts at birth and continues throughout life. Thousands of sensory signals impinge on a newborn child but the child sees and hears and feels and tastes many of these as noise. An adult perceives most of the same signals as legitimate signals unto themselves. A physician or other expert sees even more signal structure in the same swath of experience. And so it goes up the ladder of insight – to God all is signal."

~Bart Kosko in *Noise*

Chapter 1

Introduction and Background

1.1 Thesis Overview

Images produced with a high-resolution Synthetic Aperture Sonar (SAS) often resemble a photograph of the seafloor (Figure 1.1), with recognizable structures such as sand ripples, beds of seagrass, rocks, or man-made objects. While these features may produce shapes observable in the data which we associate with known structures, as with any remote sensing technique it is necessary to consider the mechanisms producing them. Just as a photograph is a two-dimensional incoherent record of scattered optical energy, a SAS image is a coherent record of scattered acoustical energy. This recorded energy, whatever the source, is influenced by the source characteristics, propagation through the environment, scattering properties of the object(s), receiver characteristics, and any processing done to record, reproduce, or enhance the image. For the case of a camera, these components are a function of the directionality and frequency spectrum of the flash or ambient light, medium composition (and possible interactions with boundaries or near-by objects), optical scattering properties of the objects being imaged, the camera lens, digitization and reproduction, and image enhancement. For the case of a SAS system, these components are a function of the source beampattern and transmitted spectrum, water properties and composition (and possible interactions with boundaries such as the sea-surface or sea-floor), acoustic scattering properties of the objects being imaged, the

Figure 1.1: Example Synthetic Aperture Sonar image. [1]

[1] The color-scale in this and subsequent figures represents a contrast-modified representation of backscattered acoustic amplitude. Contrast modification is commonplace in remote sensing, and involves changing the shape of an image pixel amplitude histogram for improved visual interpretation on various display formats (*i.e.* print and computer displays) with a significantly narrower dynamic range compared to the dynamic range of the remote sensing system [Rees 2001]. Unless otherwise stated, the image histograms here have been scaled to the Gamma distribution as in [Cook 2007].

receiver beam pattern and frequency response, digitization and display, and the synthetic aperture formation process. Keeping this in mind, extreme care must be used when making determinations about what these images represent. To further complicate matters, remote sensing often encounters the problem of randomness of the source, channel, and noise[2], forcing a dependence upon statistics [Van Trees 1968, Urick 1983]. Assumptions are made to manage the randomness [Bennett 1956] of Sonar (or Radar or optic systems) based object detection and classification.

A major limitation of active Sonar is the False Alarm rate (FAR) [Gaumond et al. 2008], which is when a target detection system identifies a non-target signal as a target. When this detected non-target signal is caused by the response of the environment, it is termed clutter. Traditionally the normalized match-filtered Sonar reverberation envelope

---

[2] Here we take the term 'noise' to mean the combination of reverberation, instrument noise, and background noise. Hereafter, clearer distinctions of 'reverberation' of an active transmission separate from background ambient 'noise' will be made, with instrument noise considered nominal and excluded for the discussion here. The term 'clutter' is taken to mean false target-like reverberation returns.

Probability Density has been modeled as a Rayleigh distribution, with justification based on the Central Limit Theorem [Urick 1983, Abraham 1997, Bisceglie et al. 1999, Burdic 2002, Abraham & Lyons 2002a, Lurton 2004]. However more recent studies continue to report data collected with high-resolution systems exhibiting, and theoretical studies predicting, tails that are significantly heavier than the Rayleigh distribution [Jakeman & Pusey 1976, Crowther 1980, Chotiros *et al.* 1985, McDaniel 1990, Middleton 1999]. Reverberation statistics have been shown to depend on both the system parameters as well as the operating environment; the former is dominated by array beam width and transmit-waveform bandwidth, while the latter is impacted through acoustic scattering and propagation [Lyons & Abraham 1999, Abraham & Lyons 2002a, Abraham & Lyons 2002b, Abraham & Lyons 2004a, Johnson et al. 2005, Abraham & Johnson 2008, Johnson et al. 2008, Lyons et al. 2009].

As the sophistication of, and the demands on such systems to perform in potentially complicated environments increases, so too does the necessity of a priori knowledge to accurately predict their performance. Quantifying physical mechanisms affecting Sonar systems is essential for understanding collected information, advancement of image processing and detection algorithms for both objects and background textures and increasing general image quality (*i.e.* increasing resolution and reducing speckle). Traditional assumptions originally postulated from theory and prior observation may no longer be valid and should be re-examined utilizing current technology in actual operating environments, with the goal of optimizing Sonar system performance through intelligent system parameter design. Further, it is often necessary to

develop *in silico* methods (*i.e.* computer based) when *in situ* methods (*i.e.* at-sea) are unfeasible or prohibited for any of a number of reasons. This requires a physical understanding of both the object of interest and the environment, and how the system parameters interact with both.

This thesis focuses on analysis and simulation of high-resolution SAS imagery characterized by heavy-tailed amplitude distributions which often adversely affect Sonar based target detection systems. The remainder of this chapter introduces Synthetic Aperture Sonar theory and history, followed by a discussion on the role of statistics in Sonar and the impact of heavy-tailed amplitude distributions on target detection algorithms. Chapter 2 describes two at-sea SAS experiments which serve as the basis of this work, followed by the general data analysis and simulations methods used. Chapter 3 focuses on the impact of multipath and Chapter 4 on the impact of resolution on SAS image statistics, with a discussion of data analysis and simulation methods specific to each case. Conclusions and suggestions for future work are given in Chapter 5.

1.2 Synthetic Aperture Sonar

Synthetic Aperture Sonar (SAS) is to acoustics what Synthetic Aperture Radar (SAR) is to electromagnetism. The fundamental idea behind both types of synthetic aperture processing is that the cross-range resolution of the remote sensing system, and subsequently the ability to observe and discern features in the data collected with the systems, is proportional to the size of the aperture. Recalling the camera analogy from

the previous section, the resolution[3] of a photographic image is bounded by the size of the aperture of the lens (one reason of several why the large-aperture cameras chosen by professionals produce clearer pictures over the smaller-aperture point-and-shoot variety, and why telescopes have extremely large lenses). Similarly in traditional Sonar and Radar systems, better directionality (*i.e.* a narrower beampattern) and thereby resolution is achieved by implementing a larger aperture. An excellent presentation of the development of resolution theory can be found in [Hawkins 1996, Soumekh 1999] which serves as the basis for this section. We begin first with the mathematical derivation of synthetic aperture resolution, followed by a brief history.

[3] High-resolution meaning pixels with a small area (*i.e.* small Δx and Δy).

1.2.1 Resolution of Traditional Aperture and Synthetic Aperture

The slant-range resolution (Δx_{slant}) for both traditional and synthetic aperture systems is defined as:

$$\Delta x_{slant} = a_{wx} \frac{c\,\tau}{2} = a_{wx} \frac{c}{2\,BW_{lfm}} \qquad \text{Equation 1.1}$$

where τ is the pulse-length and BW_{lfm} is the bandwidth of the transmitted chirp [Hawkins 1996, Burdic 2002, Lurton 2004, Jensen 2008]. Although linear frequency modulation chirps are traditionally used, several other broadband signals can be used without losing generality (*e.g.*,. hyperbolic, stepped-sine, or noise). The term a_{wx} is a constant representing windowing or weighting applied to control side-lobes in the slant-range dimension (*i.e.* along the *x*-axis). From [Harris 1978], a_{wx} = 0.89 (rectangular) and 1.30 (Hamming).

For a line array (traditional aperture) situated along the *y*-axis, the directivity pattern ($D(\theta_y)$) is defined as:

$$D(\theta_y) = \left(\frac{\sin A}{A} \right)^2, \qquad \text{Equation 1.2}$$

where:

$$A = \left(\frac{\pi L}{\lambda} \right) \sin \theta_y \qquad \text{Equation 1.3}$$

with an angular main-lobe width ($\theta_{y\,3dB}$) measured at the 3 dB down-points of:

$$\theta_{y\,3dB} = a_{wy} \frac{\lambda}{L} = a_{wy} \frac{c}{f L} \qquad \text{Equation 1.4}$$

for $L > \lambda$ where θ is the receive angle relative to the normal of the aperture, λ is the wavelength, f is frequency, and L is the aperture length. Again, the a_{wy} is a constant representing windowing or weighting applied to control side-lobes, this time in the cross-range dimension (*i.e.* along the *y*-axis). One can see that as the aperture length increases the main lobe width decreases. The cross-range resolution (Δy_{line}) is given by:

$$\Delta y_{line} = x_{slant}\, \theta_{y\,3dB} = a_{wy} \frac{c\, x_{slant}}{f L} \qquad \text{Equation 1.5}$$

where x_{slant} is the slant-range. Here it is noted for a fixed aperture the resolution width grows with range, or to maintain a constant resolution width the aperture must be increased proportional to range. In many cases the maximum aperture length, and thereby resolution, are limited either financially or mechanically. Large sensors with suitable properties can be very costly to produce or may be too fragile.

The synthetic aperture formation process produces images with fixed cross-range (*i.e.* along-track) resolution, which contrasts the range-dependent cross-range resolution width demonstrated in Equation 1.5. This is accomplished by post-processing echoes received from a moving smaller physical aperture to synthetically create a larger aperture which has the property of increasing with range, thereby resulting in an image with fixed cross-range resolution. A complete understanding of synthetic aperture cross-range resolution requires consideration of the process itself; a brief explanation is given in the next section and simplified analysis is presented here, with complete development available in numerous sources, such as: [Carrara et al. 1995, Hawkins 1996, Soumekh 1999, Cumming & Wong 2005].

The cross-range resolution of synthetic aperture is directly proportional to the bandwidth of the temporal (or spatial) Doppler induced by motion of the physical aperture. Considering the beamwidth of Equation 1.4, the dwell time (τ_d) of a point at x_0 (or time ensonified by the acoustic beam) is:

$$\tau_d \approx \frac{x_0 \theta_{y\,3dB}}{v_p} = \frac{x_0 \lambda_0}{v_p} = \frac{2\pi x_0}{k_0 v_p L} \qquad \text{Equation 1.6}$$

where k_0 and λ_0 are the wavenumber and wavelength of the carrier frequency f, and v_p is the velocity of the physical aperture along the y-axis. The phase (φ) from a point at range x_0 at along-track position u is:

$$\varphi(u) \approx -2k_0\left(x_0 + \frac{u^2}{2x_0}\right) \qquad \text{Equation 1.7}$$

and differentiation with respect to the slow-time (along-track) variable (t_{at}):

$$t_{at} = \frac{u}{v_p} \qquad \text{Equation 1.8}$$

results in:

$$f_{dr} = \frac{k_0 v_p^2}{\pi x_0}, \qquad \text{Equation 1.9}$$

which is the Doppler rate (f_{dr}) of the pulse. The Doppler bandwidth (BW_D) is then:

$$BW_D \approx 2\frac{k_0 v_p^2}{\pi x_0}\frac{\pi x_0}{k_0 v_p L} = \frac{2v_p}{L}, \qquad \text{Equation 1.10}$$

and after along-track compression (matched filtering) yields the along-track spatial resolution ($\Delta_{ySAS\ 3dB}$):

$$\Delta y_{SAS\,3dB} \approx \frac{v_p}{BW_D} = \frac{L}{2}. \qquad \text{Equation 1.11}$$

Equation 1.11 is the classical interpretation of synthetic aperture cross-range resolution developed from the along-track beampattern 3 dB down-points. Typical design of a synthetic aperture system considers the two-way propagation time of the echo and velocity of the physical aperture to determine the pulse-repetition frequency, so that the along-track pulse spacing (Δu) is:

$$\Delta u \approx \Delta y_{SAS\,3dB}. \qquad \text{Equation 1.12}$$

As will be discussed in more detail in Chapter 4, the resolution of a synthetic aperture image can be reduced for enhanced properties. Images produced using the classical cross-range resolution may exhibit grating lobes (*i.e.* when energy from the beampattern side-lobes is aliased into the main-lobe) and a more conservative approach is to sample the along-track dimension at twice the original pulse-repetition rate, or decrease the pulse spacing by a factor of two, so that there are two samples per $\Delta y_{SAS\,3dB}$ [Hawkins 1996, Gough & Hawkins 1997a, Callow 2003]. The cross-range resolution set to minimize grating-lobes is then:

$$\Delta y_{SAS} \approx \frac{\Delta u}{2} \approx \frac{L}{4}, \qquad \text{Equation 1.13}$$

which is the convention adopted in this work. From either Equation 1.11 or 1.13, one can see that the cross-range resolution of synthetic aperture does not depend on range or transmitted frequency as it does for traditional aperture. In fact for synthetic aperture, smaller physical apertures yield greater image resolution – a principle that is completely opposite of traditional aperture. However, this is achieved at the expense of computational time and required resources.

1.2.2 Synthetic Aperture History, Reconstruction Theory, and Algorithms

Carl Wiley demonstrated a technique termed Doppler Beam Sharpening with improved along-track resolution in 1951 [Sherwin et al. 1962, Wiley 1985]. This technique utilizes the Doppler shifts observed in forward-looking (squinted) pulsed Radar data, and Wiley is thereby credited with inventing Synthetic Aperture Radar, the term referring to treating the sequences of pulses from moving real aperture as a much longer 'synthetic' array. In 1948, Dennis Gabor presented a theory of wave-front reconstruction (a sort of inverse Huygens-Fresnel principle) for microscopy, and is the basis of holography [Gabor 1972]. The technique was thought to be of 'dubious' practicality and confined to a narrow branch of science [Johnston 2005]. Partially restricted by technology of the time [Steward 2004], wave-front reconstruction was renewed in the 1960's and eventually earned Gabor the Nobel Prize for Physics in 1971. Since, it has been the basis for several coherent imaging techniques in geophysics, optics, diagnostic medicine, Radar, and Sonar [Soumekh 1999]. The principle of wave-front reconstruction is exemplified in the word holography itself, coming from the Greek roots of *holos*

meaning ‘whole’ and *grafe* meaning ‘drawing’. Restated, a hologram is a coherent recoding of an image from several angles. In practice for Radar and Sonar, a single sensor is moved along a path making multiple measurements, with post-processing of the individual echo waveforms creating an effective aperture equal in length to the path traversed. Several caveats exist, specifically an accurate record of the fine-scale motion of the sensor for motion compensation, and sufficient spatial sampling along the path. An additionally requirement which contradicts traditional resolution reasoning is the sensor should exhibit a wide beampattern along the dimension of travel (this is so the ‘hologram’ image produced contains information from many angles, requiring a large beamwidth before synthetic aperture formation), as can be seen from the development of Equations 1.11 and 1.13 in the previous section.

The fundamental obstacle to synthetic aperture formation using wave-front reconstruction is mitigating the position-induced temporal- or spatial-Doppler. For the methods presented here, a start-stop assumption is made as the sensor is moving relatively slowly compared to the propagation speed such that temporal-Doppler is negligible, however the principals are analogous. This position-induced spatial-Doppler is sometimes referred to as the Point Spread Function (PSF). An example showing the amplitude component of the PSF is depicted in Figure 1.2, with the pulse-compressed data on the left and image after synthetic aperture formation on the right. The ‘potato-chip’ shape results from the acoustic beam moving past the point target, with the apex of the image curvature being when the sensor is directly in line with the point target. This spatial-Doppler is corrected for by modifying both amplitude and phase, followed by

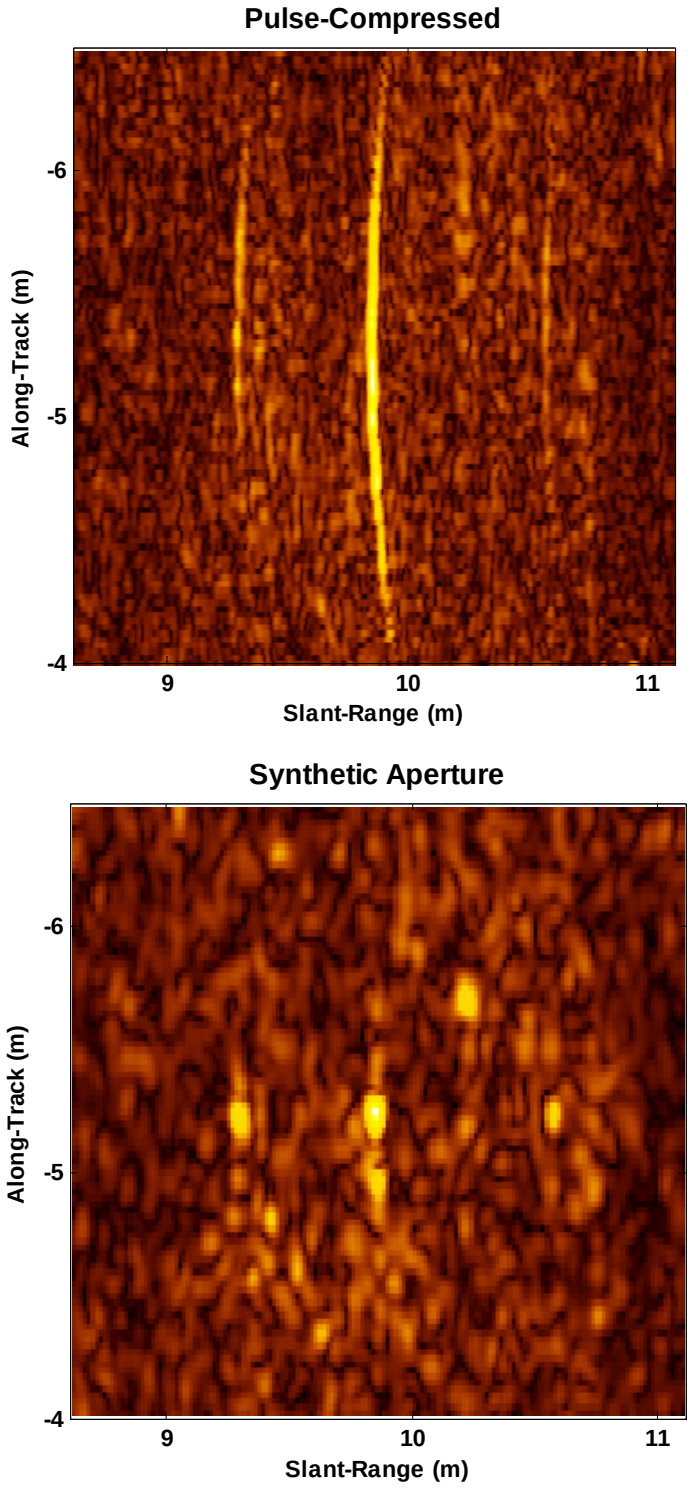

Figure 1.2: Flush-buried sphere as imaged before (top) and after (bottom) removal of point spread function with inverse Stolt-mapping.

coherent summation along the PSF of each pixel to produce a synthetic aperture image. Early SAR systems recorded electromagnetic reflectivity on films in-flight, and the PSF was accounted for in the laboratory optically by illuminating these films with lasers and focusing with lenses onto additional films. The PSF can be compensated for *in silico* with the advent of digital processing, and several methods for doing such have gained and lost popularity over the years mainly based on computational horse-power required. The launch of the SEASAT oceanographic satellite in 1978 spurred an effort to develop digital SAR processors [Cumming & Wong 2005] (processing a 1600 km2 image with 25 m resolution took 40 hours! [Bennett et al. 1979]). The notable methods include: spatial-temporal, fast-correlation, range-Doppler, chirp scaling, and the method used for rendering the images presented here, wavenumber inversion.

In 1978 Stolt described 'Seismic Migration by Fourier transform' [Stolt 1978, Carrara et al. 1995, Soumekh 1999, Cumming & Wong 2005] which is perhaps the most mathematically elegant method of all PSF compensations. Seismic migration or Stolt-mapping is also known as ωk and wavenumber inversion. Wave-front reconstruction is implemented utilizing the Fourier decomposition of a Green's function which is the impulse response of an imaging system, and is also known as the spherical phase function [Soumekh 1999]. In [Hawkins 1996], the technique was expanded and clarified for implementation with a towed, wide-bandwidth Synthetic Aperture Sonar. The Stolt-map, given by:

$$\omega\left(k_x, k_y\right) \equiv \frac{c}{2}\sqrt{k_x^{\,2} + k_y^{\,2}} \qquad \text{Equation 1.14}$$

and

$$k_u(k_x, k_y) \equiv k_y \qquad \text{Equation 1.15}$$

maps the spatial x (range or fast-time dimension) and y (along-track, cross-range, or slow-time dimension) wavenumbers (k_x and k_y respectively) into the measurement parameters of temporal frequency (ω) and along-track spatial wavenumber (k_u), where c is the speed of sound. The inverse Stolt-map is given by:

$$k_x(\omega, k_u) \equiv \sqrt{4k^2 - k_u^2} - 2k_0 \qquad \text{Equation 1.16}$$

and

$$k_y(\omega, k_u) \equiv k_u, \qquad \text{Equation 1.17}$$

which maps the measurements parameters (ω and k_u) to the spatial parameters (k_x and k_y), where k_0 the carrier wavenumber ($k_0 = w_0/c$), and k is distance from the carrier to the the specific k_x,k_y pair being mapped. It is this inverse Stolt-map which is used in the synthetic aperture formation process (Figure 1.3). Implementation of forward or inverse Stolt-mapping in discrete (*i.e.* digital) systems requires interpolation, which limited early implementation. The existence of the forward Stolt-map provides the ability to produce simulated measurement-space data from a synthetically formed image, albeit with possible interpolation and windowing errors.

Recent advances in fine-scale motion compensation [Bellettini & Pinto 2002, Cook et al. 2003, Cook et al. 2005, Cook 2007] have enabled the utilization of Autonomous Underwater Vehicles (AUV's) and the production of photograph-like Sonar images (positioning accuracy is typically required to be better than $\lambda/8$ [Jensen 2008]). We are now at the point with SAS that the SAR community was some 20 to 30 years ago, with the SAS community closing the gap quickly. A more complete history of synthetic aperture and Fourier imaging can be found in [Soumekh 1994, Carrara et al. 1995, Hawkins 1996, Gough & Hawkins 1997a, Gough & Hawkins 1997b, Soumekh 1999, Griffiths 2003, Cumming & Wong 2005, Goodman 2005] and the references contained therein.

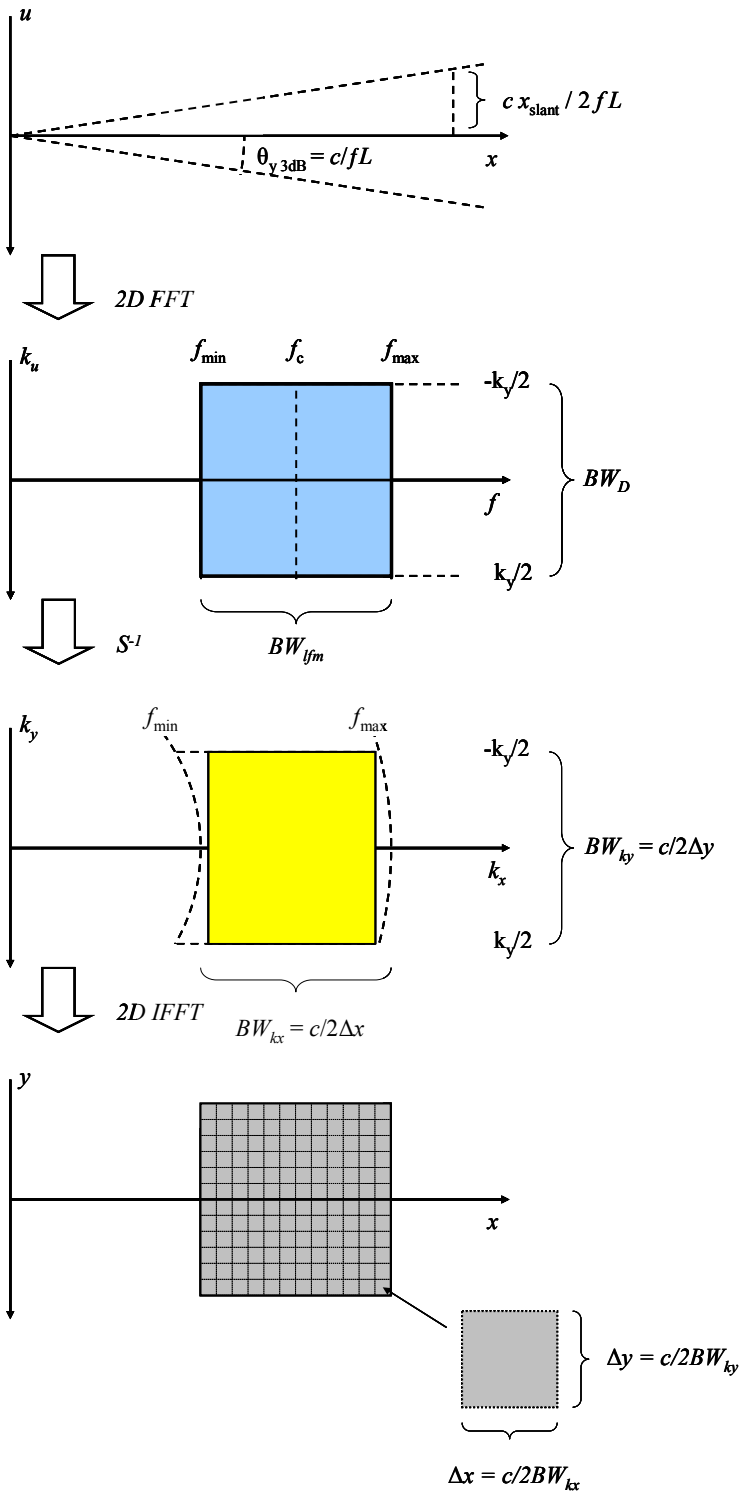

Figure 1.3: Diagram of the wavenumber synthetic aperture formation process.

1.3 Statistics for Sonar

The importance of statistics for Sonar can be summarized simply by two quotations from the popular Sonar literature.

> "Sonar signals, whether the echos of active Sonars or the target sounds of passive Sonars, must always be observed amid a background of noise or reverberation. … the system must first detect the presence of the signal in this background…" [Urick 1983]
>
> "Noise-like phenomena have the common property that we do not specify precisely what magnitudes are observed at what times… Whatever our motives, we resign ourselves to a statistical description…" [Bennett 1956]

These quotations combined state that we are uninterested in, or more realistically incapable of, prescribing a deterministic solution for the energy that will be received at a particular instant in time, mathematically accounting for every aspect of the remote-sensing process (the sources and scales of oceanic variability are significant topics in and of themselves). We are almost always relegated to a 'simplified' statistical description of the environment based upon a set of assumptions. To be valid (or even beneficial) these assumptions must be physically based on the environment being interrogated, coupled with understanding of the system being used.

As presented in [Van Trees 1968], signal processing in Sonar (and Radar) systems must consider four distinct parts:

(a) description of the reflective characteristics of the target,

(b) description of the effect of the transmission channels on the signals,

(c) characterization of interference (noise, reverberation/clutter, *etc.*), and

(d) design of an optimum receiver and evaluate the performance.

In this work, (a) is omitted entirely as we are considering only the process(es) causing reverberation in the absence of a target, while discussion of (d) is restricted to examples of the impact on energy detection. The focus of this work fall under topics (b) and (c): how SAS image statistics are impacted by multipath propagation and Sonar system resolution. While complete characterization of these will never be realized, work of this nature is significantly important to development and utilization of these systems and perhaps more importantly the understanding of the acoustic response of the environment.

1.3.1 Models of Reverberation

As stated previously, we are constrained to modeling the system response in a random environment with a statistical description. Specifically of interest in this work is the statistical description of the normalized matched-filter output envelope, which serves as the input to many target detection algorithms which will be discussed shortly. Several statistical models of reverberation have been put forth, some of which are very complex

with numerous parameters that may be adjusted to fit nearly any data that may be collected. While this flexibility has several merits, some have too many free parameters to be practical. It is acknowledged that a host of other possible statistical distributions can be used to mathematically model naturally occurring phenomenon (*e.g*., normal or Gaussian, log-normal, Weibull, Rayleigh mixture, generalized Gamma, generalized Pareto). The following discussion is limited to only two simple models: the Rayleigh distribution and the *K* distribution, which have been shown to well-describe a wide range of data [Crowther 1980, Chotiros *et al*. 1985, Lyons & Abraham 1999, Abraham & Lyons 2002a, Abraham & Lyons 2002b, Becker 2004, Preston & Abraham 2004, Abraham & Lyons 2004a, Johnson et al. 2005, Lyons *et al*. 2005, Jackson 2007, Johnson *et al*. 2008, Lyons *et al*. 2009].

1.3.1.1 The Rayleigh Distribution Assumption and Origins

In this section, justification for and subsequently the shortcomings of the traditionally assumed Rayleigh-distributed reverberation envelope are outlined. Beginning with the classical reverberation definition as reverberation (R) at time (t) being a sum of returns from discrete scatters with specified amplitude (A_m) and phase ($e^{-i\theta_m}$) being from the m^{th} of a total n ensonified scatterers:

$$R(t) = \sum_{m=1}^{n(t)} A_m e^{-i\theta_m} \qquad \text{Equation 1.18}$$

and applying the Central Limit Theorem (CLT), the infinite sum has the a Rayleigh-distributed Probability Density Function (PDF):

$$f(y) = \left(\frac{2y}{\lambda_0} \right) e^{\left(\frac{-y^2}{\lambda_0} \right)} \qquad \text{Equation 1.19}$$

where y is the matched-filtered envelope, and λ_0 is the power.

Two conditions, however, must be met to apply the Central Limit Theorem (CLT) assumption: scatterers must be independent and identically distributed (iid) spatially with a uniform distribution and the number of scatterers must be infinite [Peebles 2001, Papoulis & Pillai 2002]. Although an infinite number of scatterers is required for textbook application of the CLT, in practice scatterer numbers on the order of tens is often sufficient to simply match lower order moments [Bendat & Piersol 2000]. Shallow water environments frequently have seafloors that are spatially heterogeneous, caused by spatially varying geo-acoustic properties over the ensonified area. Processes such as bioturbation and wave action can generate spatial correlations on the seafloor such as pockmarks or sand ripples. Both heterogeneity and spatial correlations violate the iid condition of the CLT, while the small sonar resolution scales such as those achieved by SAS often violate the infinite-number-of-scatterers condition. Thus, non-Rayleigh reverberation should be anticipated in such scenarios, if not expected.

Figure 1.4 shows the probability density versus normalized amplitude for example experimental data collected during the Office of Naval Research (ONR) sponsored Sediment Acoustics eXperiment 2004 (SAX04). Data chosen for this figure come from a rippled sand seafloor as imaged by a 60-100 kHz SAS image, and is a typical example of a heavy-tailed distribution (*i.e.* the tail of the envelope distribution is heavier than a Rayleigh distribution, which is to say high amplitude events are more frequent). For this data, the tail is orders of magnitude greater for high normalized amplitudes than Rayleigh, and it is desirable to find an alternative model that more closely matches observed heavy-tailed reverberation. Also shown on Figure 1.4 is the Weibull distribution which has an adjustable shape parameter (b), estimated here using the maximum likelihood method to be b = 1.76. Visual examination illustrated the inability of both these distributions to adequately describe the probability of high-amplitude events of this particular high-resolution system.

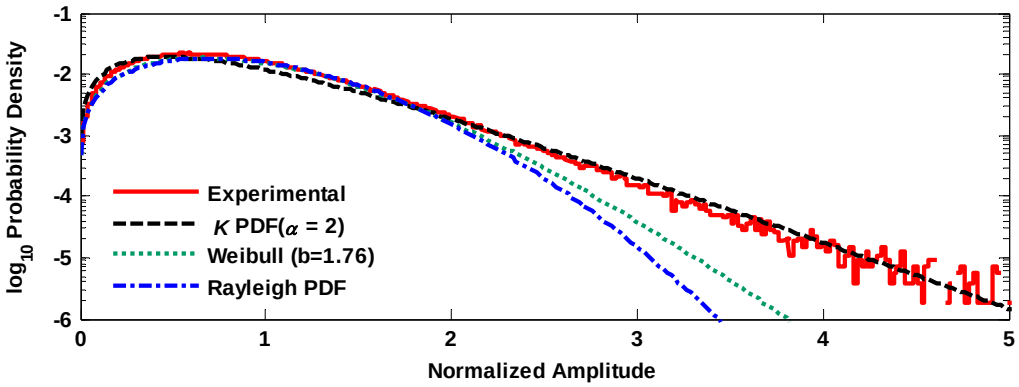

Figure 1.4: Normalized Amplitude Probability Density for 40 kHz bandwidth SAS image from SAX04.

1.3.1.2 The *K* Distribution

The *K* distribution has been used extensively for quantifying Radar clutter, optical propagation through turbulent media, and is quickly gaining acceptance in the underwater acoustics community. Heavy-tailed Sonar reverberation has been shown to be well fit by the *K* distribution, which contains a scale parameter and a shape parameter [Crowther 1980, Chotiros et al. 1985, McDaniel 1990, Abraham 1997, Lyons & Abraham 1999, Middleton 1999, Abraham & Lyons 2002b, Preston & Abraham 2004, Abraham & Lyons 2004a, Abraham & Lyons 2004b, Johnson et al. 2005, Lyons et al. 2005, Jackson 2007, Johnson et al. 2008, Lyons et al. 2009]. The PDF of the *K* distribution has the form:

$$f(y) = \frac{4}{\sqrt{\lambda}\,\Gamma(\alpha)}\left(\frac{y}{\sqrt{\lambda}}\right)^{\alpha} K_{\alpha-1}\left(\frac{2y}{\sqrt{\lambda}}\right) \qquad \text{Equation 1.20}$$

where y is the matched-filter envelope, α is the shape parameter, λ is the scale parameter, Γ is the Gamma function, K is the modified Bessel function of the second kind (sometimes referred to as the Basset or MacDonald function), and the power is $P = \alpha\lambda$. The shape parameter (α) allows for a good fit to a wide range of data; from heavy tailed distributions using a small value on the order of single digits, to near Rayleigh distributions for large values. As α tends to infinity while the power (P) is held constant, the *K* distribution simplifies to the Rayleigh distribution (Equation 1.19). Figure 1.5 shows increasing the shape parameter (α = 2→16) results in increasingly Rayleigh-like PDFs. It should be noted that two expressions for the *K* distribution appear in the

literature, one for amplitude detection (Equation 1.20) and a second for square law (i.e. intensity) detection; however, the statistics of the distributions are identical when the parameters are treated as constants [Dong 2004].

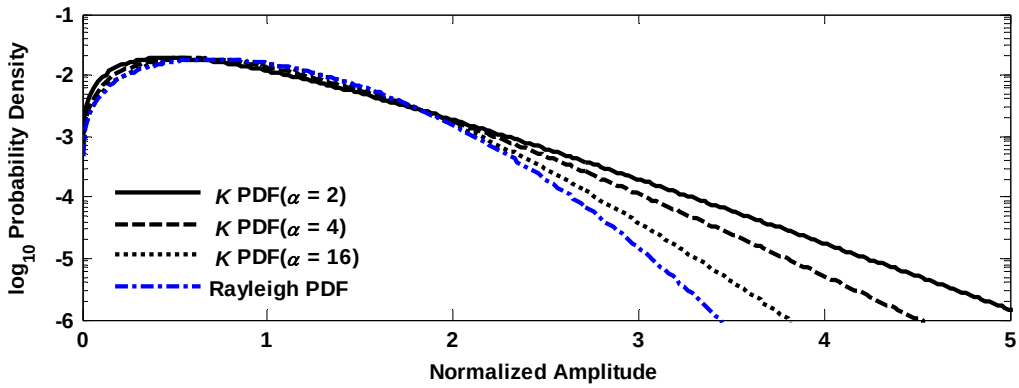

Figure 1.5: Normalized Amplitude Probability Density for *K* distributions of various shape parameters compared to the Rayleigh distribution.

It has been shown theoretically that the shape parameter of a *K* distribution matched to the reverberation envelope PDF is proportional to the effective number of scatterers within the Sonar's resolution cell [Abraham & Lyons 2002b]. Data analysis has also confirmed that within certain physical constraints, each halving of the resolution cell size by doubling the transmit bandwidth produces a heavier-tailed reverberation envelope and a reduction in the *K* distribution shape parameter by a factor of one half [Abraham & Lyons 2004a, Abraham & Lyons 2004b, Johnson *et al*. 2005, Lyons *et al*. 2005, Lyons *et al*. 2009]. A similar study in optics relating shape parameter to illuminated scatterers dates back to 1978 [Jakeman & Pusey 1978], following prior theoretical work and data analysis [Jakeman & Pusey 1975, Pusey & Jakeman 1975]. *K*-distributed reverberation

has been linked to a negative binomial distribution of scatters [Jakeman 1980, Abraham & Lyons 2002b], scattering from a sub-fractal rough surface [Jakeman 1982a, Jakeman 1982b, Ogilvy & Merklinger 1991], a Gamma distributed noise process modulated by a second underlying Gamma process [Blacknell *et al*. 1994a, Blacknell 1994b], a Rayleigh distributed surface modulated by an underlying Gamma distribution [Jakeman 1980, Tough & Ward 1999], and coherent imaging speckle modulated by a negative exponential or Gamma distribution [Goodman 2007]. In [Ward *et al*. 1990] modulated representations are referred to as the 'compound *K* distribution,' from clutter being a combination of speckle and texture, modeled as a Rayleigh-like and Gamma-like component respectively.

The simplicity of a single adjustable parameter after normalization, inherent mathematical properties that make simulation efficient (and even possible), ability to fit a wide range of data, and ties to physical quantities make the *K* distribution an excellent choice for modeling heavy-tailed reverberation in complex natural environments. The *K* distribution shape parameter serves as an excellent metric for the impact of environmental influences and system parameters on reverberation statistics.

1.3.2 Random Walk Analogy

An alternative view for the justification of the Rayleigh distribution and analogy for potential shortcomings, is to view reverberation as the result of a two-dimensional random walk (where amplitude and phase represent the two dimensions). For an infinite

number of steps where each step has a random distance with a uniform probability of direction, the random walk will result in Rayleigh-distributed distances from the origin [Rayleigh 1919, Jakeman & Tough 1988]. However, a Rayleigh distribution is not necessarily the result when the direction is no longer a uniform distribution [Bisceglie *et al*. 1999] (known as a biased-random or Drunkard's walk), or when the number of steps themselves is a random variable [Jakeman & Pusey 1978, Jakeman 1980]. A mathematical derivation arriving at the *K* distribution for a random walk with a directional bias, even as the number of steps goes to infinity, is given in [Jakeman & Tough 1988].

We make the distinction that the Rayleigh distribution is the magnitude of two orthogonal Gaussian distributions (in our case, Gaussian-distributed amplitude – distance of the step, and uniformly-distributed phase – direction of the step). Figure 1.6 demonstrates this idea visually, fixing the number of steps to 10,000. The top left plot shows a pure Random Walk as specified above. The top right plot shows a Drunkard's or biased Random Walk, which is the resulting motion when a directional bias is applied to a random walk. Here the direction has been limited from 2π to 1.95π, and even with 97.5% of the directions available the resulting direction is much more deterministic. The bottom plots of Figure 1.6 depict the ending locations for 1000 such Random (left) and Drunkard's (right) Walks, each of which can be thought of as the amplitude of a single Sonar resolution cell. The axis values are inconsequential, although it might be helpful to consider the random walks as being in complex space with the *x*-axis as the real axis and *y*-axis as the imaginary, with ties to the reverberation model of Equation 1.18, such that:

$$z = x + i\,y \,, \qquad \text{Equation 1.21}$$

$$A_m = \sqrt{x^2 + y^2} \,, \qquad \text{Equation 1.22}$$

and

$$\theta_m = \tan^{-1}\frac{y}{x} \,. \qquad \text{Equation 1.23}$$

Although 10,000 steps are certainly not infinite, there is a good approximation of significant randomness for 1000 realizations of 10,000 steps. We will return to the analogy of the Random Walk in later discussions by extending the analogy for multipath reverberation and the phenomenon of speckle in a coherently formed image.

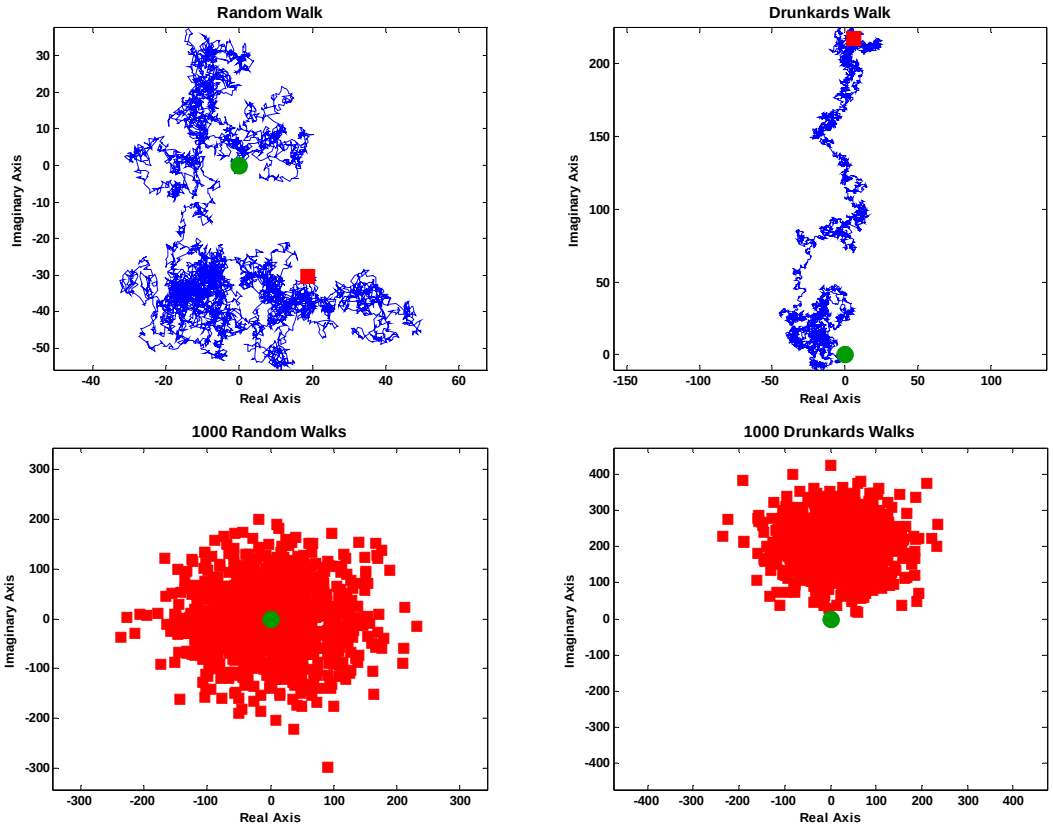

Figure 1.6: Random and biased-Random (or Drunkard's) Walks

1.3.3 Goodness of Fit

While Figure 1.4 visually depicts in the inability of the Rayleigh distribution to model collected data, a goodness of fit test such as the Kolmogorov-Smirnov (KS) test provides a quantitative means. The KS test is a measure of the goodness of fit between sample data and a specified test distribution [Fisz 1978]. As with any goodness of fit test, the KS test does not ensure a sample distribution is identically a specific probability

distribution, but rather serves to exclude tested distributions. This is summarized anecdotally by the following quotation:

> "Any frequentist test (such as the KS test) is constructed to disprove something. Just as a dry sidewalk is evidence that it didn't rain, a wet sidewalk might be caused by rain or by the sprinkler system. So a wet sidewalk can't prove that it rained, while a not-wet one is evidence that it did not rain." [Annis 2008]

Normalization of sample data is performed to obtain near unit mean intensity prior to the KS test, after which the *K* distribution shape parameter is estimated (discussion of the normalization and parameter estimation is given in the following chapter). The cumulative distribution function (CDF) is then calculated for both a Rayleigh distribution and the equivalent *K* distribution using this estimated shape parameter. Although choosing a theoretical CDF based on estimated parameters from the experimental data to be tested violates Kolmogorov's theorem [Fisz 1978], this usage of

the KS test statistic[4] is adequate to reject hypothesized distributions, particularly with the large number of samples available here for parameter estimation.

Considering the 60-100 kHz SAS data shown in Figure 1.4, and a significance level of 5% (less than 5% of the data is rejected when it should be accepted as being well fit), 33.3% of the 60-100 kHz data is accepted as being Rayleigh while 91.0% is accepted as being *K*-distributed; and for a significance level of 1%, 47.3% is accepted as Rayleigh while 95.8% as *K*-distributed [Lyons *et al*. 2005]. From these values, along with the visual comparison of the PDFs, we will assume the data are well fit by the *K* distribution. The shape parameter of the *K* distribution may then be used to as a metric of the reverberation statistics for the discussion presented in this work.

---

[4] It is noted that the KS test is less sensitive to the tail of a distribution compared to the Mann-Whitney test; however at present the necessary critical values for calculation of this test do not exist for the *K* distribution, and would involve a similar violation of Kolmogorov's theorem since a portion of the population is needed to estimate the *K* shape parameter.

1.3.4 Target Detection System Performance

The accuracy of detection and classification algorithms is dependent upon the quality of statistical assumptions made to simplify a complex problem. The simplest target detection system is an energy detector, which is a simple 'true' or 'false' algorithm based on whether or not an input energy at a single time exceeds a given threshold, which is then taken to mean the presence of a target. There are four probabilities that must be considered:

P_D: Probability of Detection (object exists and is detected),

P_{MD}: Probability of Missed Detection (object exists but is not detected),

P_{FA}: Probability of False Alarm (object does not exist but is detected, and

P_{NULL}: Probability of Null (object does not exist and is not detected).

Each of these four probabilities is specific to the chosen threshold. As data are typically normalized before being input to an energy detector, there is a single parameter of threshold.

The performance of energy detectors is typically measured with Rayleigh reverberation. As seen in Figure 1.4, high-resolution shallow water reverberation data may exhibit envelope PDFs that are significantly non-Rayleigh, which often causes an increase in the Probability of False Alarm (P_{FA}). False alarms occur when the detection algorithm outputs target detection when in actuality no target is present. The P_{FA} is a

summation of the probability density above a specified target threshold, and can be orders of magnitude higher for certain thresholds when background reverberation exhibits heavy-tailed PDFs. Figure 1.7 shows the Probability of False Alarm for the data shown in Figure 1.4. In this example, if a target threshold of 3 is chosen, the actual P_{FA} is two orders of magnitude greater than anticipated with the Rayleigh assumption.

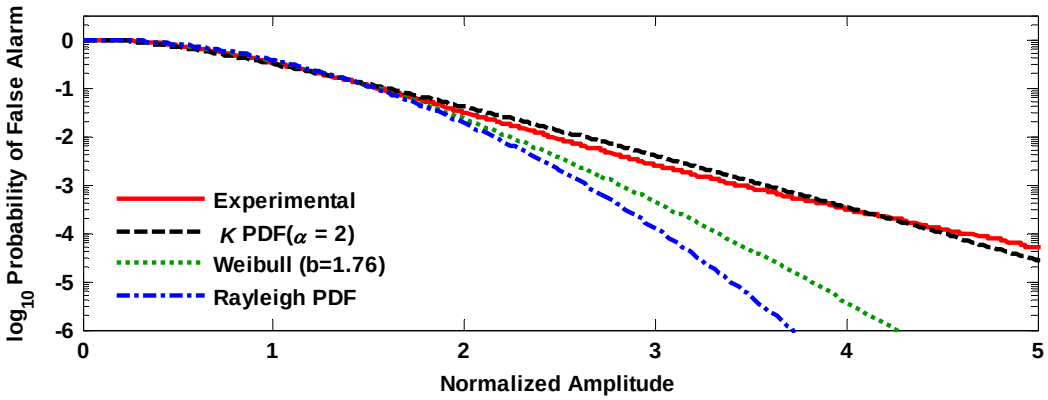

Figure 1.7: Probability of False Alarm corresponding to Figure 1.4

As a visual example, assume three targets of known amplitudes (2.8; 3.0; 3.2) at locations (7,7; 13,13; 18,18) are placed in a two-dimensional space of Rayleigh-distributed amplitudes which is normalized to unit mean power as shown in Figure 1.8 (top). When a threshold is chosen slightly less than the amplitude of the targets (2.7), all three targets are detected with one False Alarm (Figure 1.8 bottom). However, when the same three targets are placed in a two-dimensional space of significantly heavy-tailed amplitudes (here *K*-distributed of α=1 and again normalized to unit mean power), there are 23 detections with 20 False Alarms for the same target threshold (Figure 1.9); an

increase of 767%! In this example a pixel may be thought of as a single Sonar (or Radar) resolution cell. It may be argued that in high-resolution systems objects of interest would have physical dimensions that exceed a single resolution cell, however one should consider the discussion presented previously pertaining to the dependence of remote sensing on statistics. The acoustic response of an object may be confined to a 'glint' or strong response with a short angular or temporal duration. Also, the object of interest may be buried or otherwise acoustically obscured by the environment. These false alarms span the remote-sensing spectrum plaguing virtually every system for some set of conditions, and are often referred to as clutter when environmentally induced.

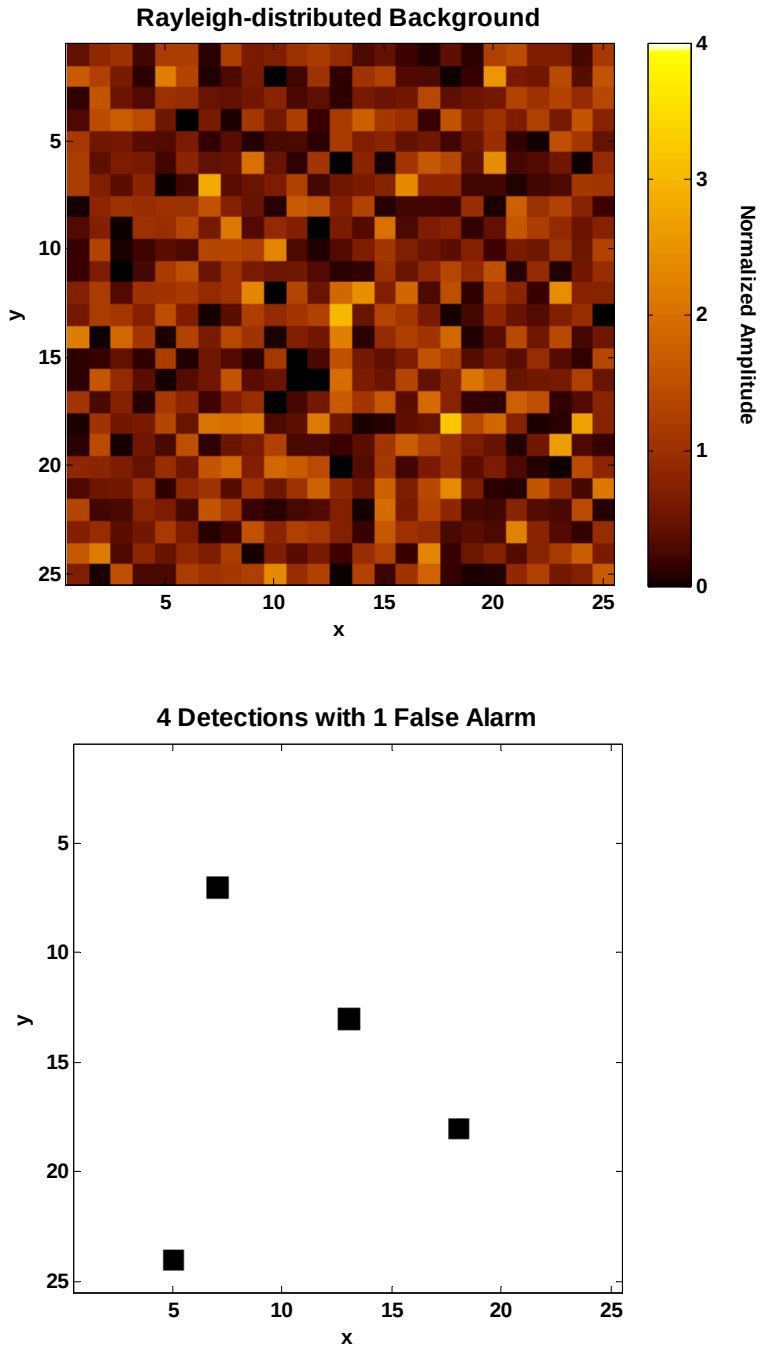

Figure 1.8: Three ‘objects’ on Rayleigh-distributed background and four detections.

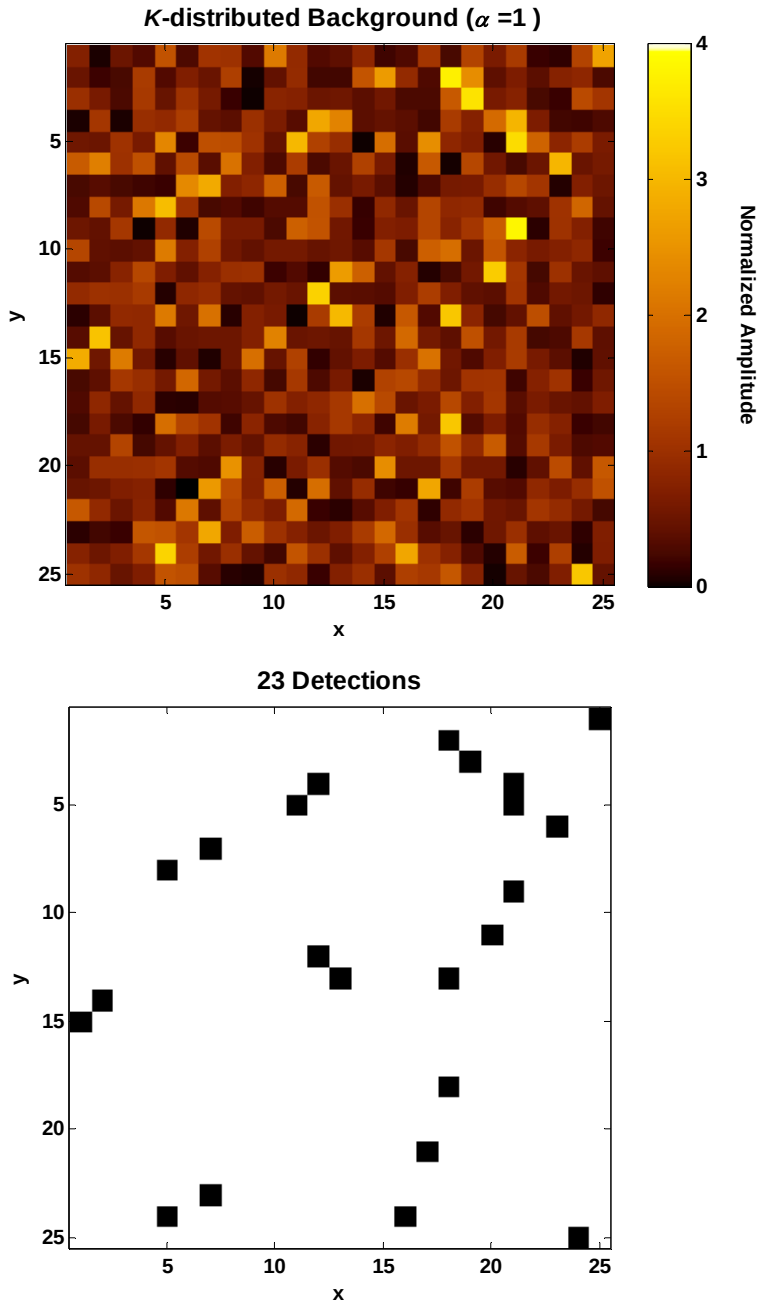

Figure 1.9: Three ‘objects’ on *K*-distributed background and twenty-three detections.

In an effort to mitigate the amount of false alarms, computer-aided detection / computer-aided classification (CADCAC) systems are now commonplace in both combat and civilian systems. These systems are significantly more complex than Energy Detectors, and often involve fusion of information from multiple detections on the same and potentially other sensors before outputting a response of both detection and classification [Dobeck *et al*. 1997, Dobeck 1999, Dobeck 2001, Dobeck & Cobb 2002]. An example of a CADCAC system is shown in Figure 1.10.

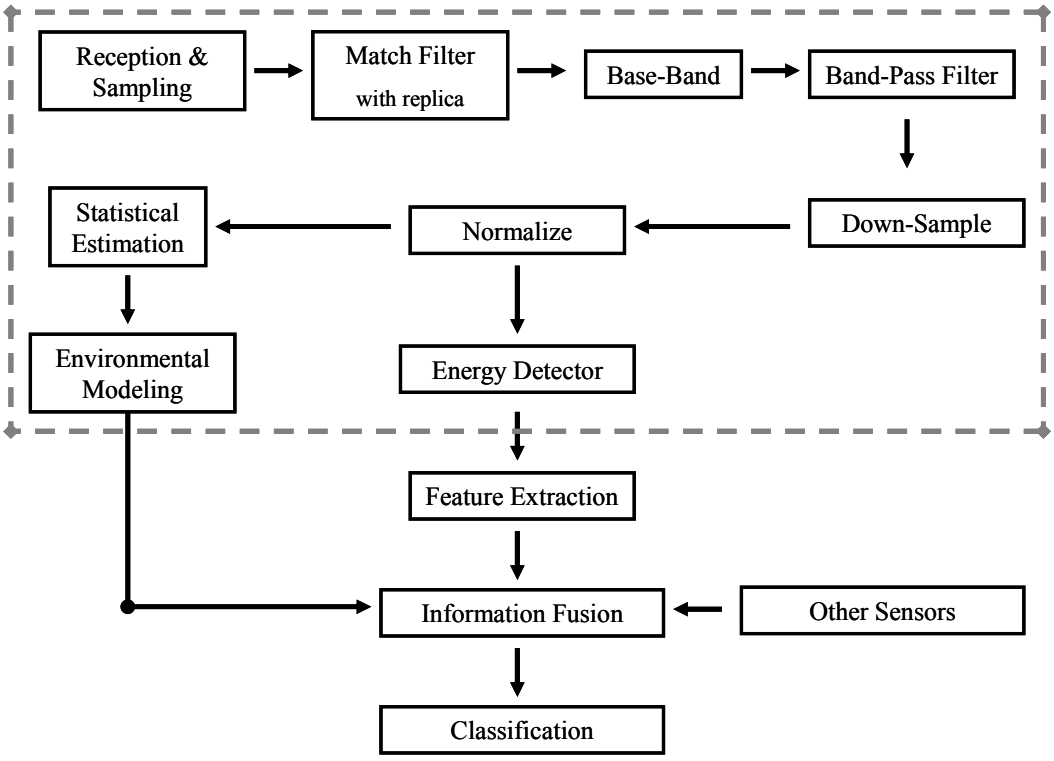

Figure 1.10: Signal flow of an example CADCAC system.

In addition to the probabilities given above for the energy detector, additional probabilities must be considered in the design of a CADCAC system, namely:

P_C: Probability of Classification (object is correctly identified), and

P_{DC}: Probability of Detection & Classification (object is detected and identified).

The probability calculations for a Classification Algorithm are not as straight forward as that of the Energy Detector [Cobb & Stack 2007, Gazagnaire *et al*. 2007], as there are often numerous additional components of the process. Additionally, such systems are often autonomous and must be 'trained' with 'true' versus 'false' signals (*i.e.* targets versus clutter) before attempting to provide appropriate responses (a Support Vector Machine is an example of such a 'supervised learning' system with routine usage by the US Post Office to decipher hand-written zip-codes). The performance of CADCAC systems therefore depends on the quality of both the target-like and clutter-like signals input to the system during the training stage.

While clutter can be mitigated by compiling additional information (fusing data from other sensors or multiple detections from a single sensor), in many systems it triggers the 'first-response' of detection algorithms requiring the input of additional sensors and analysis of further information. Reduction of the tails is also of interest in situations were data are relatively Rayleigh-like. As system resolution is increased with advances in technology, even a modest Probability of False Alarm can produce an overwhelming number of false alarms owing simply to the number of data samples being collected [Waite 2005] (*i.e.* increasing the data rate, or resolution, by a factor of ten will increase the number of false alarms by a factor of ten, even when the P_{FA} is held

constant). Thus, a thorough understanding of the causes of both environmental and system induced clutter is necessary for sensor and algorithm development. Further, as the necessity exists to operate systems in as-yet unknown environments, combined with continued environmental restrictions on training operation of *in situ* systems, the ability to generate physically-based synthetic clutter signals is of principal importance.

Chapter 2

Analysis and Simulation Methods

2.1 Chapter Introduction

This chapter introduces the experimental data sets, analysis tools, and modeling methods used for this study. A description of two experimental systems used is presented first, followed by general data analysis methods for estimating the *K* distribution shape parameter and calculating the Scintillation Index. A discussion of generating random variates and simulating correlated acoustic images of sand ripples follows, which will be used in subsequent chapters to confirm data analysis of the impact of multipath and resolution on Synthetic Aperture Sonar image statistics. The analysis and modeling presented in this work start at the output of the matched-filter at the lowest level, and typically after synthetic aperture image formation. Simulated reverberation is generated to replicate this point of the signal processing.

2.2 Experiment and System Descriptions

Data from two different systems have been analyzed and serve as the basis for this study. The synthetic aperture beamforming algorithms are based on methods presented in [Hawkins 1996, Cook 2007], and utilize the wavenumber inversion technique (also know as Stolt-mapping or ωk). While other synthetic aperture processing schemes may

be more efficient given the computationally expensive interpolation process involved with wavenumber inversion, this method is still easily handled by modern desktop computers. More importantly for the purposes of this study, the two-dimensional wavenumber domain can be exploited as a basis for the post-processing resolution adjustment analysis of Chapter 4. The first dataset comes from the Sediment Acoustics eXperiment 2004, and will be designated in later reference as SAX04. The second dataset comes from a collection of missions utilizing the Small Synthetic Aperture Minehunter, and will be later references as SSAM.

2.2.1 SAX04

Broadband acoustic measurements were performed by the Applied Physics Laboratory of the University of Washington (APL-UW) using a rail-mounted mobile tower during the 2004 U.S. Office of Naval Research funded Sediment Acoustics eXperiment 2004 (SAX04). The experimental site was approximately 1 km offshore south of Fort Walton Beach, FL with a water depth of approximately 17 m (55 ft) (Figure 2.1). The purpose of the study was to investigate enhanced acoustic penetration into the seafloor at low grazing angles in the presence of sand ripples. As such, the rail-mounted mobile tower was situated such that the motion of direction was approximately parallel to the crests of surface-wave formed sand ripples. The bottom composition consisted of rippled sand over mud patches [Williams *et al*. 2009] as the result of a series of tropical cyclones; Hurricane Ivan (September 9-24, 2004) and Tropical Storm Matthew (October 8-11, 2004). Data presented here were collected on October 26, 2004.

The rail-mounted mobile tower was equipped with a variety of acoustic transducers with various bandwidths spanning 3 to 200 kHz in six bands, typically with one transmitter and six receivers of various vertical apertures for any given band (Figure 2.2). Data presented here are of 30-50 kHz and 60-100 kHz bandwidths. Measurements were made with a spacing of 2.5 cm between transmissions over a span of 28 meters. These parameters yield a maximum synthetic aperture resolution of: $\Delta x_{slant} \approx 2$ cm and $\Delta y_{SAS} \approx 5$ cm from Equations 1.1 and 1.13. A more complete description of the experiment and system can be found in [Williams *et al*. 2005a, Williams *et al*. 2005b].

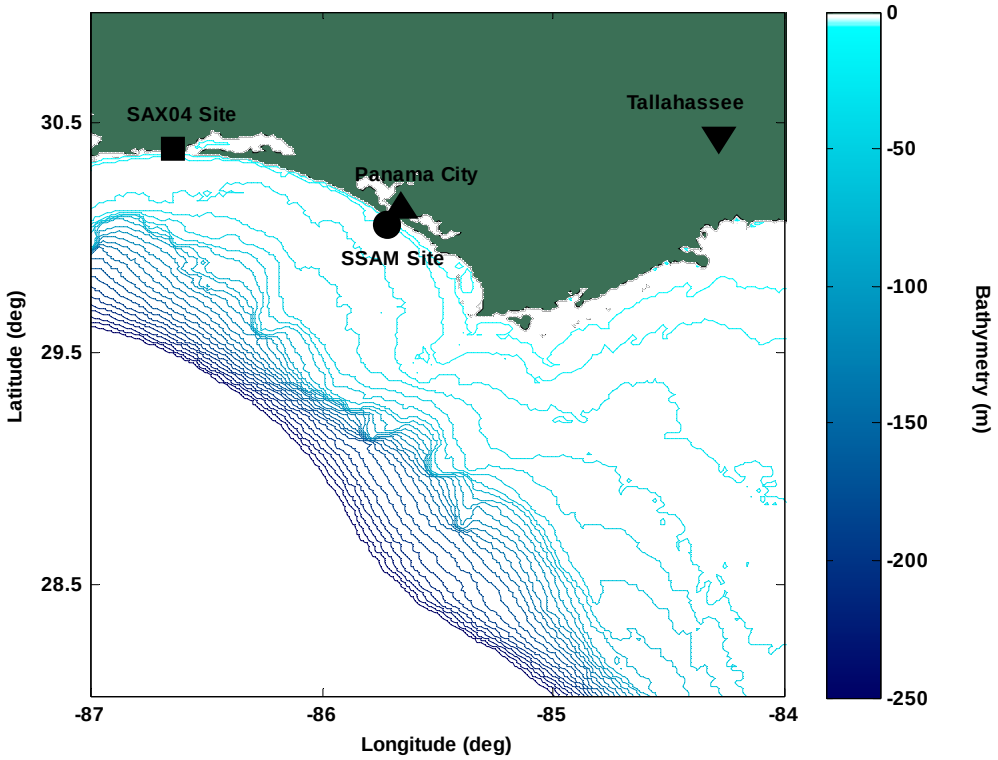

Figure 2.1: SAX04 and SSAM experimental sites off the coast of Florida. (bathymetric data of [Smith & Sandwell 1997]).

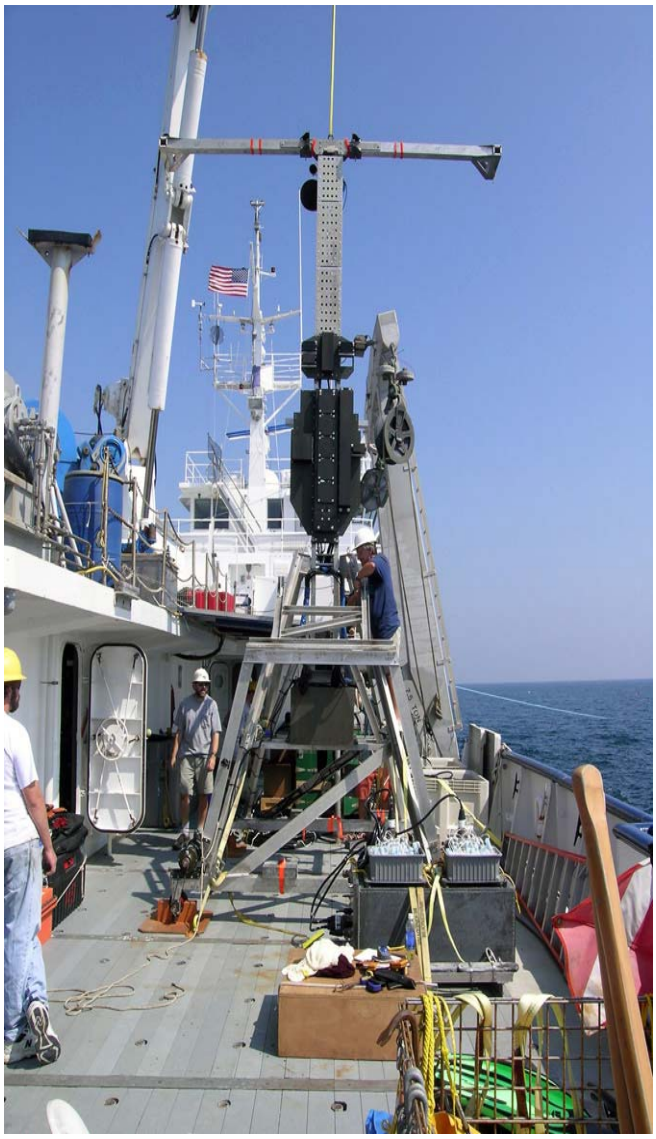

Figure 2.2: SAX04 mobile tower before deployment (photo courtesy of the Applied Physics Lab – University of Washington).

2.2.2 SSAM

The Small Synthetic Aperture Minehunter (SSAM), a joint development between the Naval Surface Warfare Center – Panama City Division and the Applied Research Lab – Penn State, is a REMUS 600 Autonomous Underwater Vehicle (AUV) based Sonar suitable for synthetic aperture processing (Figure 2.3). Although the REMUS vehicle is very stable, AUV based SAS systems must correct for motion of the platform from yaw, pitch, heave, and roll during the image formation process. This is in contrast to a rail-mounted system as in the SAX04 experiment, and provides a significant challenge to image reconstruction; specific details of motion compensation can be found in [Cook et al. 2003, Cook et al. 2005, Cook 2007]. Data were provided as complex beamformed and motion compensated images, and come from demonstration experiments near La Spezia, Italy (Figure 2.4) and near Panama City, FL (Figure 2.1), and consist mainly of rippled sand. The SSAM is a dual-frequency Sonar, with frequency ranges of 8-55 kHz and 105-135 kHz. The low-frequency (LF) band images presented here have a resolution of $\Delta x_{slant} \approx 1.2$ cm by $\Delta y_{SAS} \approx 6.7$ cm and high-frequency (HF) band imaged with a resolution of $\Delta x_{slant} \approx 5.8$ cm by $\Delta y_{SAS} \approx 2.0$ cm. A more complete description of the experiments conducted with, and development of, the SSAM system can be found in [Fernandez *et al*. 2004, Stokey *et al*. 2005, Brown *et al*. 2006].

Figure 2.3: REMUS600 mounted SSAM before deployment (photo courtesy of the Naval Surface Warfare Center – Panama City Division).

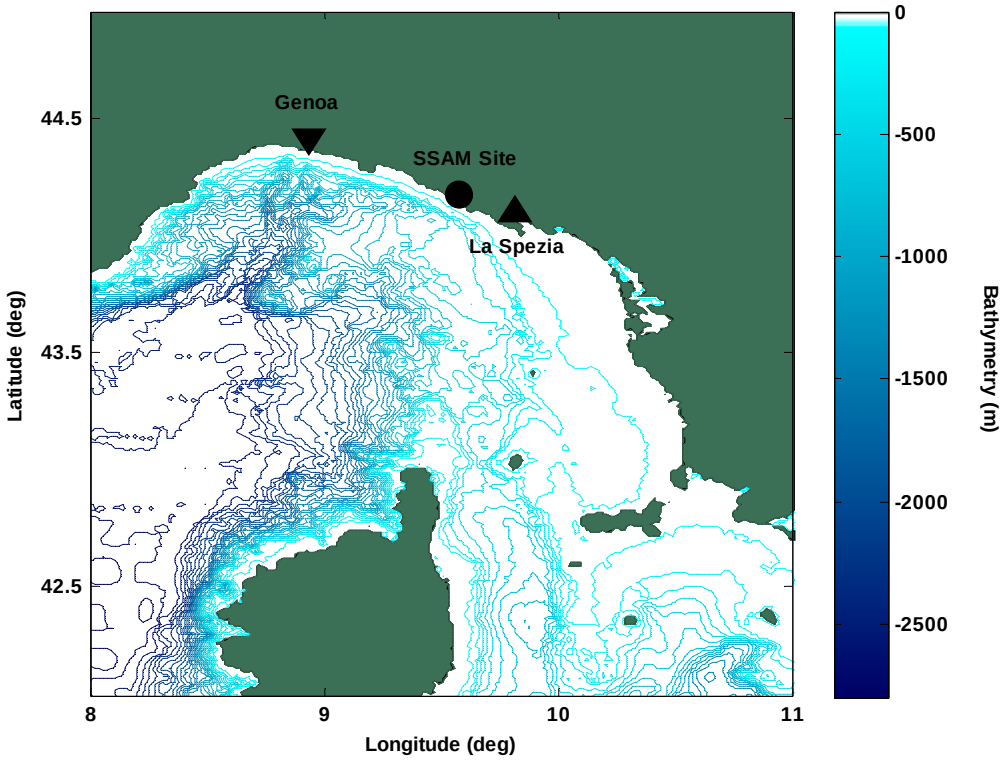

Figure 2.4: SSAM experimental sites off the coast of Italy. (bathymetric data of [Smith & Sandwell 1997]).

2.3 Data Analysis

As discussed in Chapter 1, the *K* distribution has been shown to fit a wide range of Sonar data, with the shape parameter being an excellent metric for heavy-tailed non-Rayleigh envelope probability distributions. An additional statistical measure is the Scintillation Index which is a measure of the intensity variance. Prior to the estimation or calculation of these statistical measures, data must first be pre-processed and normalized.

2.3.1 Pre-Processing

High-resolution Sonar systems are capable of producing a significant amount of data in a short period of time, owing to high pulse repetition rates and/or multiple channels of reception for beam forming. Imaging Sonar systems have the additional requirements of high sample rates because of the high carrier frequencies (f_c) involved (*e.g.*, 40 and 80 kHz f_c for SAX04, and 120 kHz f_c for SSAM HF band). In an effort to increase resolution without unduly increasing reverberation, wide bandwidth signals are transmitted. These signals can have a variety of frequency, phase, and Doppler characteristics, but perhaps the most widely employed are linear frequency modulated (LFM) chirps. Upon reception, the data are match filtered, or correlated with a replica of the transmitted signal, to obtain the impulse response. This is analogous to transmitting a pulse with an equivalent pulse length of bandwidth^{-1}, without the mechanical and electrical stress on the transmitter required to produce comparable resolution. In an effort to maintain storage space, data are often basebanded which reduces the carrier frequency

to zero after band-pass filtering the signal. From this point forward, data must remain complex to ensure later retrieval of the frequency-dependant nature of the data. The data may now be band-pass filtered at the bandwidth (BW) from –BW/2 to BW/2, and the sample frequency (f_s) is down-sampled to the bandwidth. These steps describe the optimum packing of data without introducing the adverse effects of sample aliasing, and also ensure that data are not over-sampled in space or frequency which is a necessary requirement for proper calculation of statistical measures. The order of these operations may differ based on the system configuration, so long as attention is paid to the signal flow to avoid inducing unnecessary signal processing artifacts. Figure 2.5 shows a block diagram of typical pre-processing operations.

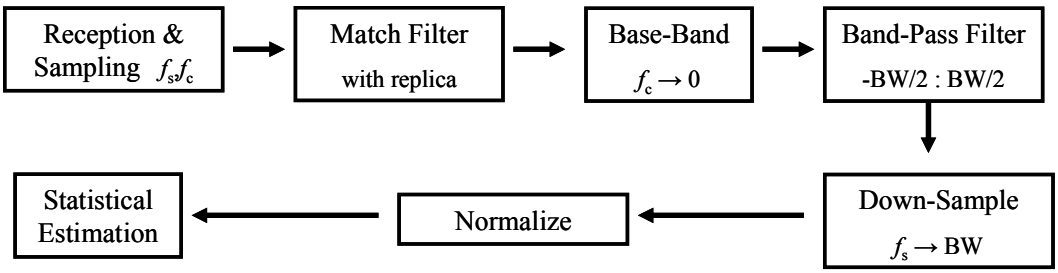

Figure 2.5: Typical Sonar pre-processing routine.

2.3.2 Normalization

Match-filtered data that have been basebanded must be normalized prior to statistical parameter estimation. The purpose of normalization is to remove gross power fluctuations, while leaving the small-scale structure of the data. These gross fluctuations

are typically the result of transducer beam patterns and sensitivity, spreading losses as a function of range, or changes in the backscattering strength of the seafloor from composition or Sonar grazing angle. These differences in dynamic range of the mean noise levels are reduced by comparison of power in a particular Sonar resolution cell to surrounding, but not adjacent, cells [Waite 2005]. Normalization is necessary for the statistical analysis described in the following section as the mean of a stationary random process must be constant [Hayes 2002, Papoulis & Pillai 2002]. From a practical standpoint, normalization also allows for a constant threshold to be set for all resolution cells, resulting in a constant False Alarm rate (CFAR) detector [Kay 1998]. As in the pre-processing steps listed previously, extreme care must be exercised to not induce unintentional artifacts to the data. While proper normalization enables the description of reverberation as a random process with reproducible statistical measures, improper normalization can induce artificial changes in the statistical nature of data. In general, a very small normalizer window (*i.e.* on the order of system resolution) will trend estimates more Rayleigh-like [Abraham & Lyons 2004a], and a window much larger than underlying power fluctuations will increase the tails [Cole *et al*. 2004].

To counter the effect of vertical beam pattern response and spreading loss, data are often solely normalized as a function of range. The normalization operator for range normalization can be computed analytically by combining estimates of the beam pattern with a range^{-2} term, or by ensemble averaging multiple pings. An example of the latter is given in Figure 2.6, where data are normalized by a polynomial fit to the ensemble-averaged intensity. Again, the complex nature of the data must be preserved if later

frequency dependent analysis is performed. While this procedure is easily implemented and often yields satisfactory results, situations may arise where the seafloor scattering strength changes not because of angle but because of composition, either with range or cross-range. In such scenarios, it may be necessary to normalize data giving consideration to correlations on a smaller scale. Further, for the two-dimensional processing to be presented in Chapter 4, it is necessary to obtain consistent two-dimensional normalization of the data.

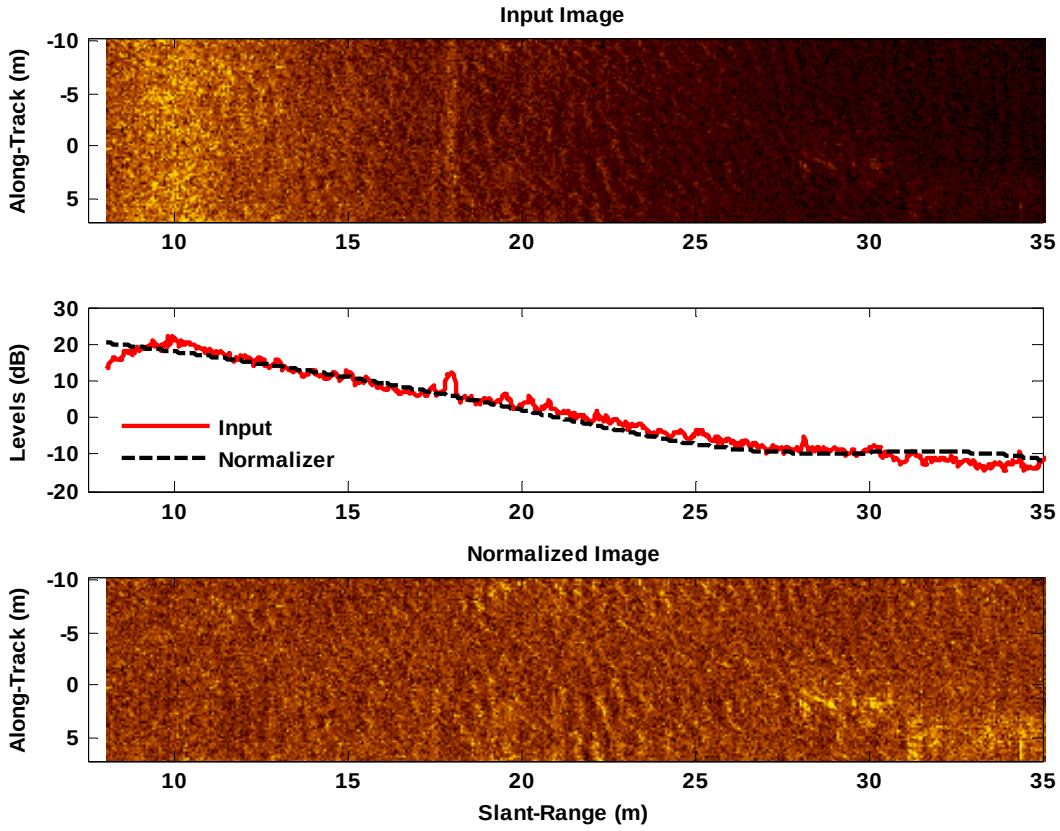

Figure 2.6: An example polynomial-based normalization.

A new technique has been developed to normalize complex data in two-dimensions [Johnson *et al*. 2005, Johnson *et al*. 2008]. This technique is implemented by creating a smoothed two-dimension version of the data matrix, which has the dimension of slow-time by fast-time, or along-track pings by slant-range samples. The filter window has variable width and guard band distances in both directions Figure 2.7 which are set by the user, and the mean intensity of the data contained within that window is computed; the resulting normalization surface is then applied to the data resulting in a smoothed version corresponding to the mean power fluctuations underlying the data surface. The original complex data are then divided by the amplitude of this smoothed version. Figure 2.8 depicts an example of this two-dimensional normalization technique. Successful normalization results in data with constant unit mean intensity, without corruption of the reverberation statistics resulting from the random processes of interest.

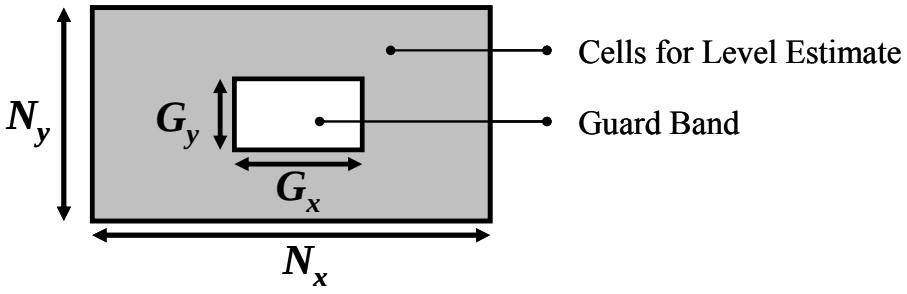

Figure 2.7: Image-based normalizer window and guard bands.

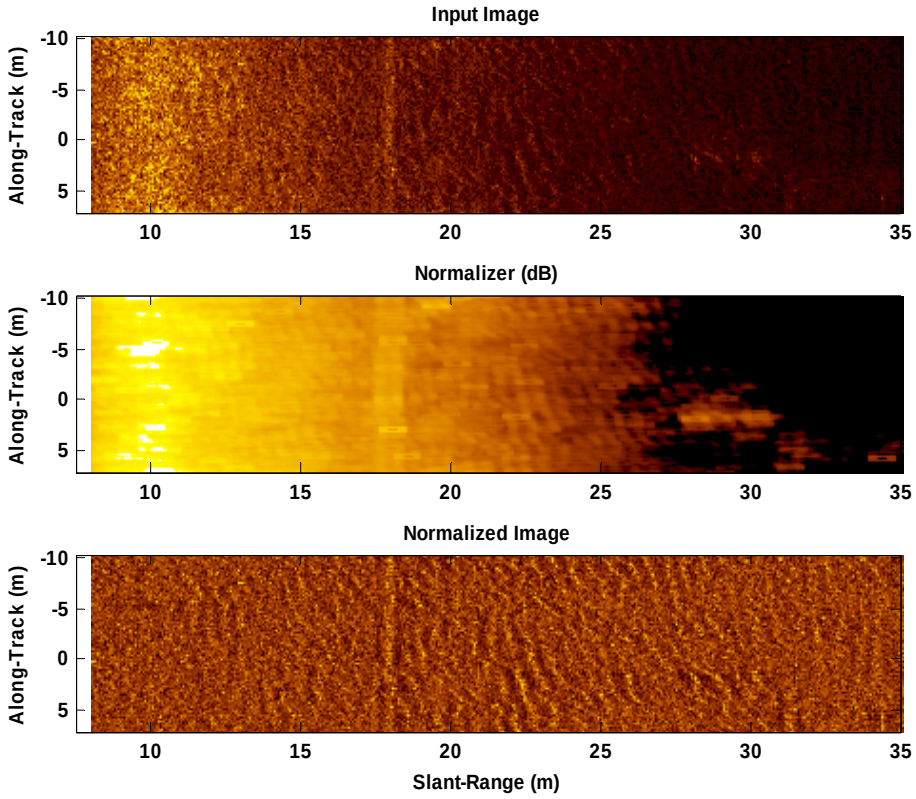

Figure 2.8: An example image-based normalization.

2.3.3 Estimation of Statistical Parameters

Statistically-based conclusions are inferences based on observations of data [Papoulis & Pillai 2002]. In our case these observations are of Sonar reverberation, which is the acoustic response of an environment to an active transmission. As statistical parameter estimations of data presuppose the observations are of stationary data (*i.e.* resulting from a fixed set of random processes), we can then assume that changes observed in the statistical measures indicate the limits of this assumed stationarity. In the

following chapters, changes observed in estimates of the statistical parameters will be correlated with the presence of multipath (Chapter 3) and Sonar system resolution (Chapter 4).

It should be noted however, as parameter estimation is a function of observations of a random process, the estimates are random variables [Hayes 2002]. In theory, when the sample population is sufficiently large estimates converge to an asymptotic value. In practice, however, only small portions of stationary data are available for estimation either because of time constraints or because the processes are non-stationary [Zoubir & Boashash 1998]. Estimation windows then should be large enough to limit the variance of the estimations, but small enough to accurately portray changes in the random processes.

2.3.3.1 *K* Distribution Shape Parameter Estimation

As presented in Chapter 1, the *K* distribution (Equation 1.20) has been shown to provide a good fit to a wide range of data with the shape parameter proportional to the number of ensonified scatterers [Abraham & Lyons 2002b], making the shape parameter an excellent metric for the study of the statistics of reverberation. Numerous methods have been proposed to estimate the shape parameters of the *K* distribution. While the maximum likelihood estimate (MLE) is typically considered to give the best estimates (*i.e.* parameter estimates converge as the sample size goes to infinity and do so efficiently, and the estimates are asymptotically Gaussian) [Van Trees 1968], no closed

form solution exists for the MLE of the *K* distribution requiring parameters to be estimated numerically. This involves a computationally expensive search of parameter space for every data sample [Joughin *et al*. 1993, Jahangir *et al*. 1996], saddlepoint integration [Gordon & Ritcey 1995], or an iterative expectation-maximization (EM) algorithm [Roberts & Furui 2000, Chung et al. 2005]. Additionally, *K* parameters have been estimated by approximation to the Gamma distribution [Raghavan 1991, Oliver 1993, Bisceglie *et al*. 1999]. Artificial neural networks have also been utilized [Jahangir *et al*. 1996, Wachowiak *et al*. 2002], however these require training of the network posing the additional dilemma of accurately synthesizing *K*-distributed training data.

An alternative approach is the method of moments (MOM) using the first and second moments [Joughin *et al*. 1993, Abraham 1997, Abraham & Lyons 2002a], second and fourth moments [Joughin *et al*. 1993], higher order and fractional moments [Iskander & Zoubir 1996, Iskander 1999], moments of the log of the data [Jahangir et al. 1996, Redding 1999, Blacknell & Tough 2001], or a hybrid between the mean and the mean of the log of the data [Blacknell 1994c, Dong 2004]. MOM estimators have been shown in several of the references above to provide results similar to the MLE for many cases. However, the MOM may fail to produce a useable solution for large values of α or when the number of samples in the observation is small. A helpful workaround is this situation is implementation of the bootstrap technique [Zoubir & Boashash 1998] for the method of moments, which has been shown to provide solutions for small sample populations and low values of α [Abraham & Lyons 2006]. Considering accuracy of parameter

estimation and computation efficiency, this study employs either the first and second order MOM, or the bootstrapped MOM.

2.3.3.2 Scintillation Index Calculation

An inherent problem with estimating parameters of a statistical distribution from observations is whether the hypothesized distribution accurately describes the data. While goodness of fit measures can exclude hypothesized distributions, they cannot choose an optimal hypothesis. Likewise, visual inspection of the probability densities of various hypothesized distributions compared to data only serves to confirm a mathematical model as a good descriptor of data. An alternative statistical metric is the Scintillation Index, or relative intensity variance, which is a direct measure much like the mean and variance. As shown in [Abraham & Lyons 2002b, Lyons *et al*. 2005] given by:

$$\sigma_I^{\,2} = \frac{\mu_2 - \mu_1^{\,2}}{\mu_1^{\,2}}, \qquad \text{Equation 2.1}$$

where μ_1 and μ_2 are the first and second moments of the intensity of the complex envelope of the received signal. Using this form, the Scintillation Index and K distribution shape parameter are then related by [Lyons *et al*. 2005]:

$$\mu_1 = \alpha\lambda\,, \qquad \text{Equation 2.2}$$

$$\mu_2 = \mu_1^{\,2} + 2\alpha\lambda^2 , \qquad \text{Equation 2.3}$$

and

$$\sigma_I^{\,2} = 1 + \frac{2}{\alpha} . \qquad \text{Equation 2.4}$$

While these equations only hold if the data are indeed well modeled by a *K* distribution, they serve as a comparative check of the shape parameter estimation process given in the previous section. Also, the Scintillation Index can be calculated directly from normalized data, whereas the *K* shape parameter is an estimate of a matched theoretical distribution. The Scintillation Index also generally has less variance for a smaller sample size as compared to the *K* shape parameter, which will be useful when considering particular cases.

Scintillation Index calculations can be implemented as a sliding window for the multipath analysis of Chapter 3, or for an entire scene for the resolution analysis of Chapter 4. An alternative analysis is to consider the statistics of multiple adjacent pixels of a gridded image. Figure 2.9 shows a sample SAS image from Figure 1.1 of a complicated seafloor with ripples and *Posidonia Oceanica* seagrass (top), and *K* shape parameter estimates from grouped 25 by 25 neighboring pixel Scintillation Index calculations of the image (bottom) (for this example, calculating the Scintillation Index was 35 times faster than estimating the *K* distribution shape parameter using the method of moments). The color shading of the SAS image (top) is determined by the received

level of backscattered acoustic energy, while the color of the statistical image (bottom) is related to the inter-pixel intensity variance with light colors signifying heavy-tailed envelope statistics and dark colors signifying more Rayleigh-like statistics. In this example, the regions of the rippled-sand facing towards the Sonar are heavier-tailed while the regions facing away are more Rayleigh-like as more transmitted energy is forward-scattered in the specular direction decreasing the signal-to-noise ratio (where ambient and system noise is considered to be Rayleigh) resulting in the vertical striations between 30 and 50 m range. The *Posidonia* produces a more uniform pattern as seen between 20 and 30 m range. It is this sort of statistical analysis that is useful for texture and bottom-type segmentation as in [Oliver 1993, Griffiths *et al*. 1997, Davidson *et al*. 2002, Davidson *et al*. 2004].

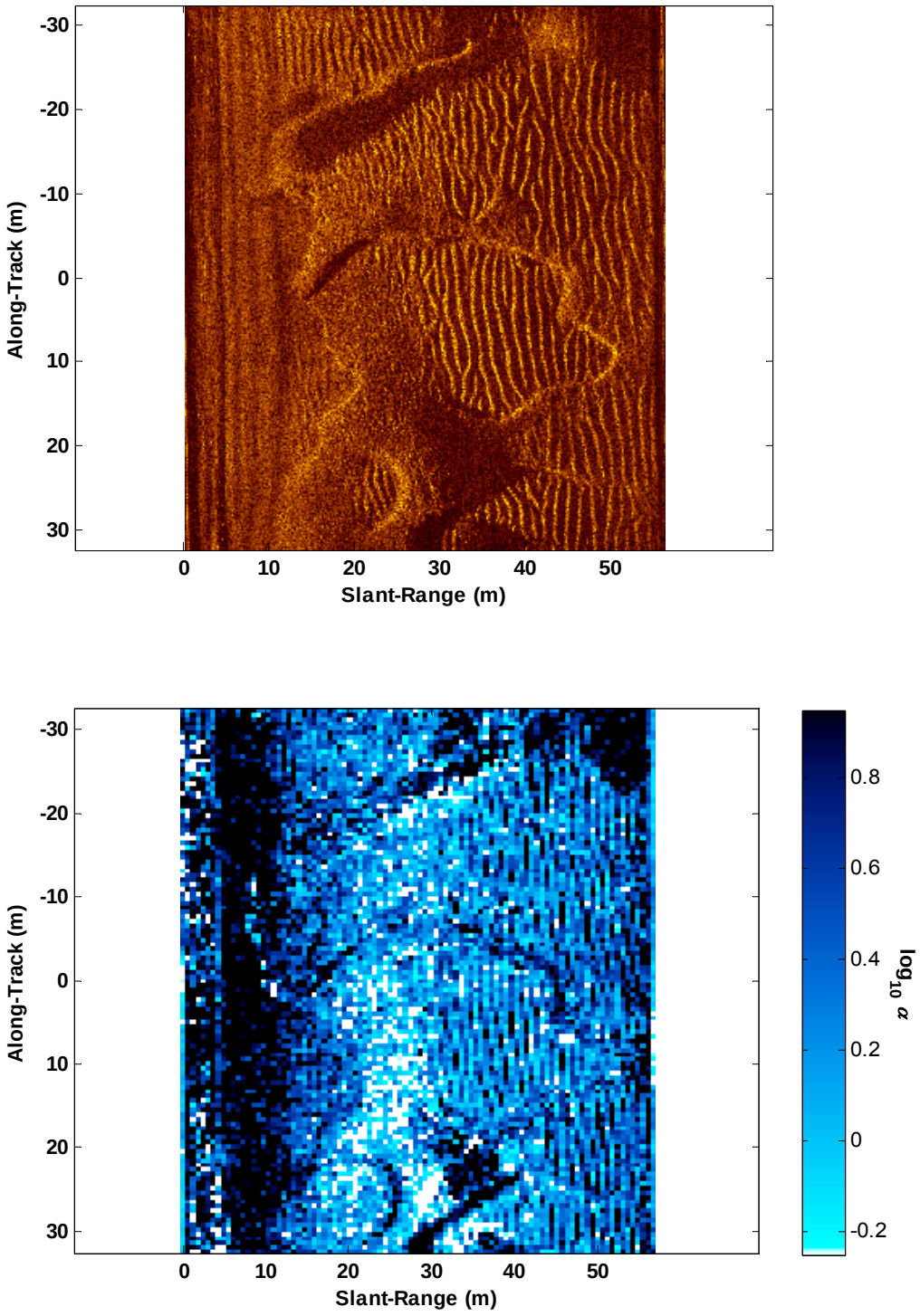

Figure 2.9: SAS image (top) and corresponding *K* distribution shape parameter estimation from multiple adjacent pixels (bottom).

2.4 Simulating Acoustic Images

Numerous[5] techniques have been proposed to simulate[6] remote sensing data, such as described in [Oliver 1986, Oliver 1988, Berman 1991, Conte *et al*. 1993, Blacknell 1994b, Blacknell 1994c, Blake *et al*. 1995, Corsini et al. 1996, Bell & Linnett 1997, Ward 1997, Franceschetti *et al*. 1998, Bell *et al*. 1999, Redding 1999, Tough & Ward 1999, Davis *et al*. 2002, Tang *et al*. 2002, Lawrence & Szabo 2003, Becker 2004, Elston & Bell 2004, LePage 2004, Abraham & Lyons 2004b] to name a few. These range from simply being random number generators which approximate a specified input PDF, to complicated physics-based simulations with computationally expensive methods such as Monte Carlo. Some of these methods include simulation of returns from targets only, environments only, or a mix of both. The intended use of these techniques and system frequencies being simulated often define the complexity and the physical models

[5] [Warnick & Chew 2001] gives 275 additional references to numerical modeling and simulation methods for analysis of electromagnetic scattering from rough surfaces.

[6] Here a distinction is made between simulating 'random' data as received and displayed by a Sonar system, compared to solving integral or differential equation methods to produce what is essentially an ensemble-averaged result of many observations.

incorporated. While the approximations of surface scattering and ray theory may be appropriate to simulate short-range high-frequency reverberation, volume scatting and modal propagation may be required for long-range low-frequency simulation. Likewise, modeling of small-scale correlated properties may be required for high-frequency simulation, while lower frequency models can generally have a coarser property sampling. Further, the specific characteristics of the Sonar system being modeled may play an important role in the simulation. The simulation models presented here draw on ideas found in several of the above referenced works, but include specific components for the task at hand: simulating the envelope of match-filtered synthetic aperture beamformed Sonar reverberation from rippled-sand seafloors in a computationally efficient manner.

2.4.1 Generating Random Variates

The simplest form of statistical simulation is generating a pseudo-random number series with a specified input PDF that is assumed to be a good fit to collected data. For this study, the PDF of the Rayleigh distribution and the *K* distribution are considered.

Generation of a Rayleigh-distributed complex random variate ($\widetilde{Z}$) with unit mean intensity can be accomplished by combining two zero-mean Gaussian random variates (G):

$$\widetilde{Z} = G + iG \quad \text{Equation 2.5}$$

Figure 2.10 shows a 1000 sample sub-set (top) of a single realization of 1×10^6 samples and corresponding PDF of the full sample set (bottom).

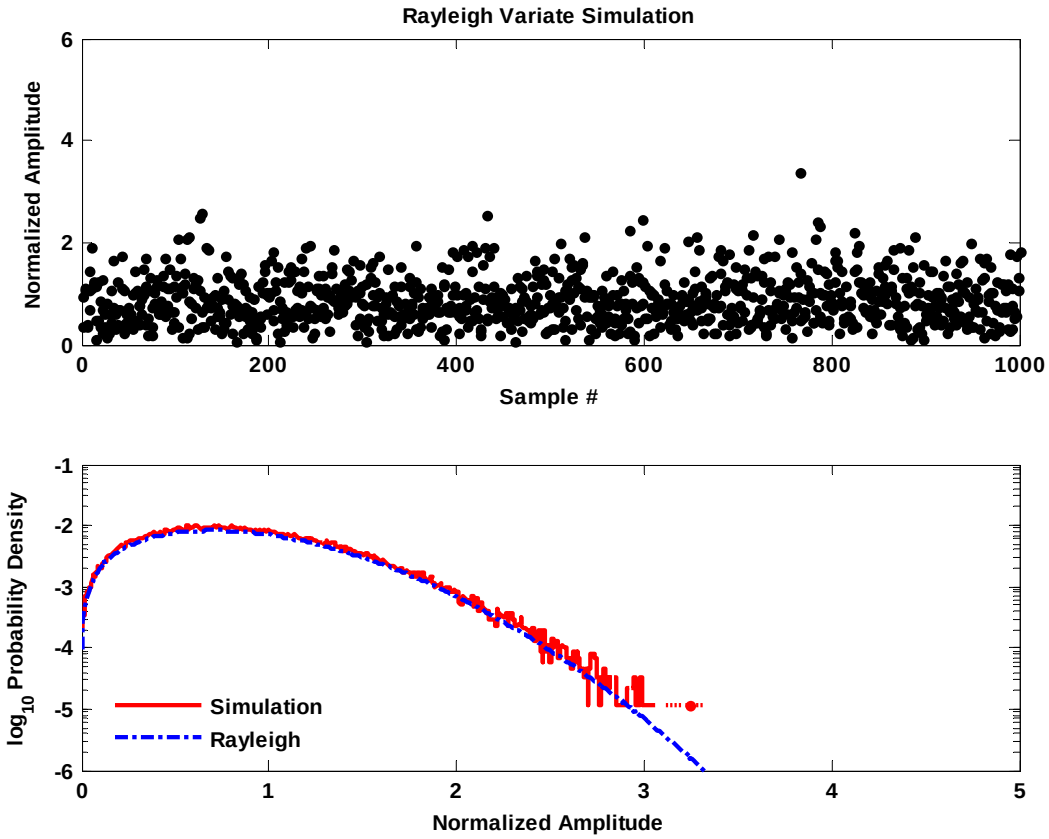

Figure 2.10: Simulated Rayleigh variates (top) and Normalized Amplitude Probability Density (bottom).

Generation of *K*-distributed variates ($\widetilde{X}$) can be accomplished utilizing the compound representation described in [Abraham & Lyons 2004b, Ward 1981], where a

Rayleigh component ($\widetilde{Z}$) is modulated by the square root of a slowly varying Gamma distribution ($V(\alpha)$):

$$\widetilde{X}(\alpha) = \sqrt{V(\alpha)}\,\widetilde{Z}, \qquad \text{Equation 2.6}$$

where α is the K distribution shape parameter. Figure 2.11 shows a 1000 sample sub-set (top) of a single realization of 1×10^6 samples and corresponding PDF of the full sample set (bottom) for $\alpha = 2$.

While generating random variates is a simple way to simulate reverberation, it requires *a priori* knowledge of the anticipated probability distribution of the data, or must be based on analysis of collected data. Additionally, as these methods incorporate no correlation, they are limited to being a statistical representation and contribute a restricted amount of insight to the understanding of synthetic aperture images. Therefore, methods which can simulate data based on physical properties are of paramount interest.

2.4.2 Physics-Based Simulations

A heuristic method of simulating data with two-dimensional correlations has been developed for used in models to be presented in the following chapters (Figure 2.12). This method draws on prior work from several sources, but incorporates them in a unique way to simulate high-resolution synthetic aperture beamformed Sonar reverberation from rippled-sand in a computationally efficient manner (a large acoustic simulation of

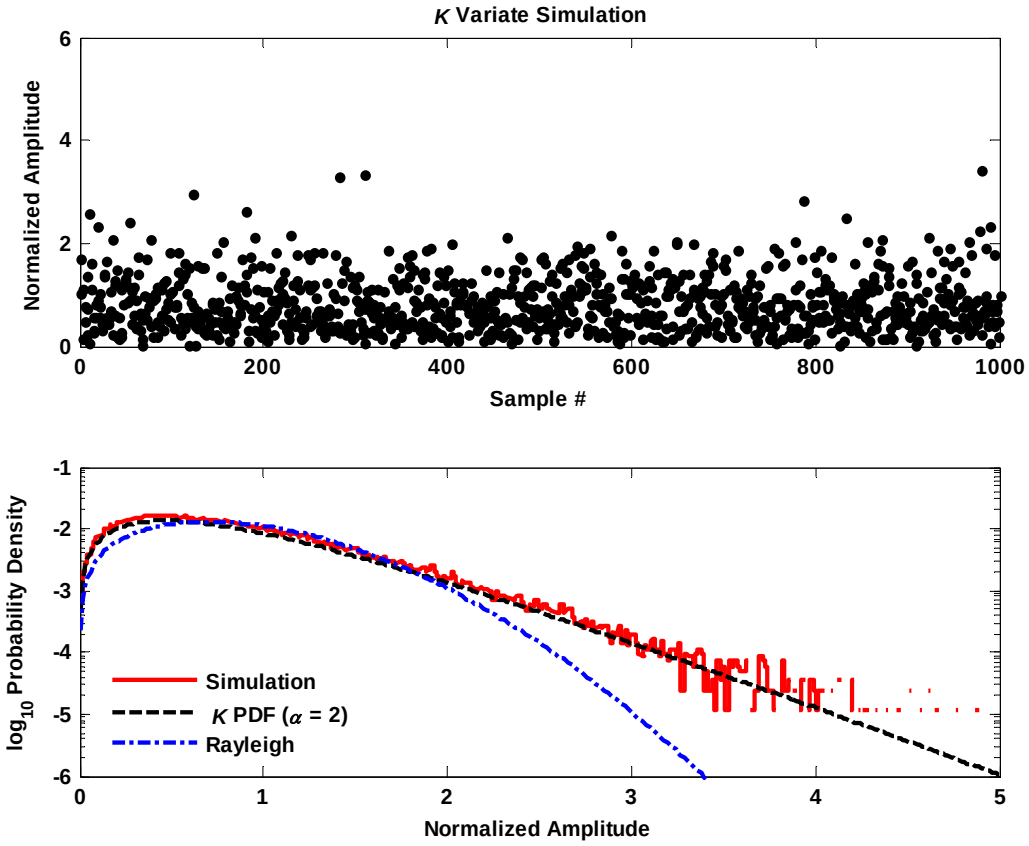

Figure 2.11: Simulated *K* variates (top) and Normalized Amplitude Probability Density (bottom).

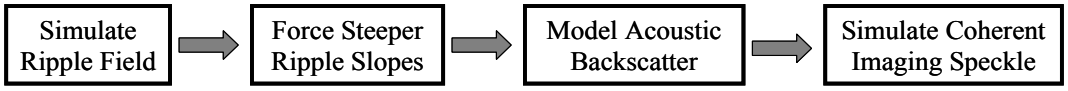

Figure 2.12: Simulation steps for sand ripple image.

approximately 8 million pixels can be computed on the order of minutes). It is important to note that no statistical form of the output normalized envelope PDF is assumed *a priori*, and the statistics of these simulations come only from assumptions made at each step of the process.

Generation of random surfaces with correlations in two-dimensions is a topic of significant interest, and non-trivial to implement. The method here begins with the work of [Tang *et al*. 2009] which is used to generate a two-dimensional ripple field with non-fading characteristics (*i.e.* the ripple heights do not fade to the mean at bifurcation points). Figure 2.13 shows a simulated ripple-field and corresponding two-dimensional wavenumber spectrum where $V_{x,y}$ represents spatial frequency with units of m^{-1}. A unique property of simulations based in the spatial frequency domain is that the resulting image is spatially-harmonic. Thus, a large surface can be generated by tiling several smaller surfaces without discontinuities at the junctions. The surface generated is symmetric with respect to zero mean height. That is, both the crests and troughs of the ripples are equidistant from the mean. Actual wave-generated sand ripples are rarely symmetric, often having a steeper slope with wider troughs and narrower crests than what is generated by the methods of [Tang *et al*. 2009]. [Lyons *et al*. 2002] shows the height h of wave-generated sand ripples at position x can be closely approximated by a Stokes wave with three harmonics,

$$h(x) = -a\cos kx + \frac{1}{2}ka^2\cos 2kx - \frac{3}{8}k^2a^3\cos 3kx \qquad \text{Equation 2.11}$$

where k is the spatial wavenumber and a is a parameter of the polynomial expansion, with $ka \approx 0.48$ in this case (ka is based on the maximum steepness the medium can support, with $ka_{max} \approx 0.44$ assumed for sea-surface water ripples). A sample realization of this surface with $k = 5.5$ is shown in Figure 2.14, and will serve as a benchmark. Implementation of Equation 2.11 for a random two-dimensional correlated surface requires generating harmonics and appropriately accounting their phase in the random two-dimensional wavenumber spectra, and has not yet been accomplished. As a workaround, harmonics which are phase-locked to the fundamental can be forced by rectifying the original surface (*i.e.* the negative of the absolute value of the previous step). This rectification effectively halves the wavelength in both dimensions, but can be accounted for in the previous step. Principles of Fourier decomposition state an infinitely steep slope in the spatial or time domain (*i.e.* a discontinuity) requires an infinite number of harmonics with decreasing amplitude in the corresponding frequency domain, which is clearly seen in Figure 2.15. The infinite steepness here is then smoothed by eliminating higher order harmonics (Figure 2.16), with the lowest three harmonics having relative amplitudes similar to the Stokes wave given in Equation 2.11. Figure 2.17 shows a single realization along the x-axis, with the normalized height distribution for the whole surface, both of which are in good agreement with [Lyons *et al*. 2002] for observed wave-generated sand ripples.

At this point, it is assumed the backscattered acoustic energy of each image pixel is primarily determined by the average slope of the seafloor within the corresponding

Sonar resolution cell with respect to the backscattered direction. This slope is simply the change in height between pixels with respect to range including the grazing angle to the Sonar, which is typically on the order of 10 degrees or less for high-contrast SAS images. The acoustic response to each Sonar resolution cell is then estimated using a polynomial expansion fit to the rough surface backscattering model of [Mourad & Jackson 1989, Mourad & Jackson 1993, Jackson 2007] (which is a combination of the small-roughness perturbation method for low grazing angles and the Kirchoff or tangent-plane approximation for near-normal grazing) for computational speed. For the simulations here, the modeled acoustic response was based on the sand properties given in [Richardson *et al*. 2001, Williams *et al*. 2002, Jackson 2007] (Table 2.1), approximated with a 5^{th} order polynomial (Figure 2.18). A much higher order polynomial (about 20^{th} order for this case) would be required to capture the structure of the critical angle seen in the model, significantly increasing the computation time. It can be argued such a clearly defined critical angle is rarely seen in experimental backscattered acoustic data. A signal to noise ratio (SNR) of 45 dB is then specified by adding Gaussian distributed 'white' noise to simulate background environmental and system noise.

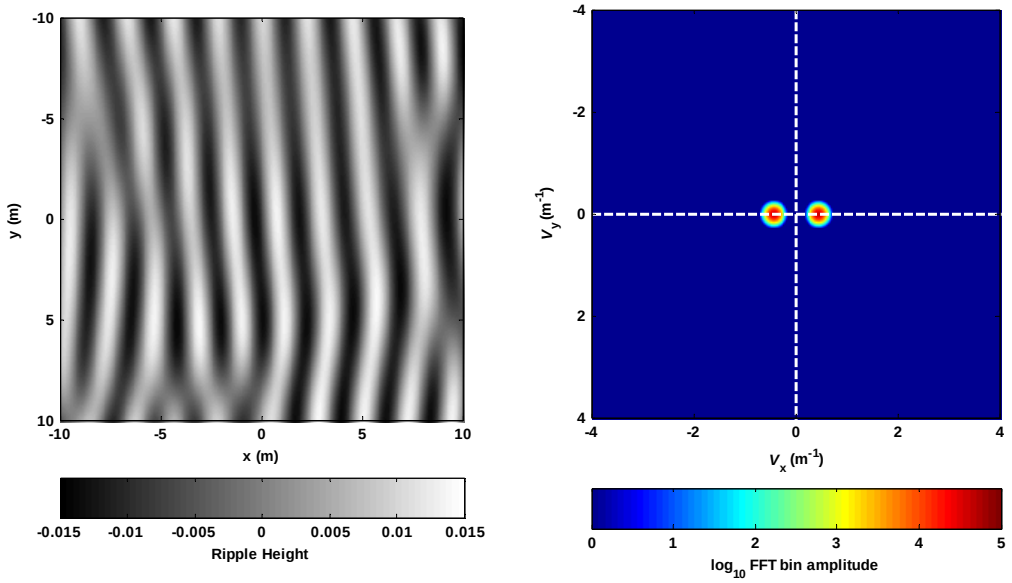

Figure 2.13: Simulated ripple field (left) and corresponding two-dimensional wavenumber spectrum (right).

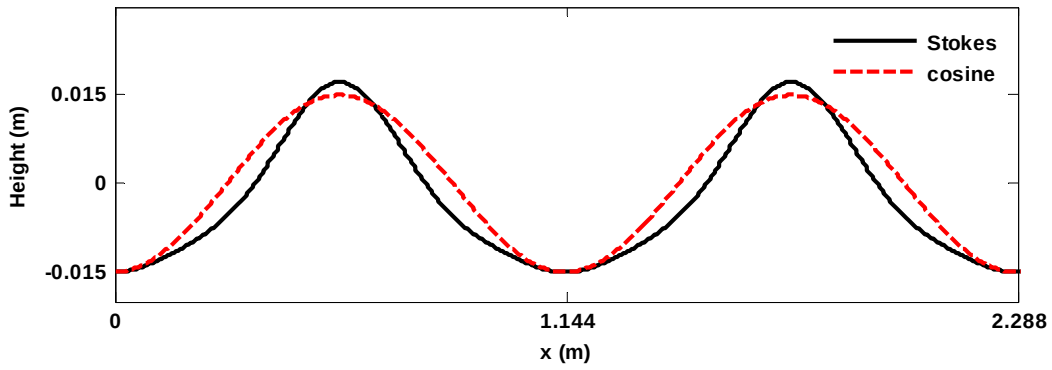

Figure 2.14: Realization of Stokes ripples (solid black) versus cosine (dashed red) (Equation 2.11).

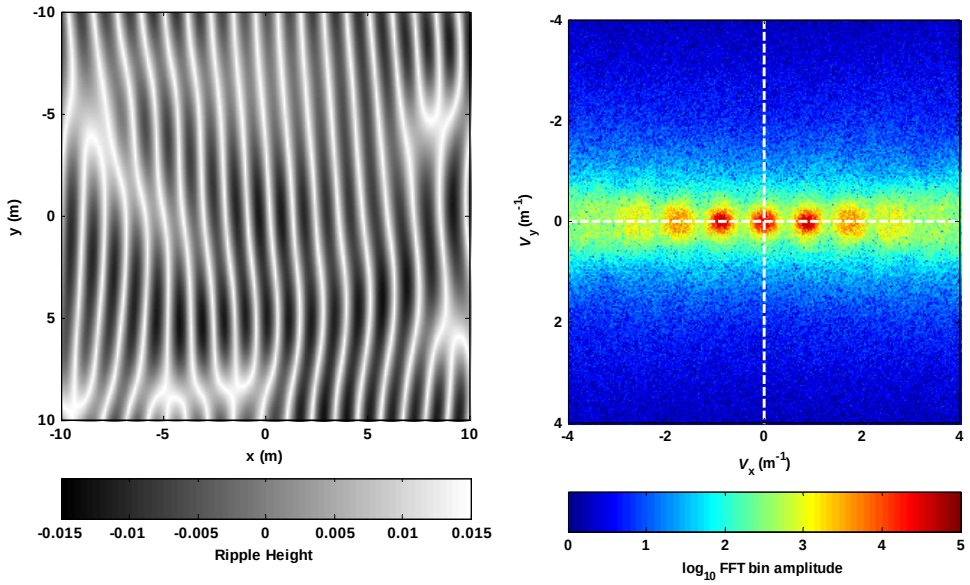

Figure 2.15: Rectified ripples of Figure 2.14 (left) and corresponding two-dimensional wavenumber spectrum (right).

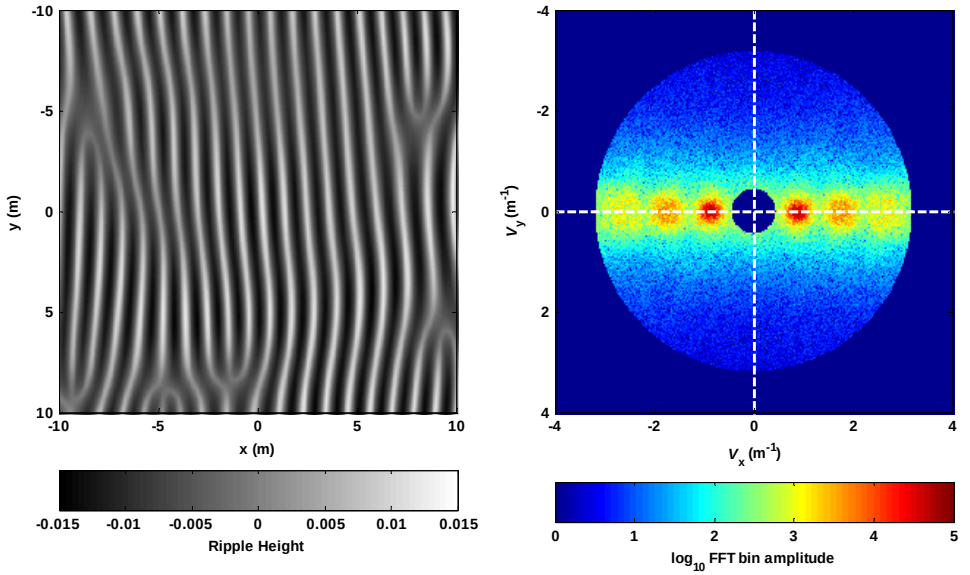

Figure 2.16: Filtered spectrum ripples of Figure 2.16 (left) and corresponding two-dimensional wavenumber spectrum (right).

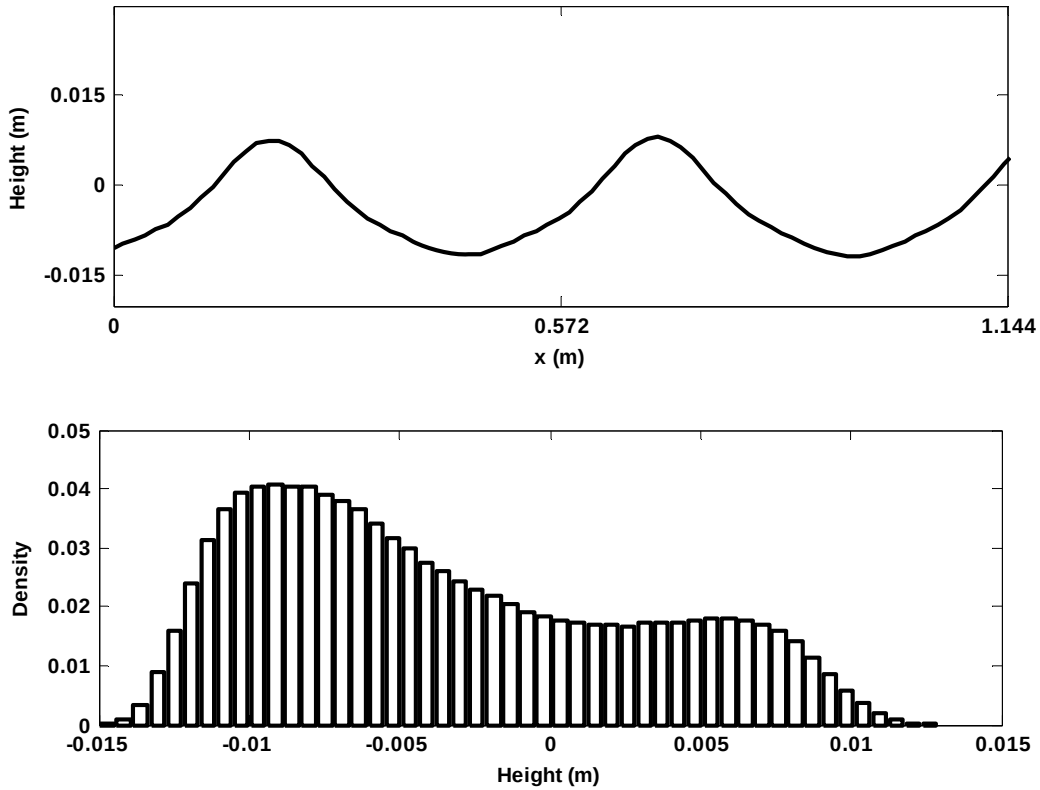

Figure 2.17: Example height field of simulation (top) and full image height histogram (bottom).

Table 2.1: Sediment properties used in simulations.

Property		**Value**
Sediment / Water Density Ratio	ρ	2.00
Sediment / Water Sound Velocity Ratio	v	1.16
Attenuation	δ	0.01
Power Law Exponent	$\gamma 2$	3.04
Power Law Spectral Strength	$w2$	4.33×10^{-5}

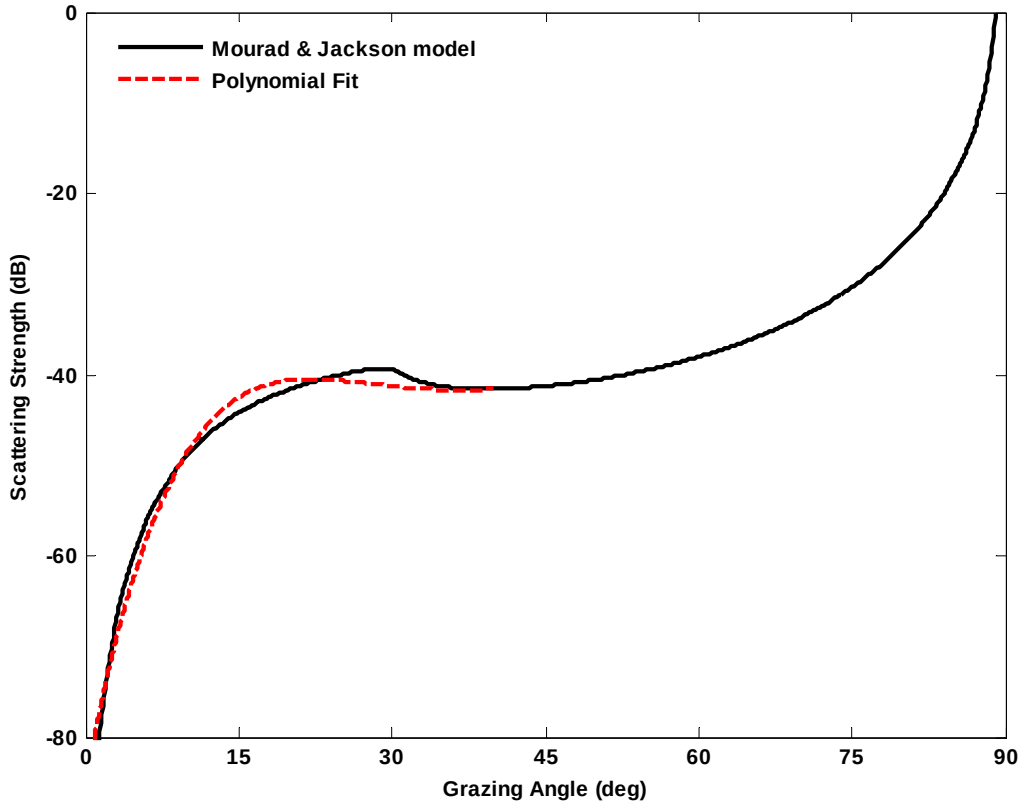

Figure 2.18: Rough surface backscattering model (solid black) and 5th order polynomial fit used in simulation (dashed blue).

The final step is to simulate speckle, which is well documented in the optics and Radar literature, with a few references for speckle mitigation in SAS images [Chanussot *et al.* 2002, Fortune *et al.* 2003]. Speckle is the result of constructive and destructive interference of the wavefronts scattered by a rough surface, and bears no relationship to the macroscopic properties of the ensonified surface [Goodman 1976] (Figure 2.19). This interference pattern is the result of random phase perturbations of the wavefronts from individual scatters within the resolution cell which are superimposed during the coherent imaging process [Goodman 2000, Goodman 2005]. Figure 2.20 shows

autocorrelation coefficients in both the along-track (*i.e.* parallel to ripple crests) and range (*i.e.* perpendicular to ripple crests) of Figure 2.19 showing de-correlation after 1-2 resolution cells [Skinner 1963]. [Goodman 2007] gives a simple algorithm for generating speckle (Figure 2.21) utilizing the inverse Fourier transform of a two-dimensional random phase spectra (a similar method is presented in [Gascón & Salazar 2006] for simulating diffraction patterns by specifying the amplitudes and speckle patterns by specifying the random phases of an inverse Fourier transform). When the speckle process is driven by a second compounding random process, the resulting phenomenon can be considered 'compound' speckle and has been shown to lead to the *K* distribution [Jakeman & Pusey 1976, Goodman 2007]. These second random processes (roughness of the scattering surface being the first), can be the result of a turbulent medium or errors in platform motion compensation. It is also hypothesized that a second order scattering feature (*e.g.* sand-dollars on rippled sand, Figure 2.22) may also produce a something resembling compound speckle, however this requires additional consideration and validation with experimental data. Speckle observed in the SAS image of Figure 2.19 have greater distance between peaks than Figure 2.21, and appear more like the compound speckle of Figure 2.23. For these reasons, compound speckles, with two independent realizations multiplied together, are used for this simulation. The acoustic response of the sand ripples simulated previously is then multiplied by this compound speckle to produce the final image. A visual comparison is given as Figure 2.24 and statistical comparison as Figure 2.25, both showing good agreement between collected data and the numerical simulation presented here over a wide range of orientation angles.

It is anticipated that the method outlined here for simulation of a rippled-sand SAS image can be expanded to incorporate alternative scattering mechanisms such as volume scattering or sediment inhomogeneties. Additionally, this method may be expanded to model specific system beampattern and beamforming techniques, and system specific speckle properties. These extensions require additional investigation.

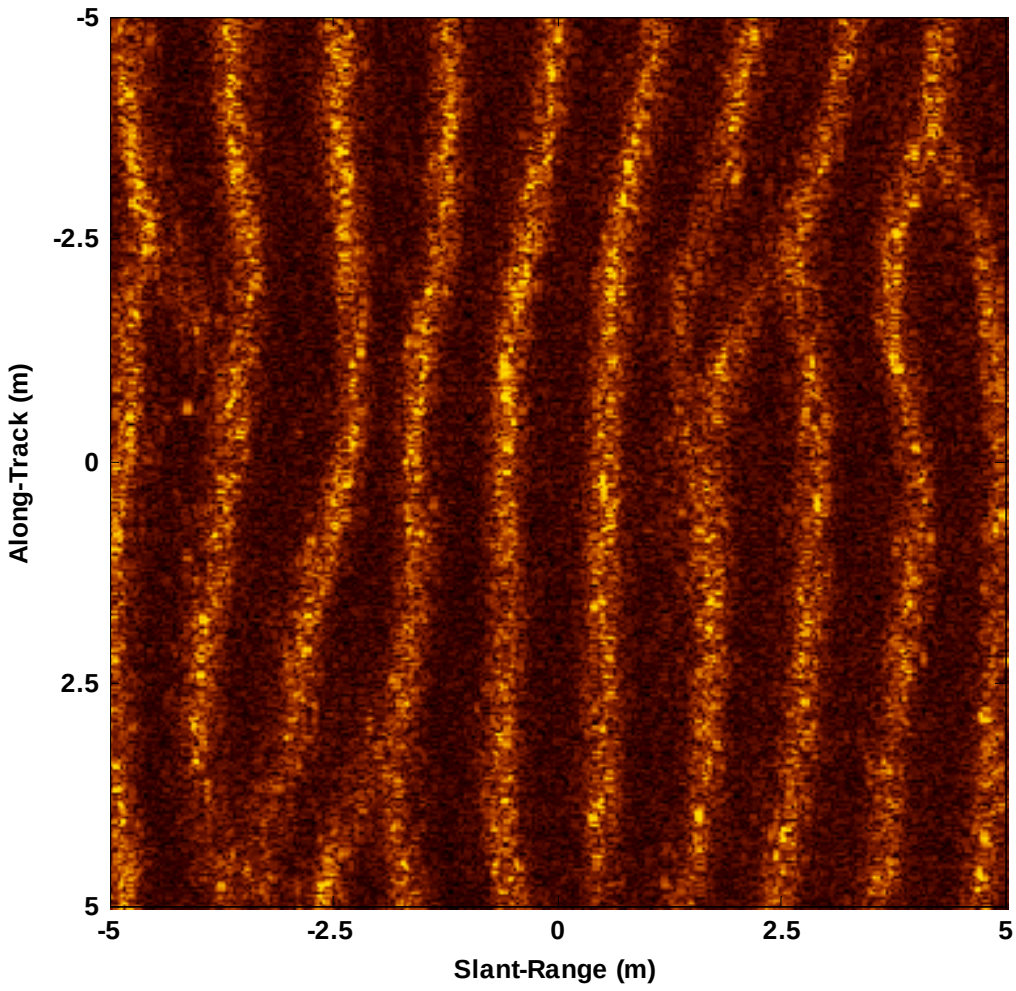

Figure 2.19: Close up of Figure 1.1 showing coherent imaging speckle.

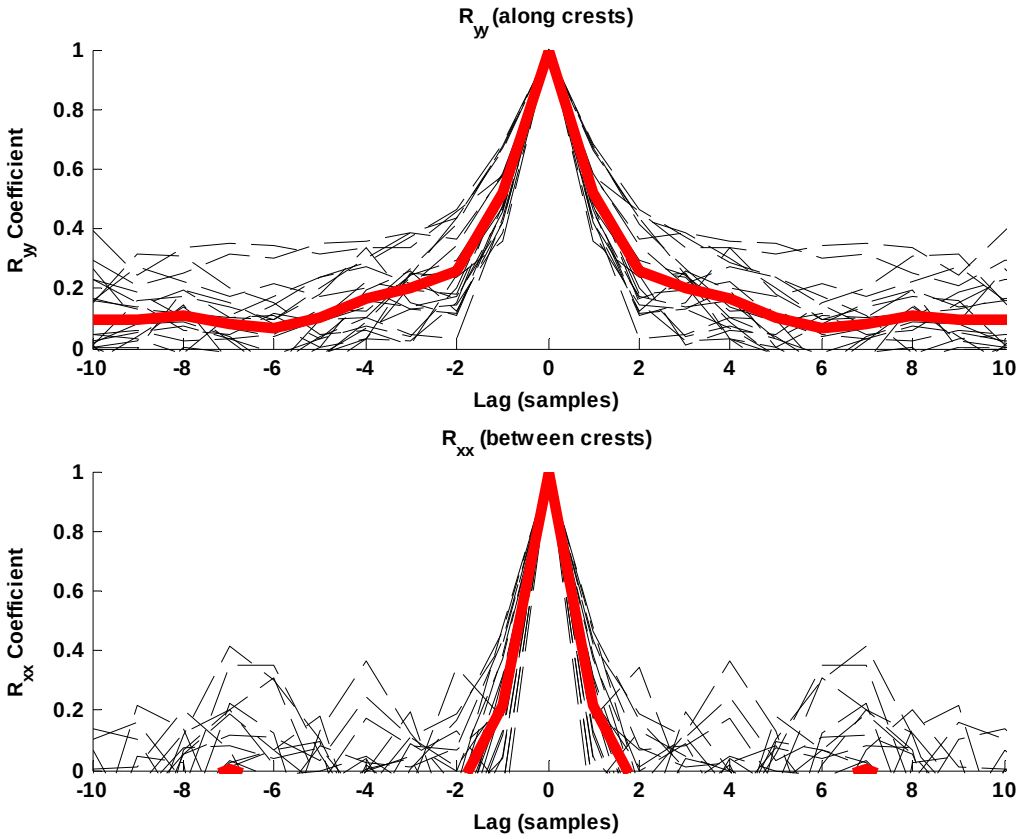

Figure 2.20: Autocorrelation of image speckle of Figure 2.19.

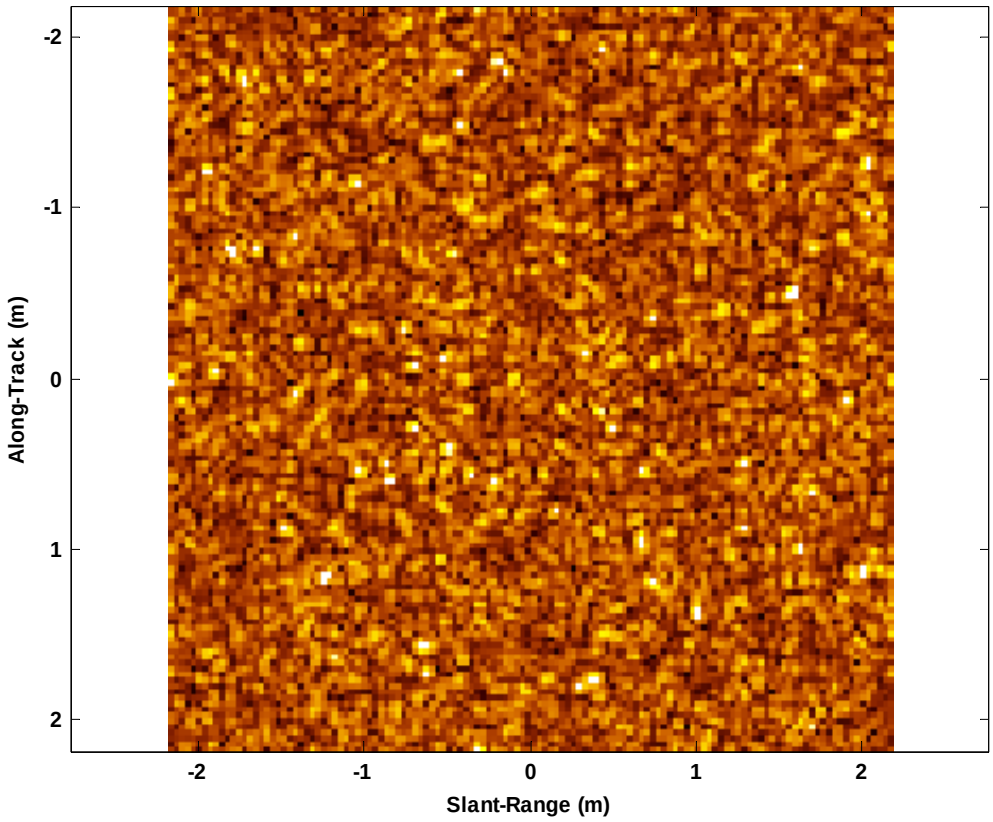

Figure 2.21: Simulated speckle.

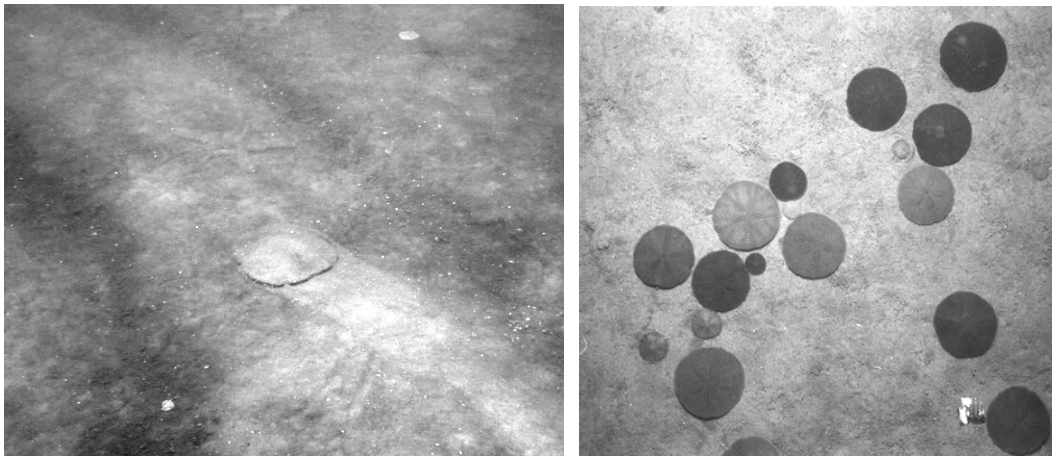

Figure 2.22: Sand dollars on a rippled sand surface. (left photo courtesy of the Applied Physics Lab – University of Washington, right photo courtesy of the USGS)

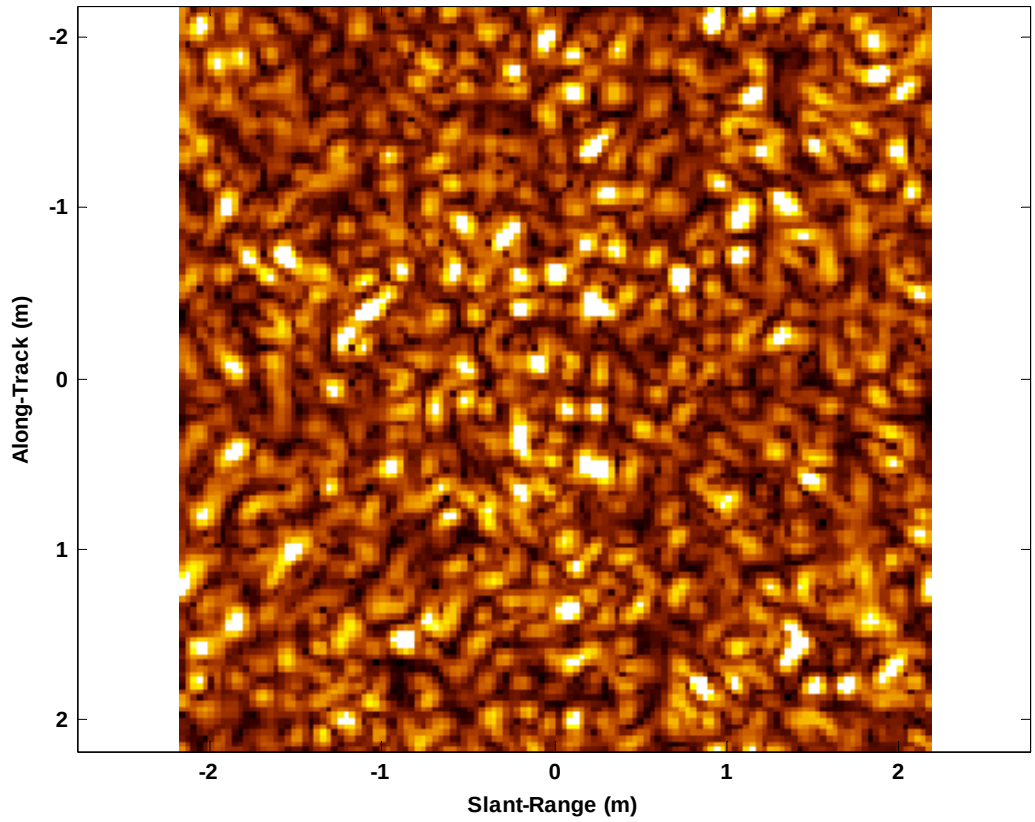

Figure 2.23: Simulated compound speckle.

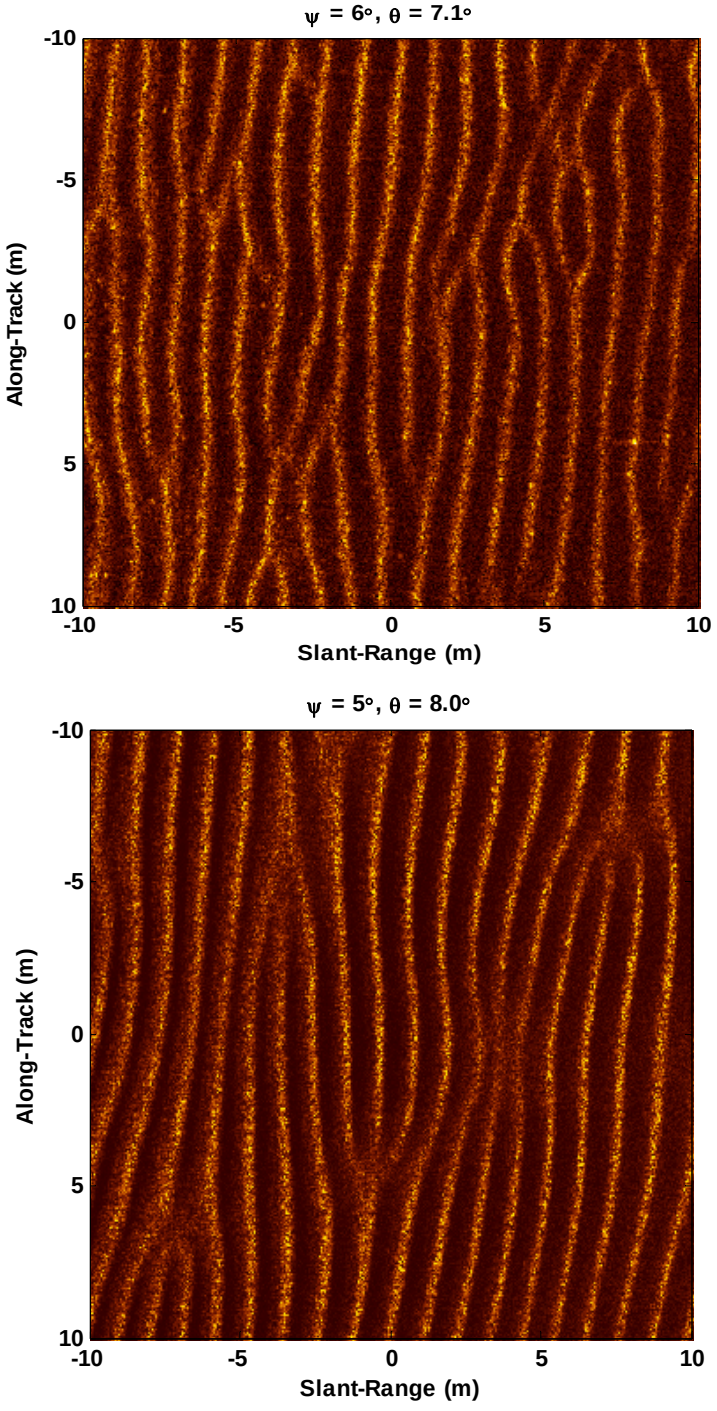

Figure 2.24: Comparison between experimental (top) and simulated image (bottom).

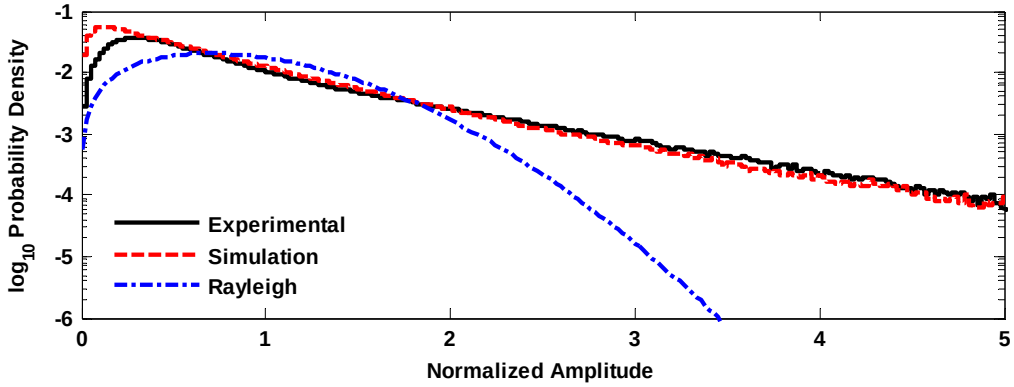

Figure 2.25: Comparison of PDF's using estimated shape parameters for experimental (solid black) and simulated (dashed red) images, and the Rayleigh distribution (dot-dashed blue).

Chapter 3

Impact of Multipath on SAS Image Statistics

3.1 Chapter Introduction

As with traditional sonar, Synthetic Aperture Sonar (SAS) is susceptible to multipath contamination, reducing the quality and also modifying the statistics of the image. Such multipath contaminants may either be environmentally induced, as is often the case when attempting to image ranges greater than the water depth, or may be induced by the system's supporting structure itself. Multipath tends to fill in shadows which are critical for image classification algorithms, may 'ghost' targets (*i.e.* multipath causes a single target to appear in multiple false locations of the image) increasing the Probability of False Alarm, and can affect data-driven micro-navigation which is critical for correction of platform motion in some Sonar systems [Johnson *et al*. 1995, Bellettini & Pinto 2002, Bellettini *et al*. 2003]. Therefore, a clear understanding of the statistical impact of multipath is necessary to advance image formation algorithms and for predicting system performance for both traditional and synthetic aperture Sonar.

Previous research on the effects of multipath on reverberation statistics has been limited to the development of theoretical models [LePage 2004, Abraham & Lyons 2004b, Abraham 2007] and circumstantial rather than conclusive evidence in experimental data analysis [Preston & Abraham 2004, Lyons *et al*. 2005]. Research

specific to SAS has generally been limited to reducing the impact of multipath with various schemes to increase vertical resolution by increasing physical aperture or by beam-steering [Bellettini *et al*. 2003, Hayes 2004, Pinto *et al*. 2004, Bellettini & Pinto 2008, Chen *et al*. 2008], or by development of models to anticipate target image degradation from surface multipath [Davis *et al*. 2002]. It is typically difficult or impossible to isolate the effects of propagation from those of bottom scattering or the effect of Sonar system parameters, particularly for long-range systems where propagation can be complicated and narrow bandwidths which often yield inseparable multipath. The constant resolution with range property of synthetic aperture data along with wide bandwidth transmit waveforms provides a unique opportunity for statistical analysis of environmental properties such as multipath, and affords a framework for extending analytic modeling and numerical simulation. We begin first with a model for multipath as a mixing process, followed by analysis of structural and environmentally induced multipath, and conclude with simulation methods.

3.2 Multipath as a Mixing Process

Visually, multipath reduces the overall image quality. Statistically, multipath serves to increase the randomness of the reverberation, decreasing the envelope PDF tails (*i.e.* producing statistics that are more Rayleigh-like). The multipath phenomena can be modeled by considering the method of images concept for acoustic sources near boundaries [Medwin & Clay 1998, Kinsler *et al*. 2000], modified for co-located source and receiver (Figure 3.1). In such a configuration, only the direct path acoustic energy is

expected (*i.e.* that which propagates from the source to the seafloor, and is backscattered to the receiver), and slant-range is a function of two-way propagation time. However, at two-way propagation times corresponding to the distances to the boundaries, additional energy from source images arrives concurrently with the direct path. In an effort to minimize these source images from distorting the intended signal, systems are typically designed with vertically narrow transmit and/or receive beampatterns. However, narrow beamwidth systems are often limited by transducer size (or array lengths) or by requirements for a broad main-lobe for adequate coverage. Additionally, even when systems do possess significant off-axis rejection, the backscattering properties of the seafloor may cause multipath levels to retain enough energy to influence imaging of the direct path. Often the direct-path is backscattered from the seafloor at a very low grazing angle, while multipath is backscattered nearly-normal to the seafloor. Considering Figure 2.18, the roughness model for the backscattering strength of a typical sand seafloor yields a direct-path backscattered level -45 dB or less than normally arriving multipath, which would require vertical side-lobes to achieve greater than 45 dB of off-axis rejection – a challenging design feat. In actuality, while this scenario may produce minimal observable distortion of the direct-path, to avoid statistical impact the level would need to be reduced by another 10 dB.

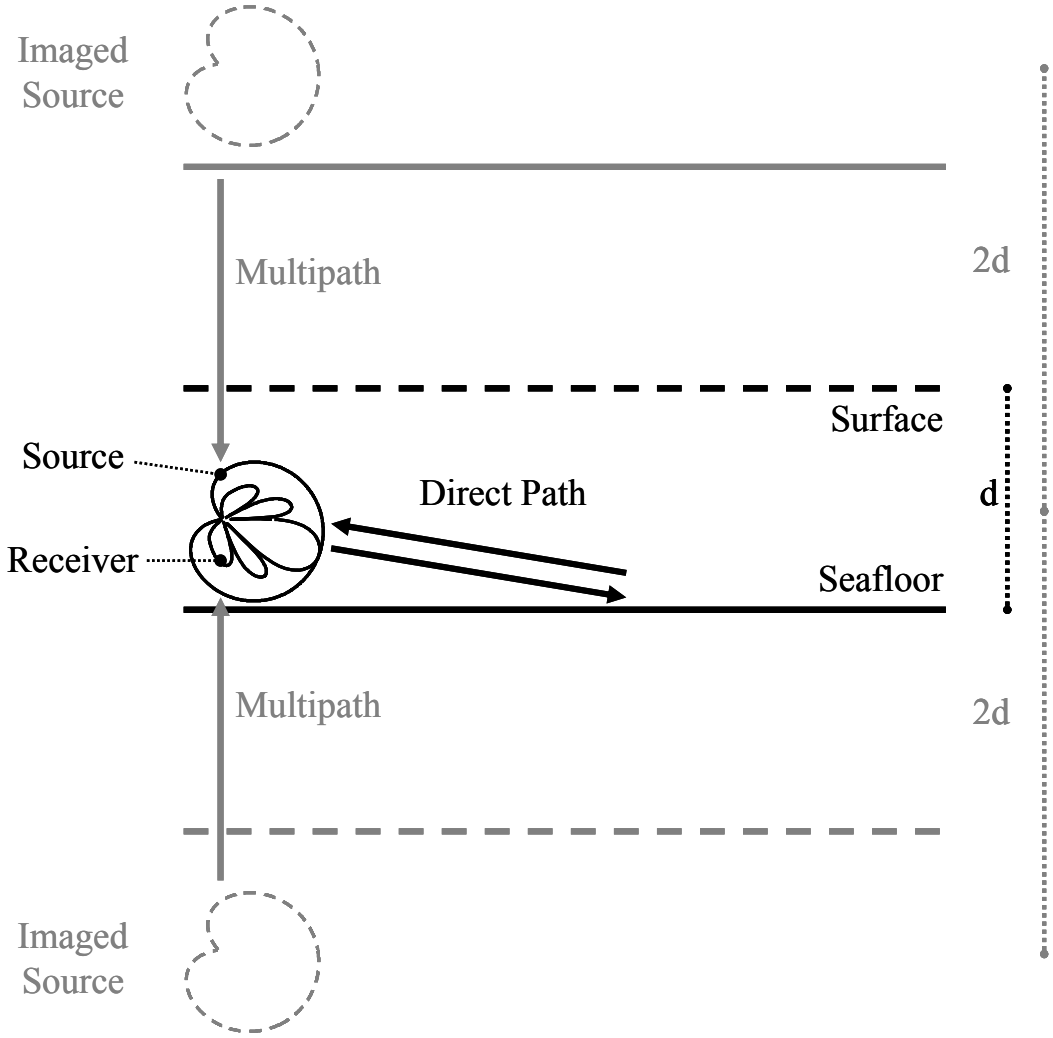

Figure 3.1: Side-view diagram of actual source and receive beampatterns, and source images contributing to multipath contamination.

Returning to the classical reverberation definition of Equation 1.18, multipath can be thought of as a summation of acoustic energy originating from the original source and the source images propagating through the boundaries, in this case the sea-surface and/or the seafloor. As the seafloor is typically a rough surface and the sea surface may be both rough and time-varying, the multipath can be modeled as a random process. The two extreme cases for this model are *K*-distributed with an identical shape parameter as the

direct path or Rayleigh-distributed, corresponding to coherent or completely random incoherent boundary reflection respectively. Thus, multipath can be modeled as the mixing of two or more statistical distributions with varying power levels based on the angle-dependant boundary backscattering strength and beampattern responses. Derivation of the equivalent *K* distribution shape parameter from mixing of Rayleigh and/or *K* distributions by matching higher order moments may be found in [Watts 1987, Abraham 2007, Lyons *et al*. 2009].

Considering the case where both the direct-path and multipath returns exhibit *K*-distributed PDFs with the same shape parameter, the equivalent shape parameter of the combination may be derived from the results of [Abraham 2007]. With the assumption that there is no change in area of the ensonified cell with grazing angle as a result of SAS processing, setting the shape parameter of the individual components to α_0, and adapting the results to our situation results in the equivalent *K* distribution shape parameter ($\tilde{\alpha}_{K\,MP}$):

$$\tilde{\alpha}_{K\,MP} = \alpha_0 \left(\frac{\left(P_{DP} + \sum P_{MPn} \right)^2}{P_{DP}{}^2 + \sum P_{MPn}{}^2} \right) \qquad \text{Equation 3.1}$$

where P_{MPn} represents the power of the n^{th} independent multipath return, P_{DP} represents the power of the direct path, and α_0 is the shape parameter of the direct path return. The case where the multipath exhibits a Rayleigh-distributed envelope is presented in detail in

[Watts 1987] for *K*-distributed radar clutter in the presence of thermal noise, and adapted in [Lyons *et al*. 2009] to model reverberation from patches on a Rayleigh background for heterogeneous seafloors. Using these results with the multipath taking the place of the background terms, the equivalent *K* distribution shape parameter ($\widetilde{\alpha}_{RMP}$) is:

$$\widetilde{\alpha}_{RMP} = \alpha_0 \left(1 + \frac{\sum P_{MPn}}{P_{DP}} \right)^2 . \qquad \text{Equation 3.2}$$

Figure 3.2 demonstrates the results considering multipath as a mixing of statistical distributions; the solid black line represents *K*-distributed multipath (Equation 3.1) the dashed blue line represents Rayleigh-distributed multipath (Equation 3.2) mixed with a *K*-distributed direct-path. As the power level of the 2nd PDF (*e.g.,* the multipath) is increased with respect to the first (*e.g.,* direct-path) the normalized equivalent shape parameter increases until the distributions are of equal level. If the level of the 2nd PDF is increased additionally, the resulting mix of distribution will be primarily dominated by the 2nd PDF. This is seen as the *K*+*K* PDF returns towards a normalized equivalent shape parameter of 1.

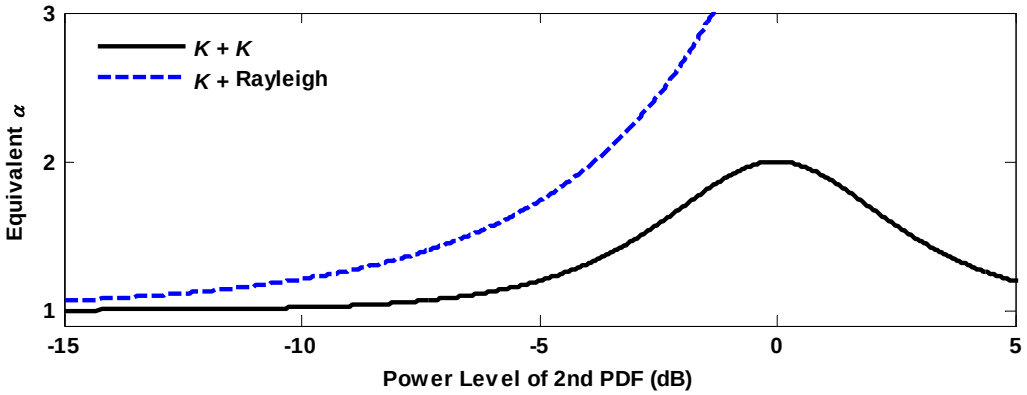

Figure 3.2: Equivalent shape parameter when mixing a *K*-distributed direct-path (α = 1) with a *K*-distributed (α = 1) (solid black) or Rayleigh-distributed (dashed blue) multipath of varying power level.

An alternative method for estimating the equivalent statistics for multiple mixed distributions is to compute the resulting distribution numerically, which provides nearly identical results to the analytically derived moment matching equations given in Equations 3.1 and 3.2. Utilizing the random variate generation methods given in the previous section, any number of distributions each with independent power levels and statistical properties, each representing a specific multipath arrival, can be mixed coherently, with statistical parameter estimation performed on the result. This can be applied to any of a number of distributions, not limited to Rayleigh and *K*, can provide a solution when a moment matching solution does not exist.

To aid in understanding of multipath as a mixing process, we can return to the Random Walk analogy for reverberation. A *K*-distributed direct-path can be thought of as a biased random walk in a particular direction, while the multipaths can be thought of

as either a biased random walks in different directions for the case of *K*-distributed multipath, or completely random (*i.e.* unbiased) walks for the case of Rayleigh-distributed multipath. If we combine these walks, the resulting direction will always be more random than the original. As the number of combined walks goes to infinity, the result would be completely random following the Central Limit Theorem. Thus, reverberation containing multipath should be less non-Rayleigh than direct-path reverberation which contains a single realization of the same seafloor. Theoretical models and simulation analysis yields essentially the same result [LePage 2004, Abraham & Lyons 2004b, Abraham 2007].

3.3 Structure-Scattered Multipath

3.3.1 Analysis of SAX04 Data

Figure 3.3 is an example synthetic aperture formed image from 30-50 kHz SAX04 data. Sand ripples, regions of high backscatter, a flush buried sphere (at approximately 9.8 m range and -5.2 m cross-range), and rippled sand are clearly visible. Of particular interest for this section are the lines across the image at 17.9 m range and those just preceding, which are examples of the visual impact of multipath contamination. These lines are the result of energy scattered by the rail and mobile-tower structure which then interacts with the boundaries, arriving concurrently with the intended direct-path at slant-ranges corresponding to time of arrival. The dominant early scattering (Figure 3.4) arrivals of interest for this discussion are labeled: A – structural reflection, B –

electronics package reflection, C-D – multiple arrivals at or just above the seafloor from the rail and mobile-tower structure. These early reflections then interact with the boundaries (seafloor and/or sea-surface) (Figure 3.5) to create the false fathometer-like returns observable just prior to the true fathometer return at 17.9 m.

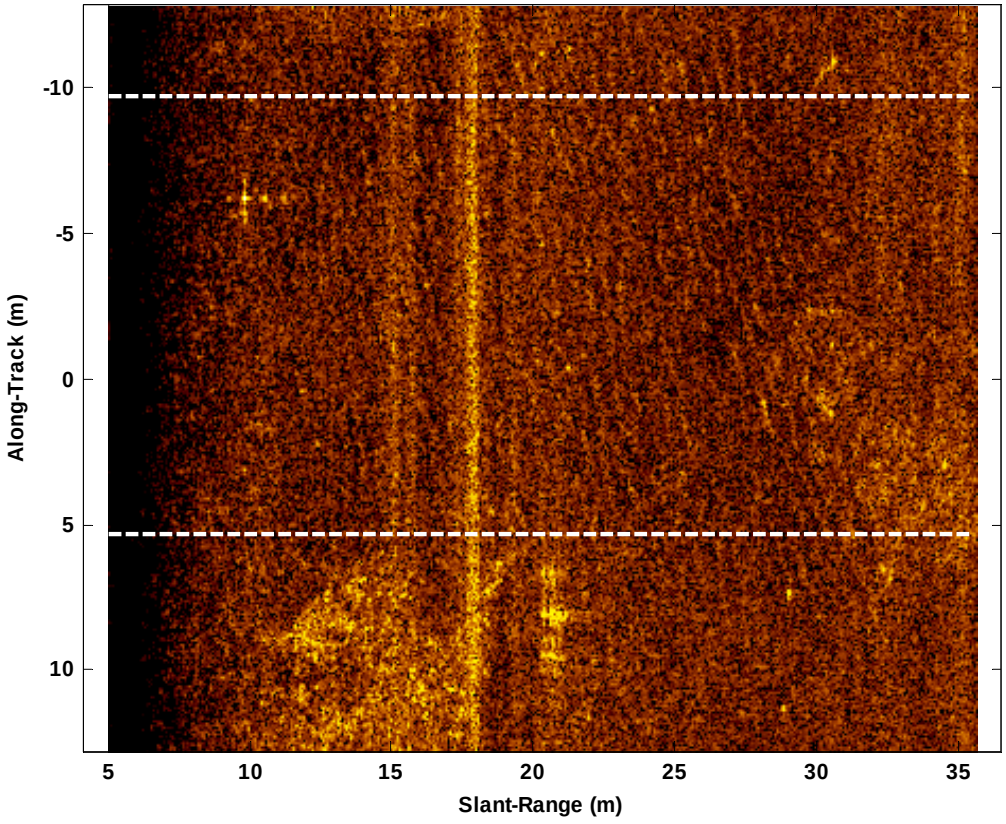

Figure 3.3: 30-50 kHz SAS image from SAX04 with structure-scattered multipath clearly visible between 15 and 18 m slant-range.

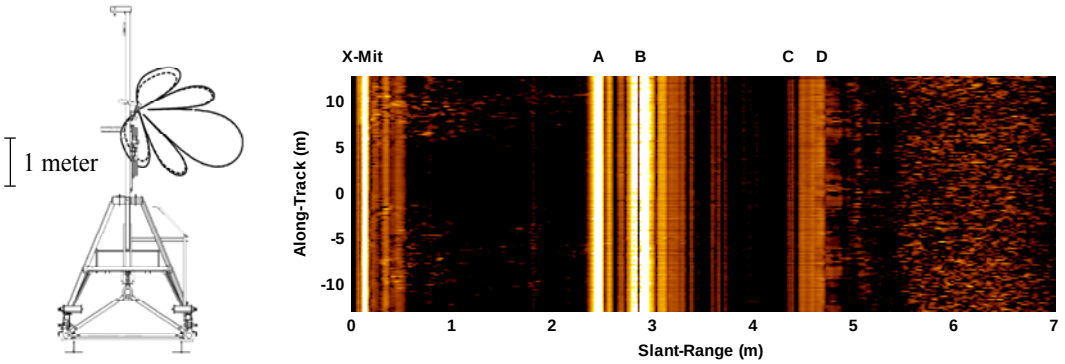

Figure 3.4: Side-view scale drawing of rail and mobile tower with analytical beampatterns superimposed (30-50 kHz solid, 60-100 kHz dashed) (left), and early reflections from structural scattering (right) (scale drawing courtesy of the Applied Physics Lab – University of Washington).

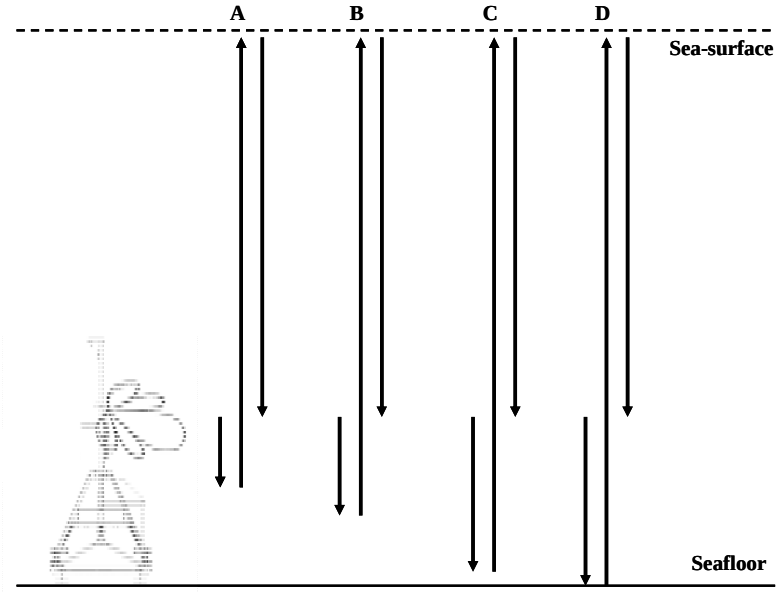

Figure 3.5: Reflections from structural features, electronics case, rail, and seafloor resulting in multipath (A, B, C, and D respectively). Note water depth is not to scale.

After SAS image formation, images were normalized to unit mean power removing gross power fluctuations, including the increase attributed to the multipaths at 17.9 m slant-range (Figure 3.3). Any areas containing objects or that exhibited statistics different from the overall image were excluded from further processing. The data used are bounded by dashed lines of Figure 3.3 (note: the flush buried sphere at 9.8 m slant-range and -5.2 m along-track is outside the analysis ranges presented here). The *K* distribution shape parameter and Scintillation Index were then estimated as a function of range using a sliding window to increase sample size in an attempt to minimize variance without unduly sacrificing spatial resolution (the analysis window was approximately 0.6 m in range by 15 m in cross-range with at least 10,000 samples per estimate). Figure 3.6 shows a synthetic aperture image formed from 30-50 kHz acoustic data and a 1 cm vertical aperture receiver with data selected for statistical analysis bounded by dashed lines (top), and estimated *K* distribution shape parameter as a function of range (bottom). Similarly, Figure 3.7 shows an image and statistical analysis using 60-100 kHz data collected with a 5 cm vertical aperture receiver.

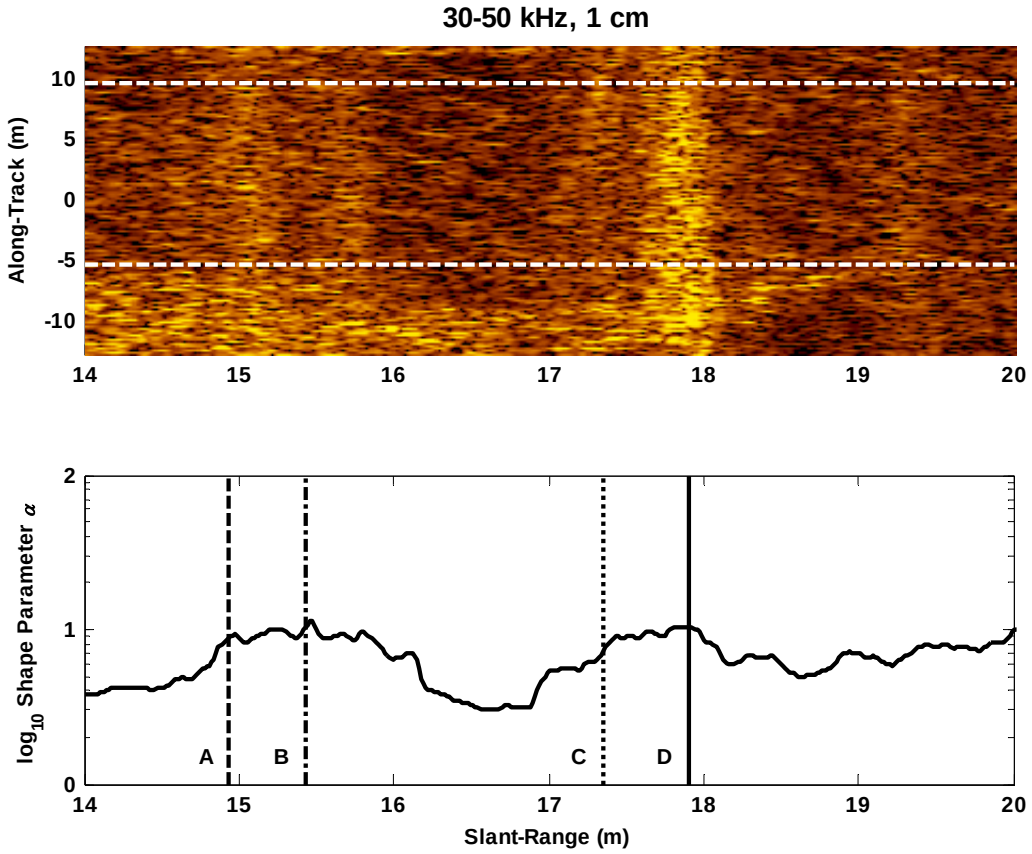

Figure 3.6: SAS image formed from 30-50 kHz acoustic data collected with a 1 cm vertical aperture receiver (top) and *K* distribution shape parameter estimates vs. range (bottom).

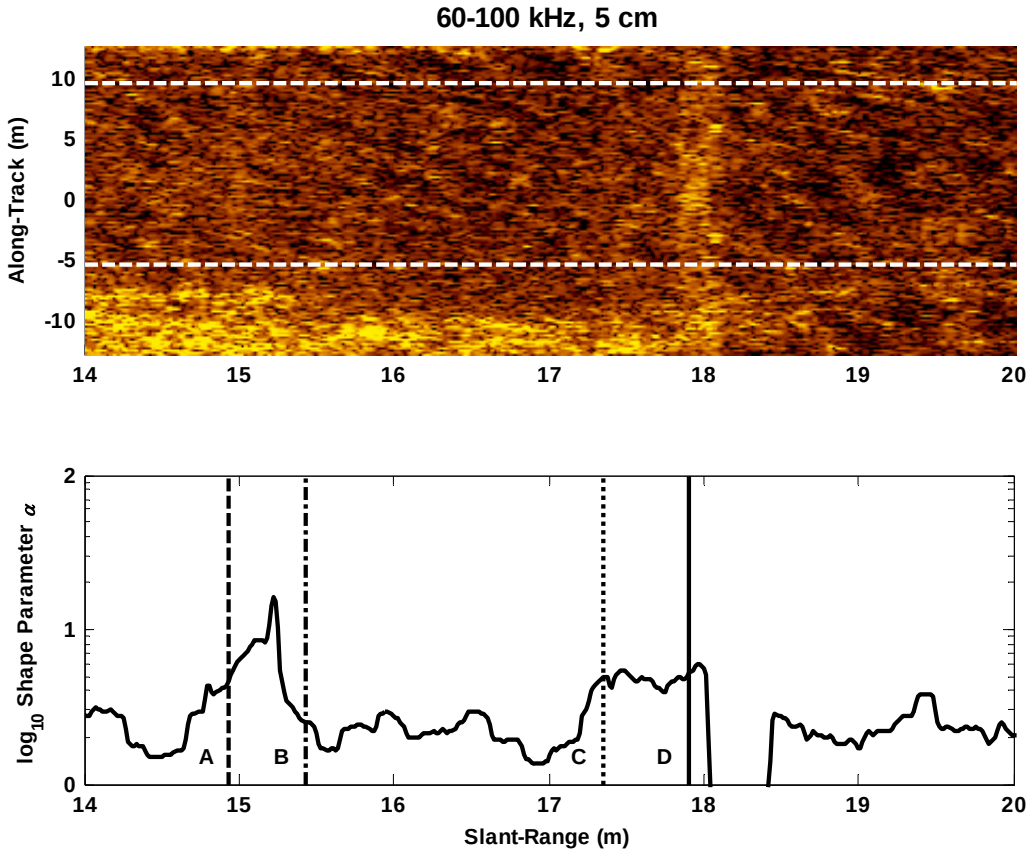

Figure 3.7: SAS image formed from 60-100 kHz acoustic data collected with a 5 cm vertical aperture receiver (top) and *K* distribution shape parameter estimates vs. range (bottom).

In Figure 3.6, multipath contamination resulting from scattering off the measurement rail near the seafloor followed by the sea-surface (or *vice versa*) is clearly observable as both a power level (top) and shape parameter (bottom) increase at 17.9 m. These increases in both power and shape parameter correspond to multiple early reflections from the rail structure and scattering from the seafloor (Figure 3.4) which then interact with the sea-surface (Figure 3.5). These spatially distributed multiple scatterers

are further stretched in range by the acoustic pulse length, the sliding window used in the statistical parameter estimation, and motion of the sea-surface. Figure 3.7 shows a similar impact slightly narrower in range with a lower resulting shape parameter because of both the shorter physical duration of the pulse and narrower beampattern. The narrower main lobe achieved utilizing a higher center frequency and larger aperture rejects more off-axis reverberation than a lower center frequency and smaller aperture. However, this tight beam pattern also reduces the useable range of the transducer for a fixed mounting angle.

Also observable in the statistical analysis of both images is an additional multipath contaminant at approximately 15 m. This corresponds to a multipath incorporating scattering off the sea-surface and a large electronics box situated approximately 3 m below the acoustic source and receivers. This additional multipath contaminant is observable visually in the 30-50 kHz SAS image of Figure 3.6 but not in the 60-100 kHz SAS image Figure 3.7 owing to narrower beampatterns of the higher frequency signal; however the statistics of both images are impacted. It should be noted that while only two examples of multipath contamination are given here, any (or all) of the early reflections shown in Figure 3.4 are capable of impacting the statistics at integer combinations of structural distance and water depth. Recalling Figure 3.2, these additional multipath contributions need not be visible to affect the statistics – a multipath with a power level of -10 dB relative to the direct path can have an impact. The complex nature of the structure and variability associated with experimental data highlight the difficulty in separating the two, and as such only two clear examples are given here. The

next section will focus on predictions of statistical impact based only on the multipath arrival at 17.9 m.

Figure 3.8 shows estimated *K* distribution shape parameter versus range for 30-50 kHz (top) and 60-100 kHz (bottom) synthetic aperture formed images around the range of the fathometer-like multipath arrivals scattered by the rail and mobile-tower structure just above and on the seafloor. All six curves show a marked increase in shape parameter because of these multipath contaminants. In general, the 60-100 kHz images exhibit a lower shape parameter across all vertical receiver apertures because of higher range resolution resulting from greater acoustic bandwidth. Additionally, for both bands, the impact of multipath is reduced with increasing vertical aperture (and subsequent narrowing of the vertical beampattern). The width of the impact is dependent upon the location of the scattering structures, the bandwidth of the transmitted acoustic signal (which defines the range resolution), and also the size of the sliding estimation window.

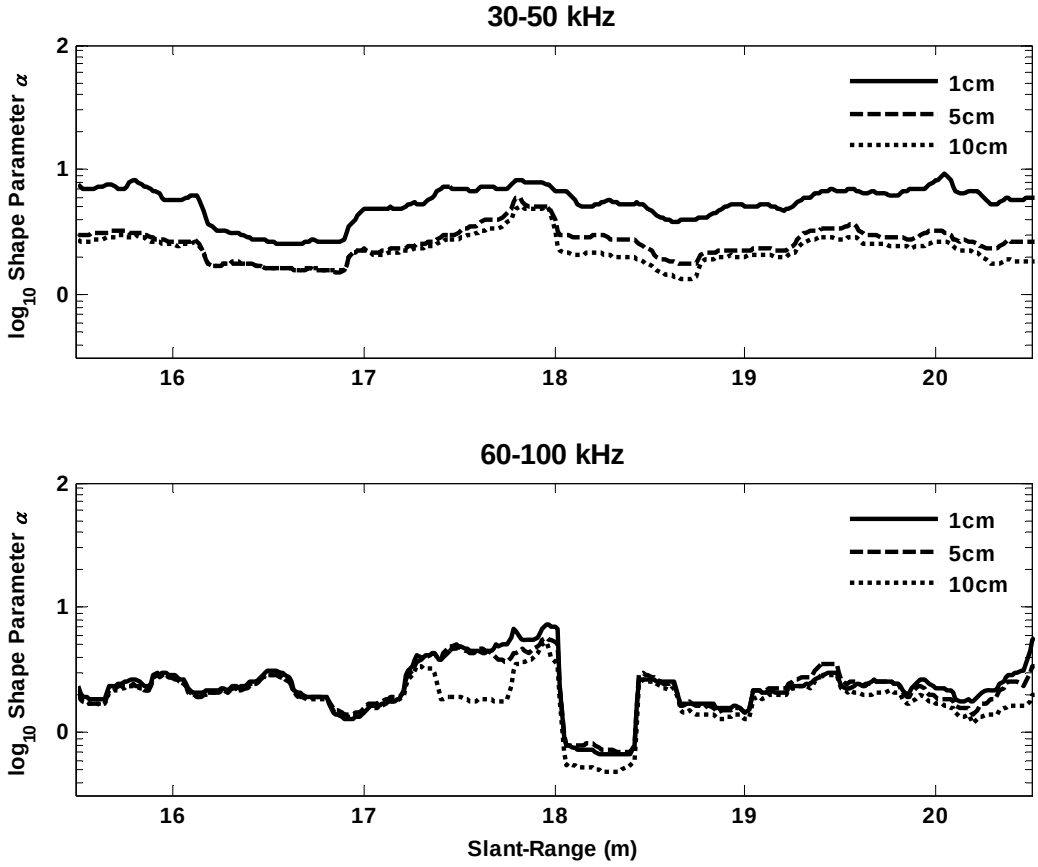

Figure 3.8: *K* distribution shape parameter estimates vs. slant-range for 30-50 kHz (top) and 60-100 kHz (bottom) images for each of the three vertical receiver apertures.

3.3.2 Modeling of Structure-Scattered Multipath

Figure 3.9 shows mean power level versus slant-range across synthetic aperture formed images for 30-50 kHz and 60-100 kHz data collected with 1 cm, 5 cm, and 10 cm vertical aperture receivers. Each curve is normalized so that the slope, excluding the fathometer-like multipath return, intercepts 0 dB at 17.9 m range. As individual scattering contributions from the rail and mobile-tower structure can not be resolved at fathometer-like ranges (*i.e.* the multiple returns between C & D shown in Figure 3.4 can

not be resolved in Figure 3.9), modeling of the multipath contamination is based on a single observable power level increase. This also serves to minimize the number of terms in each of the two-component reverberation models (*i.e.* only P_{DP} and a single P_{MPn} term remain in Equations 3.1 and 3.2). The increase in peak power level caused by multipath contamination (Table 3.1 third column) is then used as input to the two-component reverberation models of Section 3.2 and compared to the analysis of experimental data of Figure 3.8. It should be noted that although analysis for this section is restricted to an observable power level increase, any multipath mixing with the direct-path can impact the statistics even if there is no marked power level increase as demonstrated in Figure 3.2.

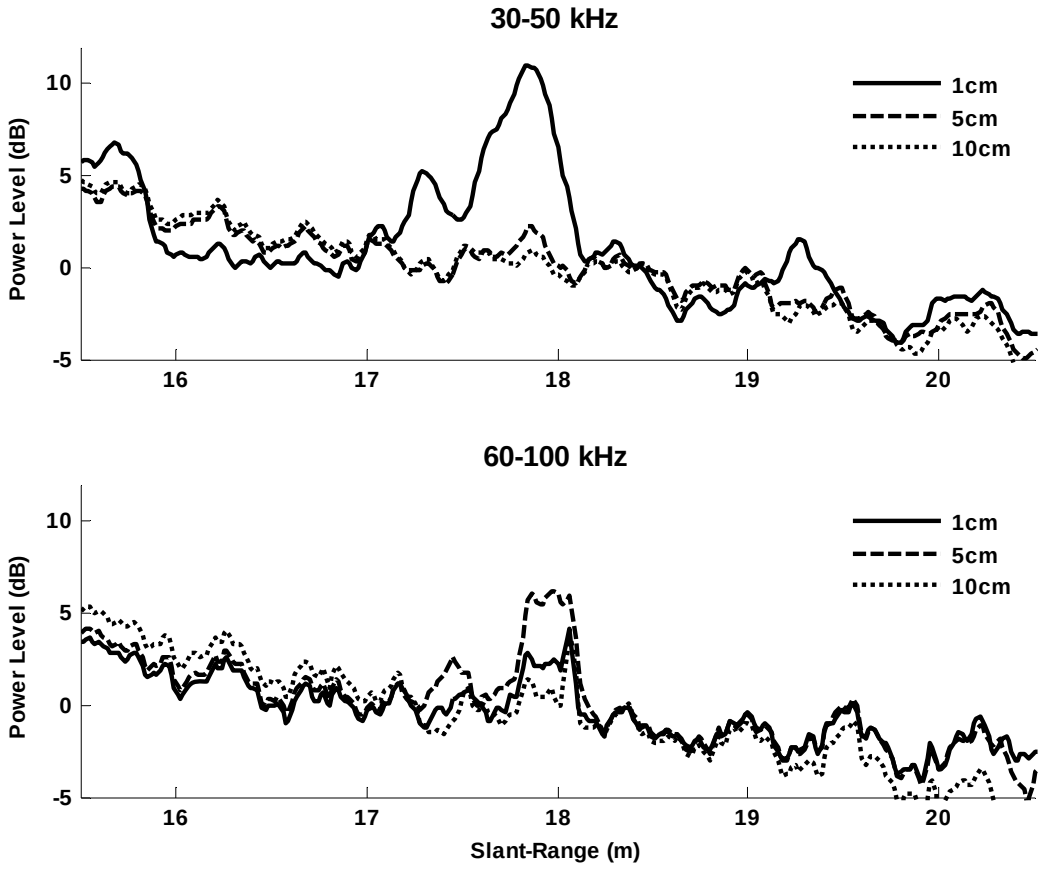

Figure 3.9: Power levels vs. slant-range for 30-50 kHz (top) and 60-100 kHz (bottom) images for each of the three vertical receiver apertures. Each curve is normalized so slope intercepts 0 dB at 17.9 m range.

Table 3.1: Comparison of structural multipath experimental analyses to model predictions.

			Experimental			**Model**	
Frequency (kHz)	Receiver (cm)	Δ Power Level (dB)	α_0 (@ 16.9 m)	Peak α	Δ α	Δ α Case 1 (K + Ray)	Δ α Case 2 (K + K)
30-50	1 cm	10.9	2.7	8.3	5.6	54.9	4.1
30-50	5 cm	2.2	1.5	6.0	4.5	7.9	3.0
30-50	10 cm	0.9	1.5	5.1	3.6	6.7	3.0
60-100	1 cm	6.2	1.3	7.3	6.0	12.0	2.3
60-100	5 cm	4.1	1.4	5.6	4.2	9.5	2.7
60-100	10 cm	3.8	1.3	5.3	4.0	8.4	2.5

The initial shape parameter input (α_0) used for the models is taken at 16.9 m range from the estimated K distribution shape parameter analysis of Figure 3.8. This region is generally free of multipath contamination for the majority of the images, and has seafloor structure visually similar to that surrounding the 17.9 m multipath. An exception is the 1 cm vertical aperture 30-50 kHz data which shows an observable statistical departure from the other data presented, the result of a nearly omni-directional receive beampattern placing additional emphasis on the vertically arriving multipath contaminants in this region of the analysis. It should be noted that this departure does not invalidate the analysis presented here since we are comparing the change in shape parameter as a function of the change in power level. Variability of the experimental data in this region highlights the amount of care that must be taken with this sort of analysis. These two

parameters (α_0 @ 16.9 m and Δ Power Level @ 17.9 m) then serve as inputs for the two-component reverberation models presented previously in Section 3.2.

It should be noted that in each example presented in Table 3.1, there was an increase in the *K* distribution shape parameter by a factor of at least 3. Recalling Figure 1.5, increasing the shape parameter has the effect of significantly reducing the tails of the envelope probability density, possibly by an order of magnitude or more for high amplitudes. This reduction of the tails in turn reduces the False Alarm rate, but is offset by a decrease in the probability of object detection because of an increase in reverberation power level, both attributable to multipath contamination.

For each of the six synthetic aperture formed images of varying bands and vertical receiver apertures presented, the two proposed cases of mixing a *K*-distributed direct path of shape parameter α_0 with either a *K*-distributed multipath of shape parameter α_0 or Rayleigh-distributed multipath bound the observed increase in shape parameter of the experimental data. Individually however, the results are not intuitive based on beampatterns alone, which one might consider to dominate these results (sea-floor backscattering strength is minimally dependent upon center frequency at 40 versus 80 kHz [Lyons & Abraham 1999, Johnson *et al*. 2005, Jackson 2007], particularly when compared to more drastic changes in beampattern). Thus, one is forced to also consider the frequency dependent nature of the rail and mobile-tower structural scattering, thus lending additional validity to the assumption that the predominant scattering mechanism

in this situation is not seafloor induced, but rather structurally induced multipath contamination.

3.4 Environmental Multipath

As the majority of SAS systems are either towed or AUV based, it is of greater interest to investigate environmental multipath which not only degrades the image but may limit the ability of the processing to make needed motion compensations to produce a clear image. We begin with an example of how environmental multipath impacts both the imagery and statistics of Synthetic Aperture Sonar, followed by a method for modeling and simulation of multipath based on system and environmental parameters.

3.4.1 Analysis of SSAM Data

Figures 3.10 and 3.11 show example high frequency (HF) and low frequency (LF) band images (top) from data collected concurrently with the AUV based SSAM, and corresponding *K* distribution shape parameter versus range (bottom), estimated using the processing steps described in the previous section. In this example, the tighter beampattern of the high-frequency (HF) band allows for significantly greater rejection of multipath as compared to the low-frequency (LF) band. In the LF band image, the onset of the surface arrival is visible about 25 m range with a slight increase in shape parameter, and fathometer-like multipath at 29 m range causing a significant increase with the distinct imagery of rippled sand becoming blurred. For the LF band image, the

mean K distribution shape parameter increases a negligible amount from $\alpha_{mean} = 1.1$ for 15-29 m to $\alpha_{mean} = 1.3$ for 29-40 m, well within the variance of the estimates (Figure 3.10 bottom). However, the HF band image shows a significant increase from $\alpha_{mean} = 3.2$ for 15-29 m to $\alpha_{mean} = 17.2$ for 29-40 m, representing a significant trend towards Rayleigh-like statistics because of multipath contamination (Figure 3.11). In both analyses, the estimation window included all along-track data shown, with a slant-range extent of 0.72 m (30 samples for HF band image, 60 samples for LF). Environmental multipath continues to persist beyond the onset range as the boundaries supporting the multipath are the sea-floor and sea-surface, not finite sized structural elements as in the previous section.

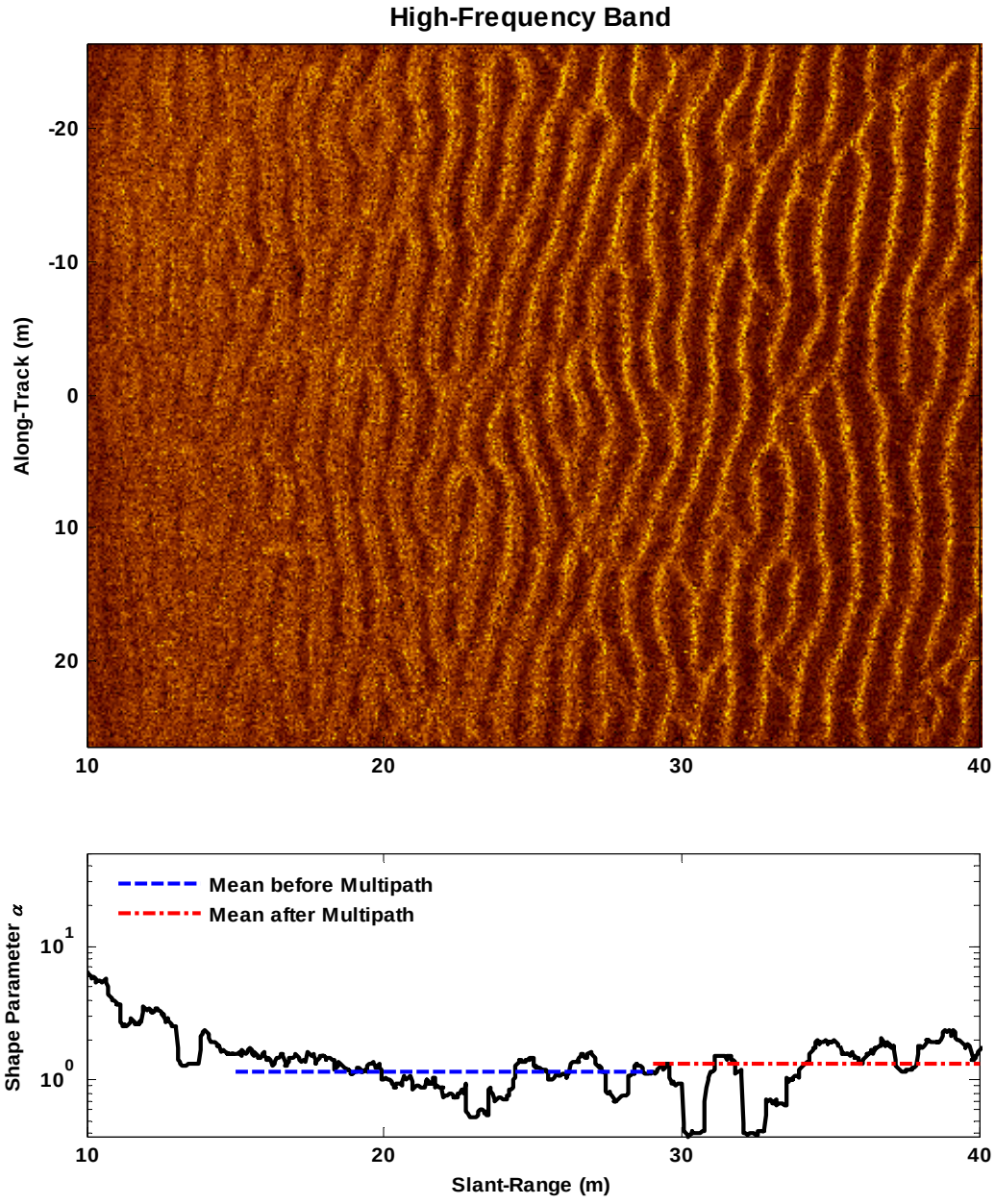

Figure 3.10: HF band SSAM image (top) and *K* distribution shape parameter estimates (bottom) vs. slant-range.

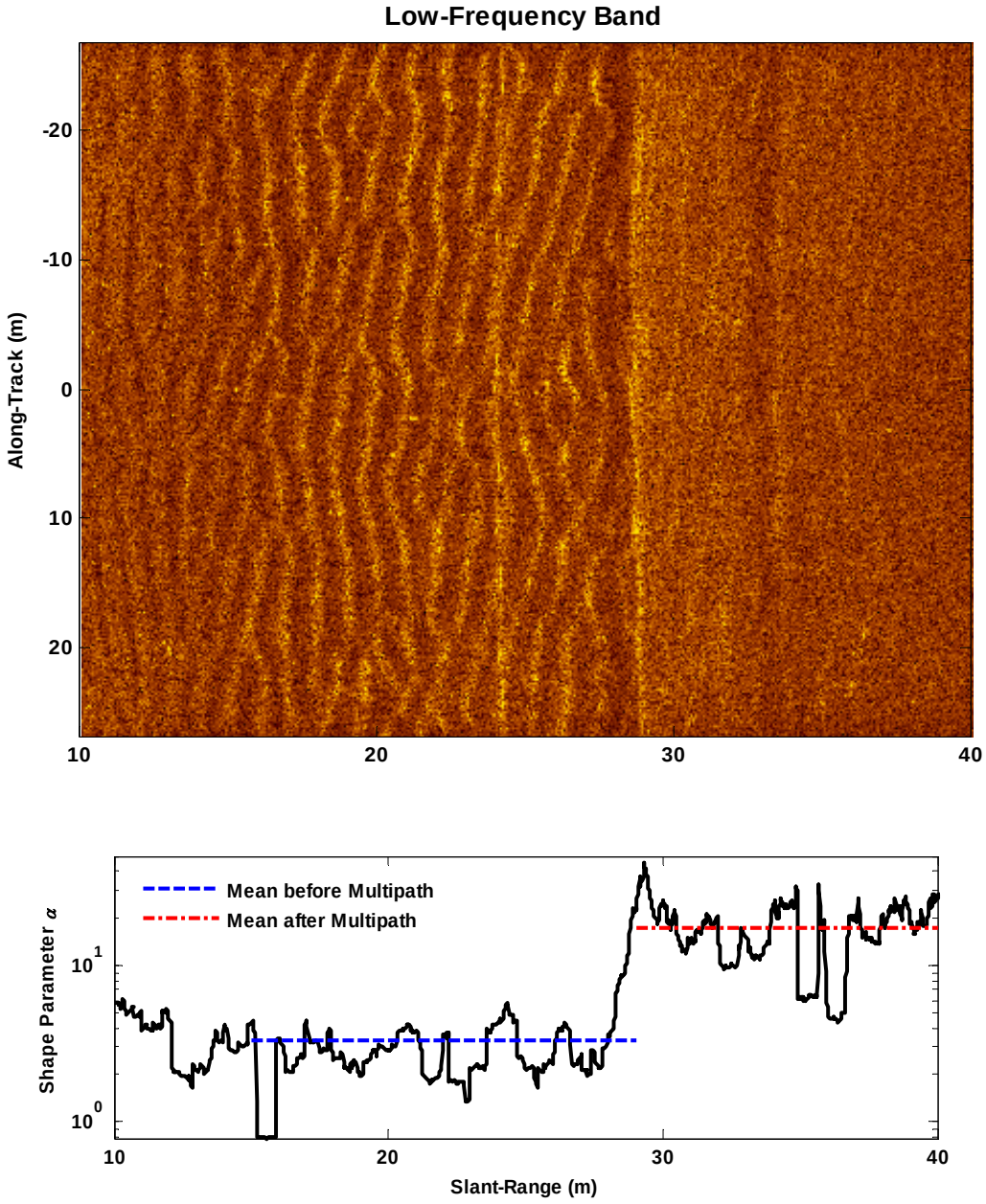

Figure 3.11: LF band SSAM image (top) and K distribution shape parameter estimates (bottom) vs. slant-range.

3.4.2 Modeling and Simulation of Environmental Multipath

As seen in Section 3.3.2, good agreement can be achieved between observed and predicted impact of multipath on image statistics utilizing observed power level increases and moment-matched analytical equations. In an effort to predict the potential impact of multipath *in silico*, these methods are extended to model environmental multipath. The first step is to calculate the range-dependent power levels for the direct-path and contributing multipaths. These levels can then be input to the moment-matched equations as before, or can be used in numerical simulation involving random variates or more complicated simulations of coherent synthetic aperture images as presented in the previous chapter.

3.4.2.1 Modeling Range-Dependent Path Power Levels

The power levels of the multipath and direct-path contributions to reverberation are derived from the transmit- and receive-array beampatterns and the backscattering strength of the sea surface and/or seafloor at near-normal incidence. For simplicity, these are both modeled using the center frequency of the transmitted signal. Both the backscattering strength and beampatterns change minimally over bandwidth of the transmitted signal [Jackson 2007, Abraham & Johnson 2008]. For the examples here, simulation follows a similar setup as the SAX04 experiment, with specific values given in Tables 2.1 and 3.2.

Table 3.2: Parameters used in environmental multipath simulation

Property	Value
Transmit Vertical Aperture	0.01 m
Transmit Horizontal Aperture	0.10 m
Receive Vertical Aperture	0.01 m and 0.05 m
Receive Horizontal Aperture	0.10 m
Sonar Center Frequency	80 kHz
Sonar Bandwidth	40 kHz
Sonar Aiming Angle (grazing)	10°
Sonar Height (above sea-floor)	5.0 m
Water Depth	25.0 m
Sound Speed in Water	1535 m/s
Along-Track Resolution	0.025 m
Slant-Range Resolution	0.050 m

The transmit and receive beam patterns are calculated using the standard text-book line array as found in [Lurton 2004], modified by an additional $\cos^2\theta$ term to suppress rearward facing lobes and more closely match beam patterns of the transducers as measured in a calibration tank. The vertical and horizontal transmit and receive beam patterns are then combined, taking into account the Sonar aiming angle. Figures 3.12 and 3.13 show example beampatterns taken as slices through the *x*-*y* plane at the Sonar height parallel to the seafloor for the direct path, surface reflection, and bottom and surface arriving multipath for the 5 cm and 1 cm vertical aperture receiver respectively. These

two-way beampatterns depicted in Figure 3.12 and 3.13 are then projected onto the seafloor or sea surface taking into account the corresponding method of images heights as in Figure 3.1 and two-way spherical spreading. Travel time is calculated for each point on the computation surfaces and amplitudes are summed within a window of bandwidth^{-1} which corresponds to the radial resolution of Sonar before synthetic aperture formation. This level is then combined with a projection of the modeled seafloor backscattering strength as a function of range as in Table 2.1 and Figure 2.19 and/or a Lambertian term of $\cos^2\theta$ for sea surface scattering depending on the interactions of the path considered. Figure 3.14 shows the resulting range-dependent path power levels for the two receiver vertical apertures and four paths considered. Recalling Figure 3.2, an impact on the statistics should be expected when multipath come within -10 dB or more of the direct-path. Figure 3.15 demonstrates this using the moment-matched Equations 3.1 and 3.2 (note the top plot ordinate axis is $\log_{10}$ while the bottom is linear, and shape parameter estimates have been scaled by the estimate before the onset of multipath). For both Rayleigh- and *K*-distributed multipath cases, the 5 cm vertical aperture is minimally affected by the multipath with a slight increase when the surface arrival comes within -10 dB. For the case of Rayleigh-distributed multipath with the 1 cm receiver, the onset of the surface arrival drives the statistics towards Rayleigh immediately because its power level is greater than the direct path. For the case of the *K*-distributed multipath with the 1 cm receiver, the shape parameter displays a sudden increase and then drops with increased range. This is again because the surface reflection level dominates the direct path which in turn drives the statistics. The moment-matched Equation 3.1 assumes both paths are of the same *K* distribution shape parameter so that the result returns to the

original value of one. It should be noted, however, that an actual image would be dominated by the surface reflection and not the intended seafloor as will be demonstrated in the next section.

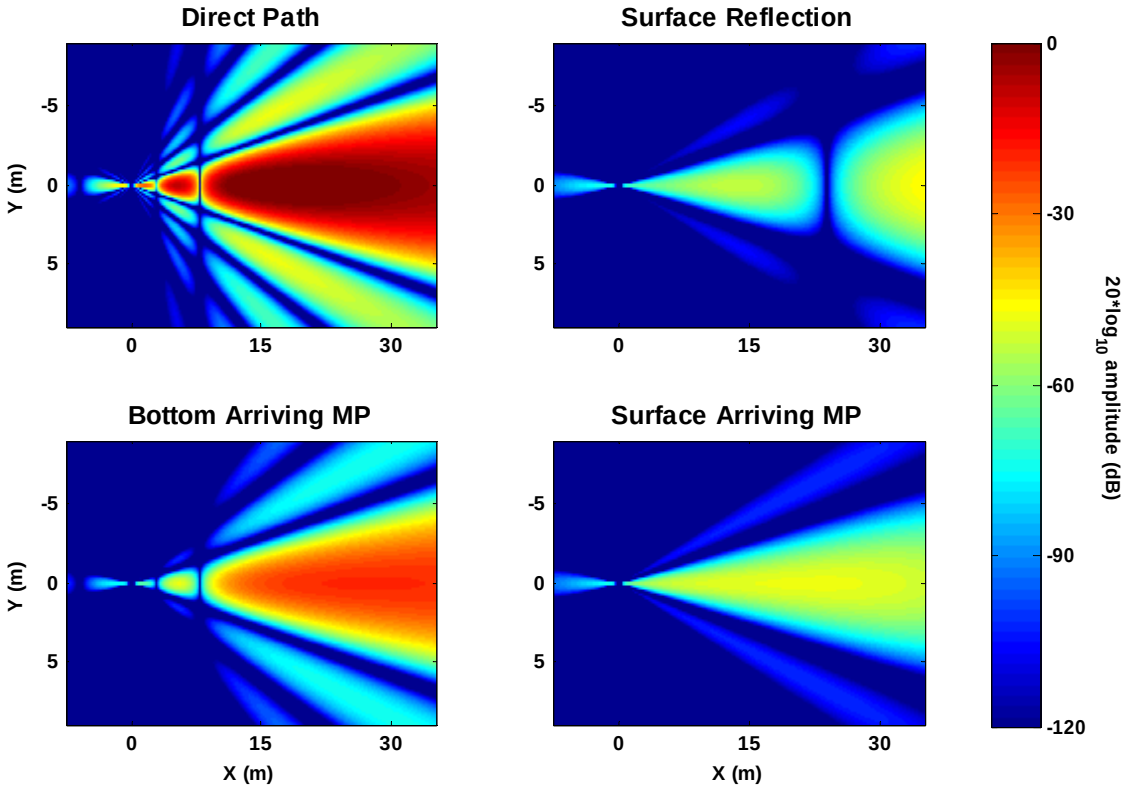

Figure 3.12: Modeled two-dimensional beampatterns for direct-path and multipaths with transducers of vertical apertures 1 cm (transmit) and 5 cm (receive) at 80 kHz.

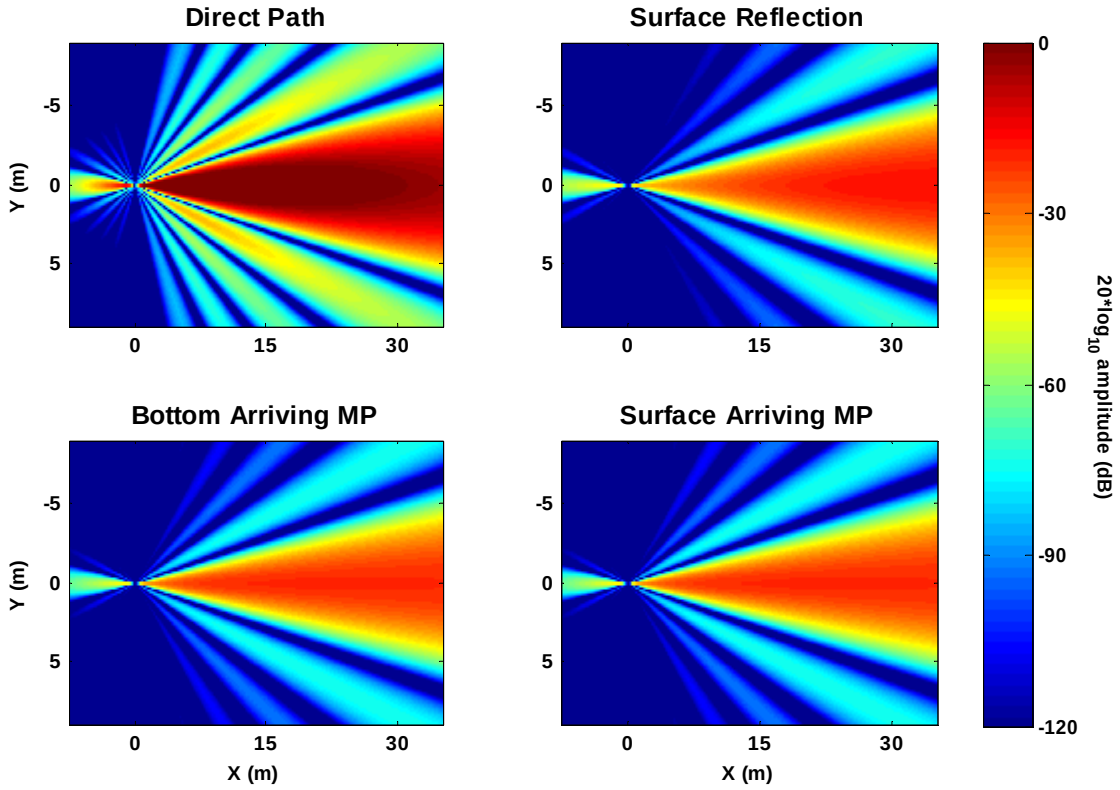

Figure 3.13: Modeled two-dimensional beampatterns for direct-path and multipaths for transducers of vertical apertures 1 cm (transmit) with 1 cm (receive) at 80 kHz.

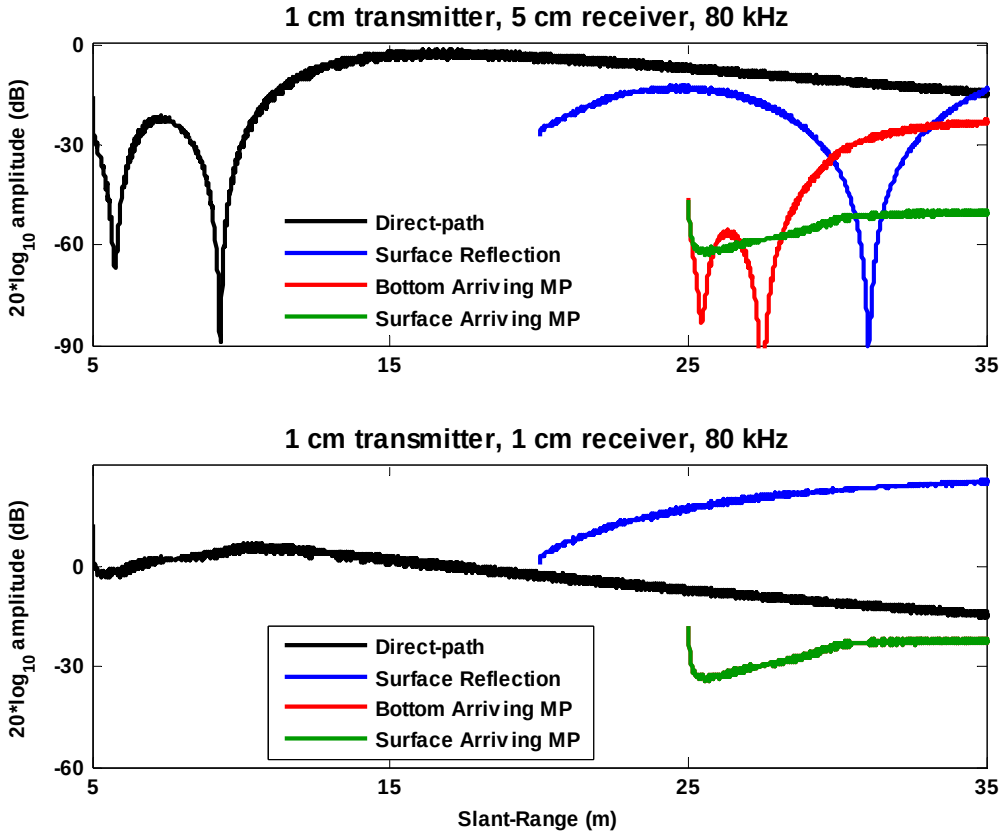

Figure 3.14: Direct-path and multipath power levels vs. slant-range for 1 cm transmitter with 5 cm receiver (top), and 1 cm receiver (bottom) at 80 kHz.

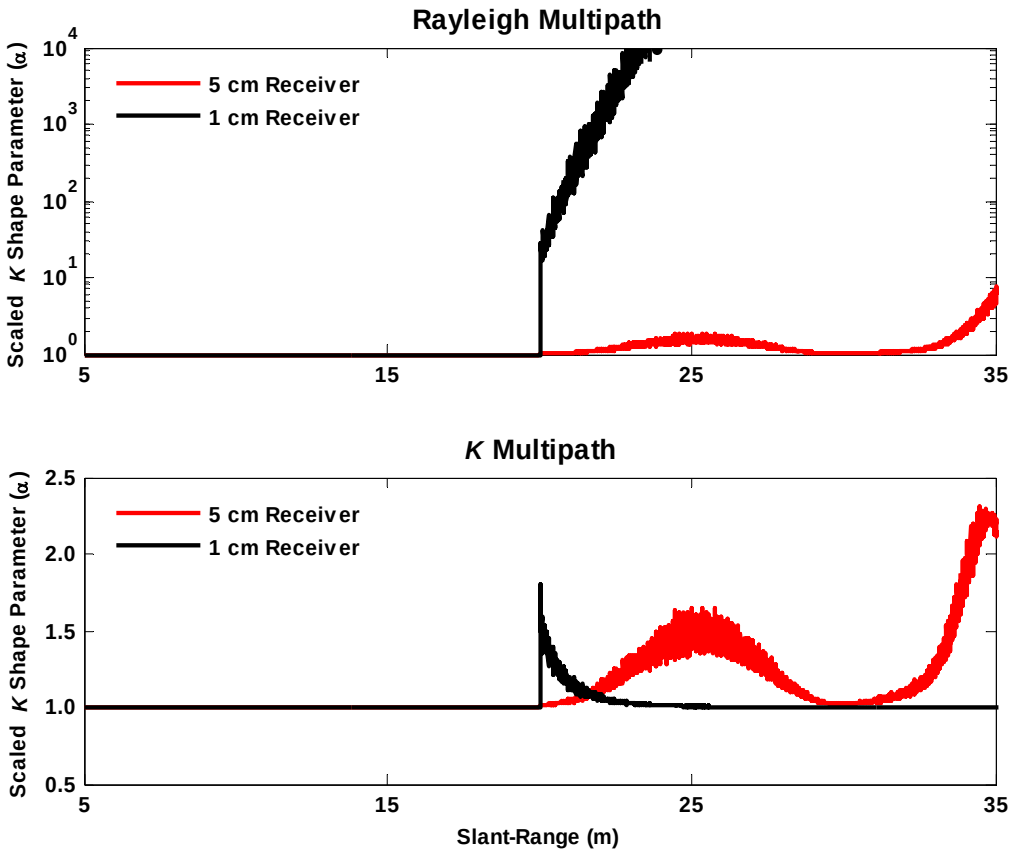

Figure 3.15: Shape parameter vs. slant-range using moment-matched equations with modeled range-dependent path power levels for 1 cm (black) and 5 cm (red) receivers with Rayleigh multi-path (top) and *K* multi-path (bottom). Note the ordinate axis is $\log_{10}$ (top), and linear (bottom).

3.4.2.2 Simulation of Multipath Impact with Random Variates

Utilizing the range-dependent path power levels calculated in the previous section and the random variate generation techniques of Section 2.4.1, the impact of multipath on image statistics can be predicted numerically. For this and the following section, only Rayleigh-distributed multipath will be considered, with justification being two-fold: the

observed increase in the *K* distribution shape parameter (Figure 3.11) is significantly greater than predicted by a low shape parameter *K*-distributed multipath, and sea surface motion between pings will distort any coherence of source images involving a sea surface interaction, thus rending these source images as purely random noise. Figure 3.16 shows estimated shape parameter versus range for mixing of random variates (*K*-distributed direct path of $\alpha = 1$ and Rayleigh-distributed multipaths) using the method of moments estimator described in Section 2.3.3. As in Figure 3.15 (top), the 5 cm vertical aperture receiver case is minimally affected by multipath, while for the 1 cm receiver case the shape parameter increases with the onset of multipath. A distinct advantage of random variate mixing compared to the acoustic image simulation discussed in the next section is the speed of computation. Any of a number of distributions of varying statistics and power levels representing direct-path and multipaths can be combined with subsequent estimation of statistical parameters once a set of range-dependent path power levels are computed. However, while this is advantageous for system performance prediction, the resulting images bear little resemblance to actual Sonar displays despite being statistically accurate because of a lack of correlation between pixels observed in images caused by seafloor structure (*e.g.*, sand ripples).

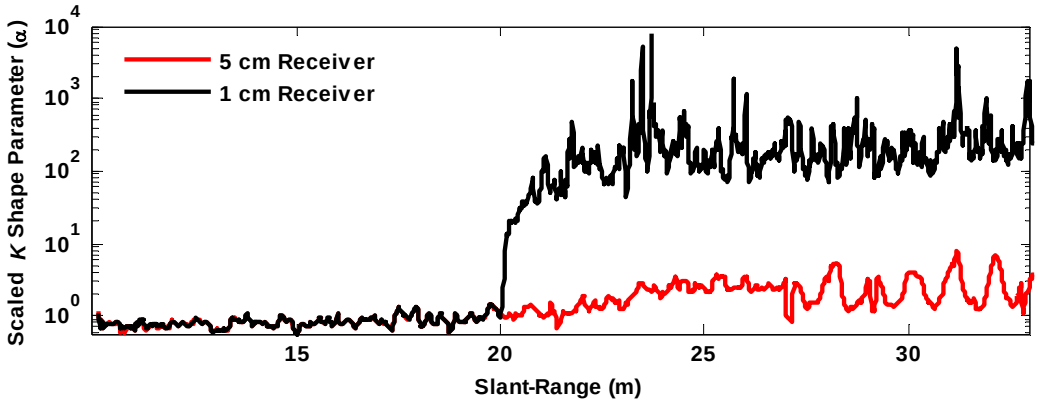

Figure 3.16: Shape parameter vs. slant-range using simulated range-dependent path power levels for 1 cm (black) and 5 cm (red) receivers by mixing *K* direct path and Rayleigh multi-path random variates.

3.4.2.3 Simulation of Multipath Impact with Simulated Acoustic Images

Utilizing the range-dependent path power levels calculated in Section 3.4.2.1 and the random variate generation techniques of Section 2.4.1 for the multipath, combined with the rippled-sand acoustic simulation of Section 2.4.2 for the direct-path, a more realistic Sonar image can be simulated. Figure 3.17 shows an example image (top) and corresponding shape parameter estimates with range (bottom) as simulated with methods of the previous chapter. This image is mixed with Rayleigh-distributed random variates using the range-dependent path power levels modeled previously and shape parameter versus range is then estimated (Figure 3.18). For this example, the 5 cm aperture produces an image that is both visually (top) and statistically (bottom) free of multipath, while the 1 cm aperture receiver image is dominated by multipath after the surface arrival

at 20 m slant-range with Rayleigh-like appearance and statistics. This example is in good agreement with the environmentally-induced multipath observed in experimental data.

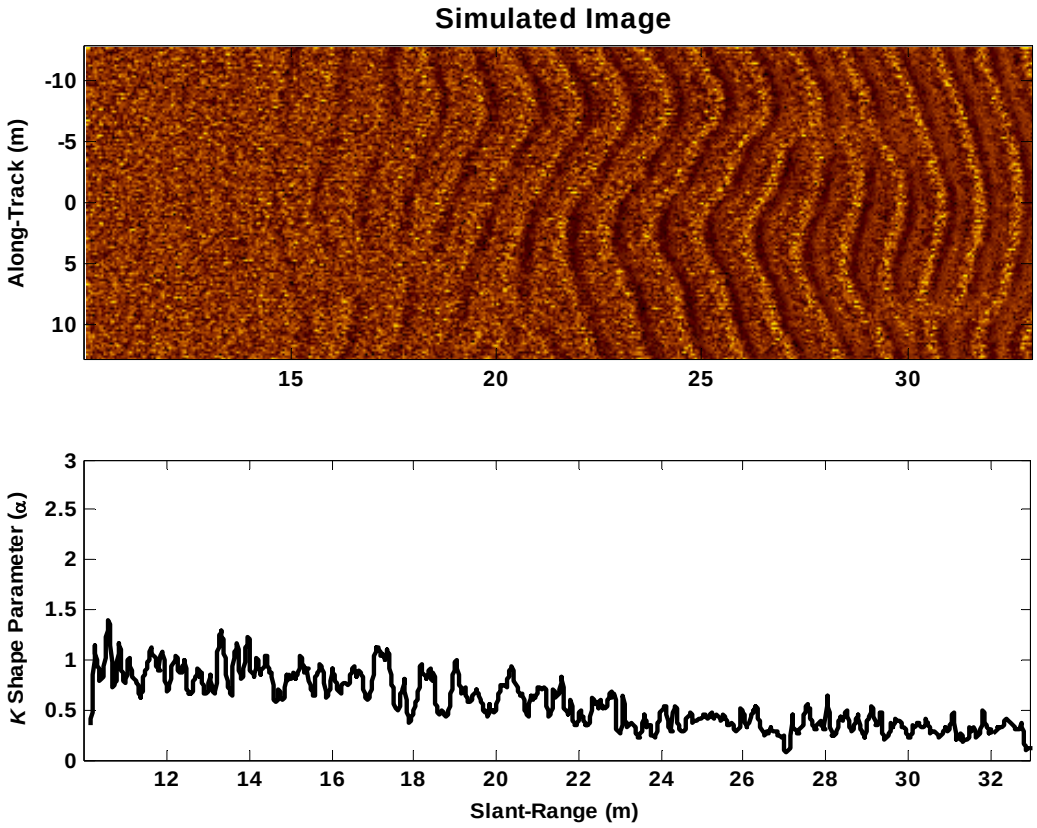

Figure 3.17: Simulated SAS image (top) and estimated *K* shape parameter as a function of slant-range (bottom).

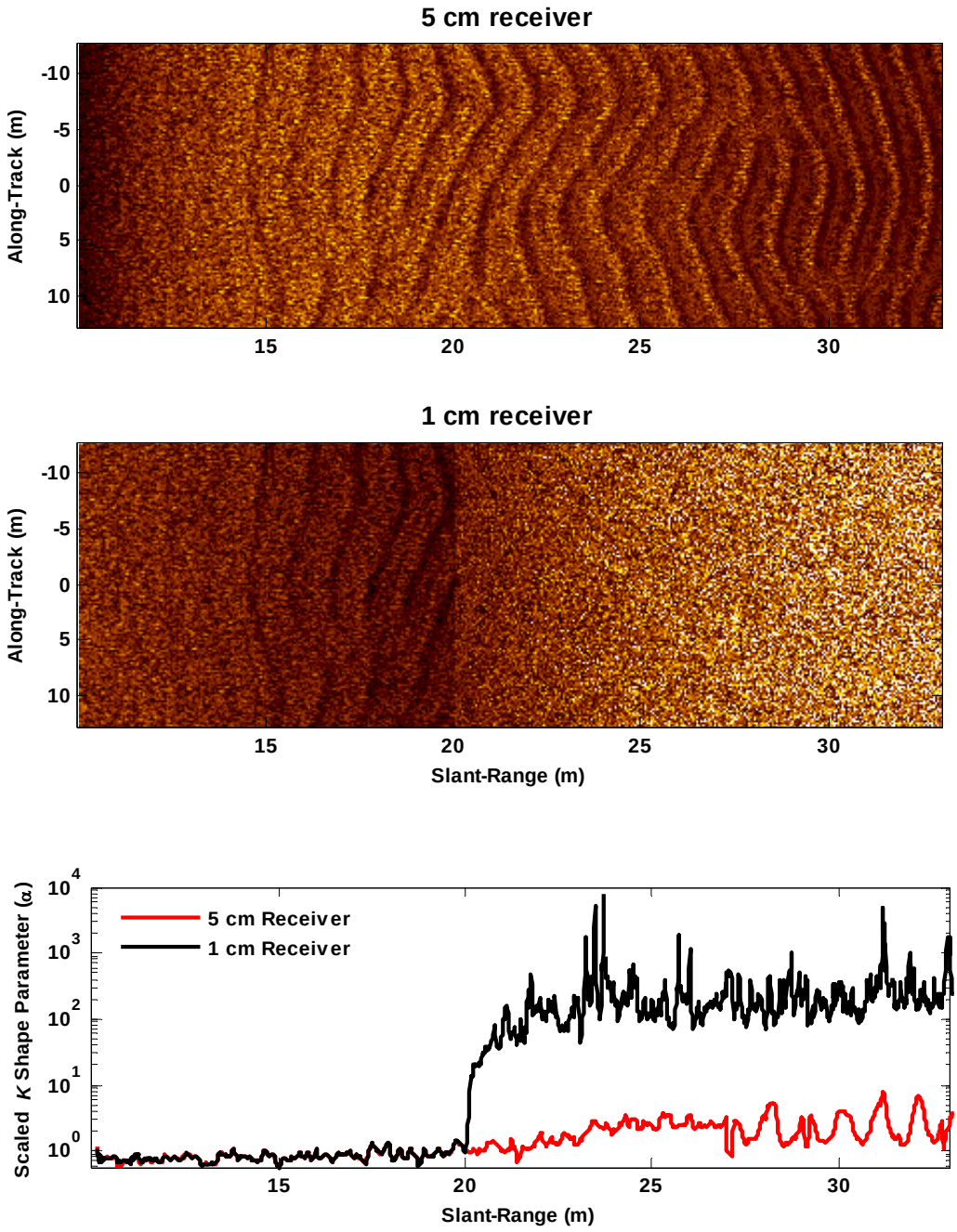

Figure 3.18: Simulated SAS images using simulated image mixed with Rayleigh variates for 5 cm receiver (top) and 1 cm receiver (middle). Equivalent shape parameter results (bottom) for 1 cm (black) and 5 cm (red) receivers.

Chapter 4

Impact of Resolution on SAS Image Statistics

4.1 Chapter Introduction

Synthetic Aperture Sonar systems are capable of producing images which resolve regions of the seafloor on the order of square centimeters. Such high-resolution images may only contain a few dominant scattering features per pixel, often resulting in images with wide inter-pixel amplitude fluctuations and heavy-tailed envelope probability distributions. It is possible through post-processing to increase the resolution cell area, potentially reducing the tails of the envelope distribution in certain scenarios. Extensions of former work with one-dimensional resolution reduction [Abraham & Lyons 2002a, Abraham & Lyons 2002b, Preston & Abraham 2004, Abraham & Lyons 2004a, Johnson *et al*. 2005, Lyons *et al*. 2005, Abraham & Johnson 2008, Lyons *et al*. 2009] to two dimensions simultaneously will be introduced. Results have shown that when scatterers are not over-resolved, a doubling of the resolution cell area corresponds to a doubling of the estimated K distribution shape parameter because of a doubling of the number of ensonified scatterers or scattering patches. However, just as with the previous analysis of multipath data, these studies are somewhat limited by the range-dependent resolution nature of traditional aperture Sonar (*i.e.* either monostatic or traditional line arrays). Additionally, previous work focusing on resolution reduction in one dimension was

limited by integer-only reductions of the original transmit bandwidth or by an integer-only number of elements used for beamforming. Synthetic aperture data utilizing the techniques presented in this chapter provide a unique opportunity for statistical analysis of any resolution desired in two dimensions, increasing understanding of the interplay between Sonar resolution and the seafloor properties impacting image statistics. Methods are presented first, followed by utilization of these techniques with experimental data and numerical simulation. Examples include scenarios when reverberation from a correlated seafloor may continue to be significantly non-Rayleigh in spite of resolution degradation.

4.2 Wavenumber Domain Sub-Banding

4.2.1 Multilook Synthetic Aperture Processing

As alluded to in discussion of Equation 1.13, approximations made with respect to the along-track sampling interval in synthetic aperture beamforming algorithms using digital (*i.e.* discretely sampled) systems may lead to aliasing of energy from along-track side-lobes into the main-lobe of the formed beam. It is possible to reduce the impact of these grating-lobes by increasing the along-track sampling rate. An alternative is to reduce the effective bandwidth. From Equation 1.11, one can see the along-track synthetic aperture resolution is proportional to the Doppler bandwidth and inversely proportional to the velocity of the physical aperture (where resolution is defined as $1/\Delta y_{SAS}$). If the platform velocity has a design minimum because of flight properties, or the pulse-repetition frequency is limited because of propagation speed, grating-lobes may

be inevitable with traditional processing (*i.e.* utilizing Equation 1.11). Minimum platform speeds are required for many airborne Synthetic Aperture Radar systems to maintain orbit while imaging at long ranges (*i.e.* from outer-space for the case of a non-geosynchronous satellite). Multilook processing was introduced to mitigate these constraints. A more recent and widespread usage of multilook is in the reduction of coherent image speckle [Curlander & McDonough 1991, Fortune *et al*. 2003, Cumming & Wong 2005].

The principle of multilook is to divide the along-track Doppler bandwidth (BW_D) into multiple sub-bands to produce multiple images of lower resolution with improved grating-lobe characteristics. Reducing BW_D increases the required sample spacing to effectively reduce grating-lobes. Substituting Equation 1.4 into Equation 1.10, we have:

$$BW_D \approx \frac{2v_p}{a_{wy}\lambda}\theta_{y\,3dB} = \frac{2v_p f}{a_{wy} c}\theta_{y\,3dB} \quad \text{Equation 4.1}$$

For a fixed platform velocity, carrier frequency, and wavelength, reducing BW_D increases the angular main-lobe width proportionally. Again recalling Equation 1.11, reducing the BW_D reduces the along-track resolution proportionately (*i.e.* one-half BW_D increases $\Delta y_{SAS\ 3dB}$ by a factor of two). This can be implemented either during the beamforming process itself, or through post-processing formed complex images (*i.e.* images that retain the amplitude and phase information of the original formation process). A common procedure is to create two images or 'looks' from a single set of beamformed data, each

having one-half the along-track resolution. As each image is formed from independent portions of the Doppler bandwidth, they can be considered independent realizations of the same scene, and speckle between the images is uncorrelated. If the images are then combined incoherently (*i.e.* co-located pixel magnitudes are summed), the resulting image will have reduced speckle [Fortune *et al*. 2003]. This can be expanded to multiple Doppler sub-bands, even overlapping bandwidths 10-60% with appropriate windowing [Moreira 1990, Moreira 1991, Cumming & Wong 2005], keeping in mind the necessary bandwidth to achieve desirable along-track resolution. A caveat to this treatment will be presented in Section 4.2.3.

4.2.2 Adjusting Resolution in Two-Dimensions via. Post-Processing

Just as reducing the Doppler bandwidth reduces the along-track resolution, reducing the pulse bandwidth reduces the slant-range resolution. Recalling Equation 1.1, the slant-range resolution is directly proportional to the bandwidth of the transmitted pulse (*i.e.* one-half BW_{lfm} increases Δx_{slant} by a factor of two). A similar technique is employed in [Abraham & Lyons 2004a, Johnson *et al*. 2005, Lyons *et al*. 2009] using monostatic data. Resolution adjustment in two-dimensions simultaneously can be performed by limiting the bandwidths of the two-dimensional wavenumber domain, prior to performing the two-dimensional inverse Fourier transform into the spatial domain (*i.e.* the resulting synthetic aperture formed image).

This reduction can be applied to the either the Doppler or pulse bandwidth independently. From [Soumekh 1994], the two-dimensional Fourier transform pairs ($\Im, \Im^{-1}$) of signal $f(x,y)$ are given by:

$$\Im_{k_x,k_y}\left[f(x,y)\right] \equiv F(k_x,k_y) \equiv \int_{-\infty}^{\infty}\int_{-\infty}^{\infty} f(x,y)e^{-j(k_x x+k_y y)}\,dx\,dy \quad \text{Equation 4.2}$$

and

$$\Im^{-1}_{k_x,k_y}\left[F(k_x,k_y)\right] \equiv f(x,y) \equiv \frac{1}{(2\pi)^2}\int_{-\infty}^{\infty}\int_{-\infty}^{\infty} F(k_x,k_y)e^{j(k_x x+k_y y)}dk_x dk_y \,. \quad \text{Equation 4.3}$$

If the function $f(x,y)$ represents a separable two-dimensional signal, such that:

$$f(x,y) = f_1(x) f_2(y) \quad \text{Equation 4.4}$$

the two-dimensional Fourier transform of $f(x,y)$ is also a separable two-dimensional function given by:

$$F(k_x,k_y) = F_1(k_x) F_2(k_y) \quad \text{Equation 4.5}$$

The assumption that $f(x,y)$ represents a separable two-dimension signal is valid for synthetic aperture data because of the properties of the inverse Stolt map (Equations 1.16

and 1.17), with slant-range and along-track resolutions being independent (Equations 1.1 and 1.11). Images can be divided into *m* range sub-bands and *n* cross-range sub-bands, producing *m* times *n* images from independent wavenumber sub-bands, each having a spatial resolution of 1/*m* by 1/*n* of the original after inverse Fourier transform.

4.2.3 A Caution for Averaging Sub-Banded Images

As mentioned in Section 4.2.1, sub-banded images from independent regions of the spatial wavenumber domain are sometimes incoherently summed to reduce speckle. Similarly, images are sometimes pixel averaged or filtered spatially to reduce noise. If such images are implemented with an energy detector, there is often a decrease in the Probability of False Alarm, which is typically considered advantageous. Caution should be exercised, however, to maintain a suitable Probability of Detection. As an example, a synthetic aperture image from the SAX04 experiment dataset (Figure 4.1) and corresponding two-dimensional wavenumber spectrum (Figure 4.2). When the spectrum is divided into three slant-range sub-bands and three cross-range sub-bands, nine independent images can be produced. Figure 4.3 shows four of these nine images from the corresponding four corner regions of Figure 4.2, with Figure 4.4 showing detail of areas including a flush-buried sphere.

Figure 4.5 is the incoherent summation of all nine sub-banded images as would be performed in multilook processing. Table 4.1 summarizes a disadvantage with multilook in this particular case: the backscattered signal from the sphere to mean background level

(SBL) of the original image is 47.3 dB and is reduced over 9 dB by multilook processing to 37.7 dB. While the summation of the multilook images decreases the Probability of False Alarm, in this case multilook could decrease the Probability of Detection by lowering the SBL. From Table 4.1 and Figure 4.4, it is seen that the sphere has a higher level compared to the mean background level in the lower slant-range spatial frequency (k_x) images compared to the higher slant-range spatial frequency images, which is defined by the transmit frequency. Despite the sphere itself being axially-symmetric, there is a slight advantage to the middle k_y spatial frequency images, or region about the Doppler centroid, which is most likely because of the horizontal beampattern of the transmit / receive transducers and windowing to control side-lobes. It is hypothesized that an object that does not exhibit angular symmetry would appear different in the various Doppler bandwidth-limited images. Considering this, *a priori* understanding of the acoustic properties of a desired object would aid in decreasing the Probability of False Alarm while minimally impacting the Probability of Detection, however this requires additional consideration and experimentation.

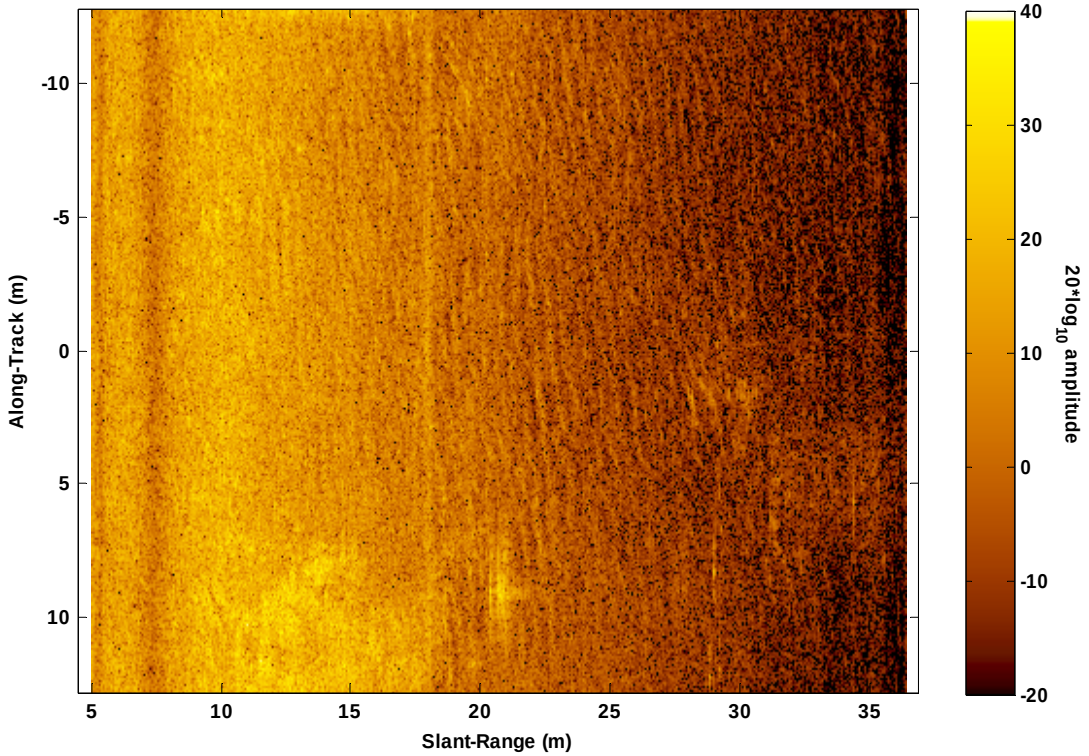

Figure 4.1: SAS image with flush-buried sphere at 9.8 m slant-range and -5.2 m along-track.

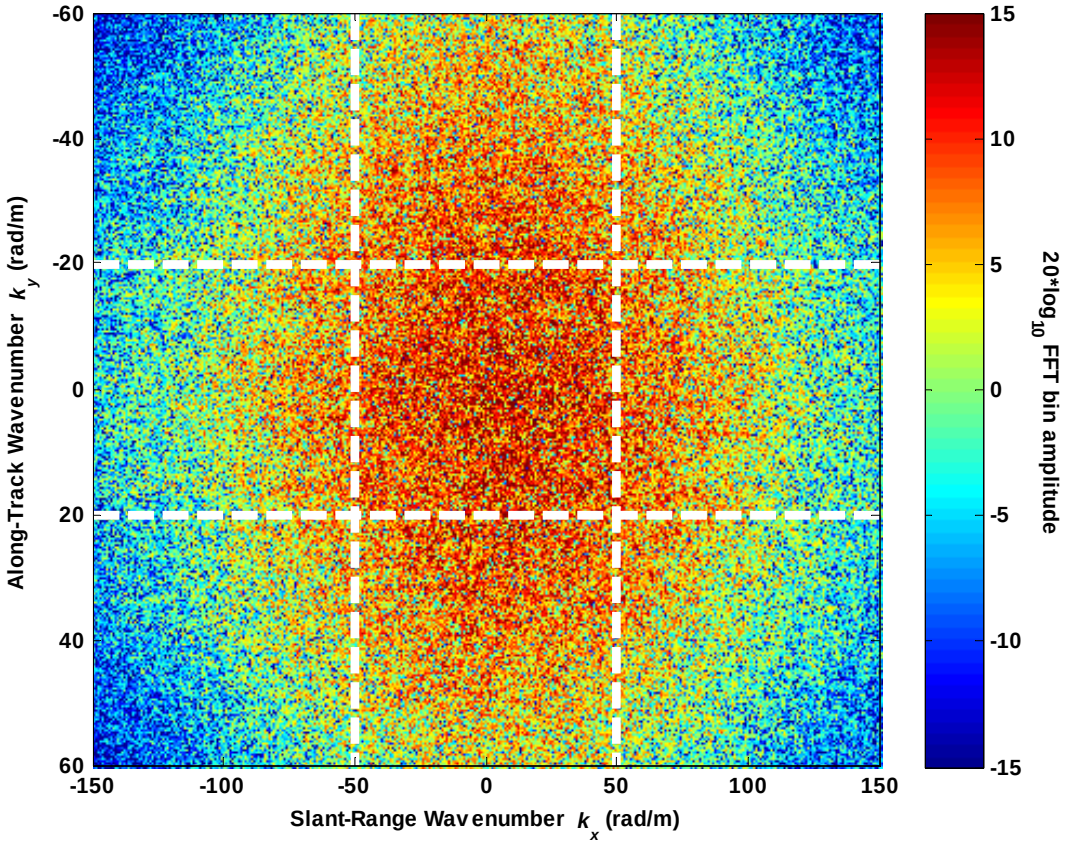

Figure 4.2: Two-dimensional spatial wavenumber spectrum of Figure 4.1.

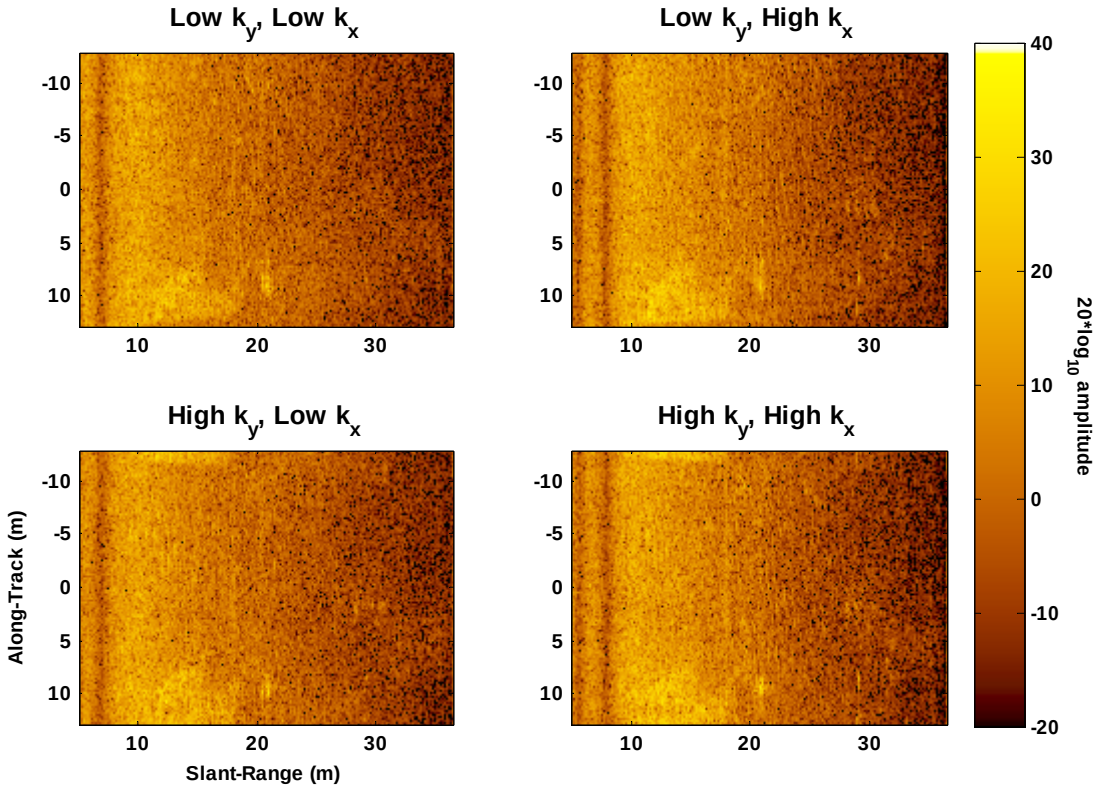

Figure 4.3: Images produced from four corner regions of the spatial wavenumber spectrum of Figure 4.2.

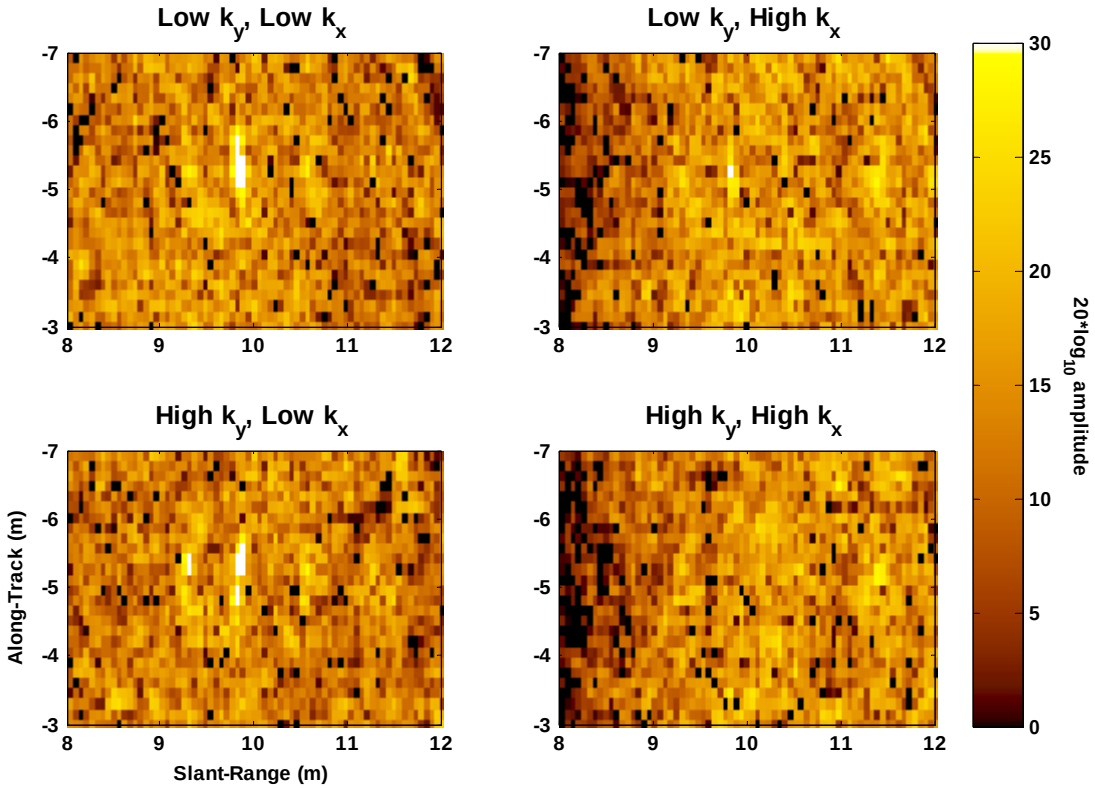

Figure 4.4: Same as Figure 4.3, zoomed to show detail of flush-buried sphere.

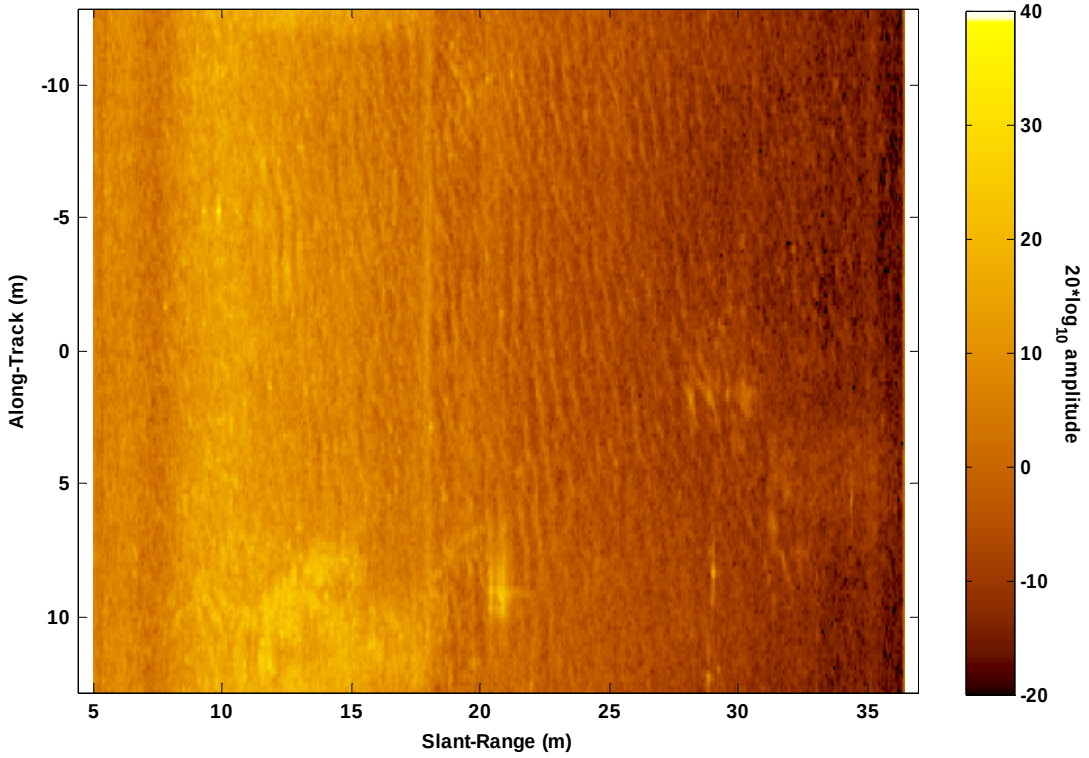

Figure 4.5: Example 9-look version of figure 4.1.

Table 4.1: Comparison of object levels in multi-look images. Low k_x,k_y top left, high k_x,k_y bottom right for individual sub-bands, as in previous figures.

Original Image SBL	**Individual Sub-Banded Images SBL**				**Multilook SBL**
47.3 dB		k_x			37.7 dB
	k_y	44.9 dB	38.5 dB	30.9 dB	
		46.9 dB	39.3 dB	29.1 dB	
		40.7 dB	34.6 dB	20.4 dB	

4.3 Data Analysis

Figure 4.7 shows K distribution shape parameter estimates for resolution reduction of an SSAM image of sand ripples parallel to the along-track dimension (Figure 4.6) along a single dimension. Shape parameter estimates made from images that were resolution reduced in the range dimension only (*i.e.* limiting the pulse bandwidth) are shown as blue circles, and resolution reduced in the cross-range dimension only (*i.e.* limiting the Doppler bandwidth) as red diamonds. Also shown is the slope of the anticipated doubling of shape parameter for doubling of area [Abraham & Lyons 2002b] based on the shape parameter estimates of the original image.

The apparent discrepancy can be explained by considering the visual appearance of example resolution reduced images. Figure 4.8 shows two representations of Figure 4.6 using $1/10^{th}$ of the original image bandwidth. The top image was created using $1/10^{th}$ of the available bandwidth in the range dimension, (*i.e.* $1/10^{th}$ BW_{lfm}); the bottom image using $1/10^{th}$ of the available bandwidth in the cross-range dimension (*i.e.* $1/10^{th}$ BW_D). As a result of the orientation of the sand ripples in this example, the two images appear significantly different. While the area of each pixel is identical, the dimensions of the pixels are not (*i.e.* $10\times\Delta x_0$ by Δy_0 for the top image, and Δx_0 by $10\times\Delta y_0$ for the bottom image, with the original image having a resolution of Δx_0 by Δy_0). Therefore, image statistics depend not only on the resolution, but also on the orientation of the aperture to the seafloor.

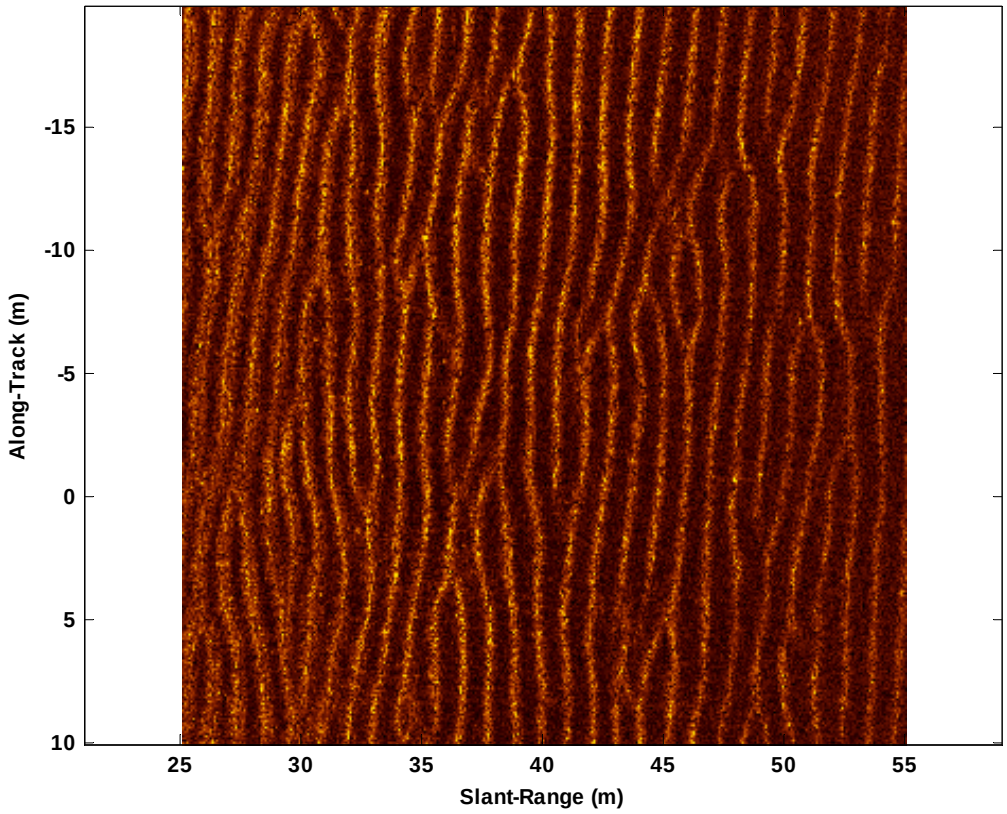

Figure 4.6: SSAM image where sand ripples are nearly parallel to along-track direction.

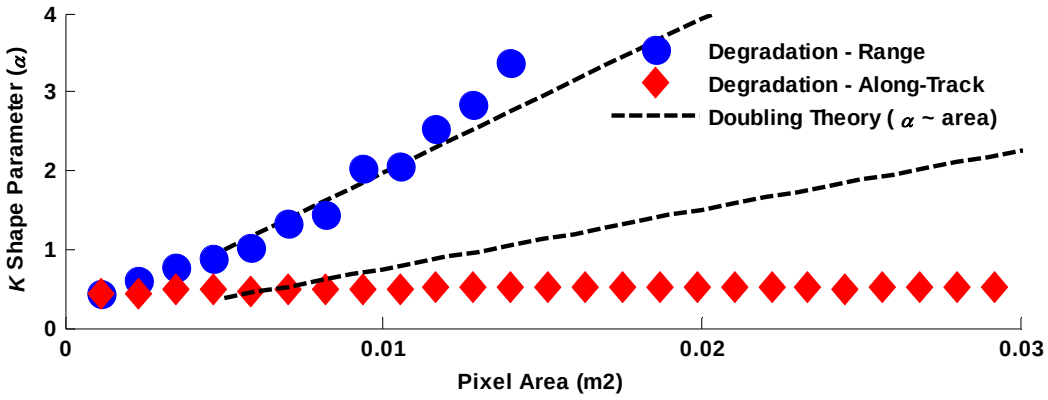

Figure 4.7: *K* distribution shape parameter estimates vs. resolution of Figure 4.6 in one-dimension.

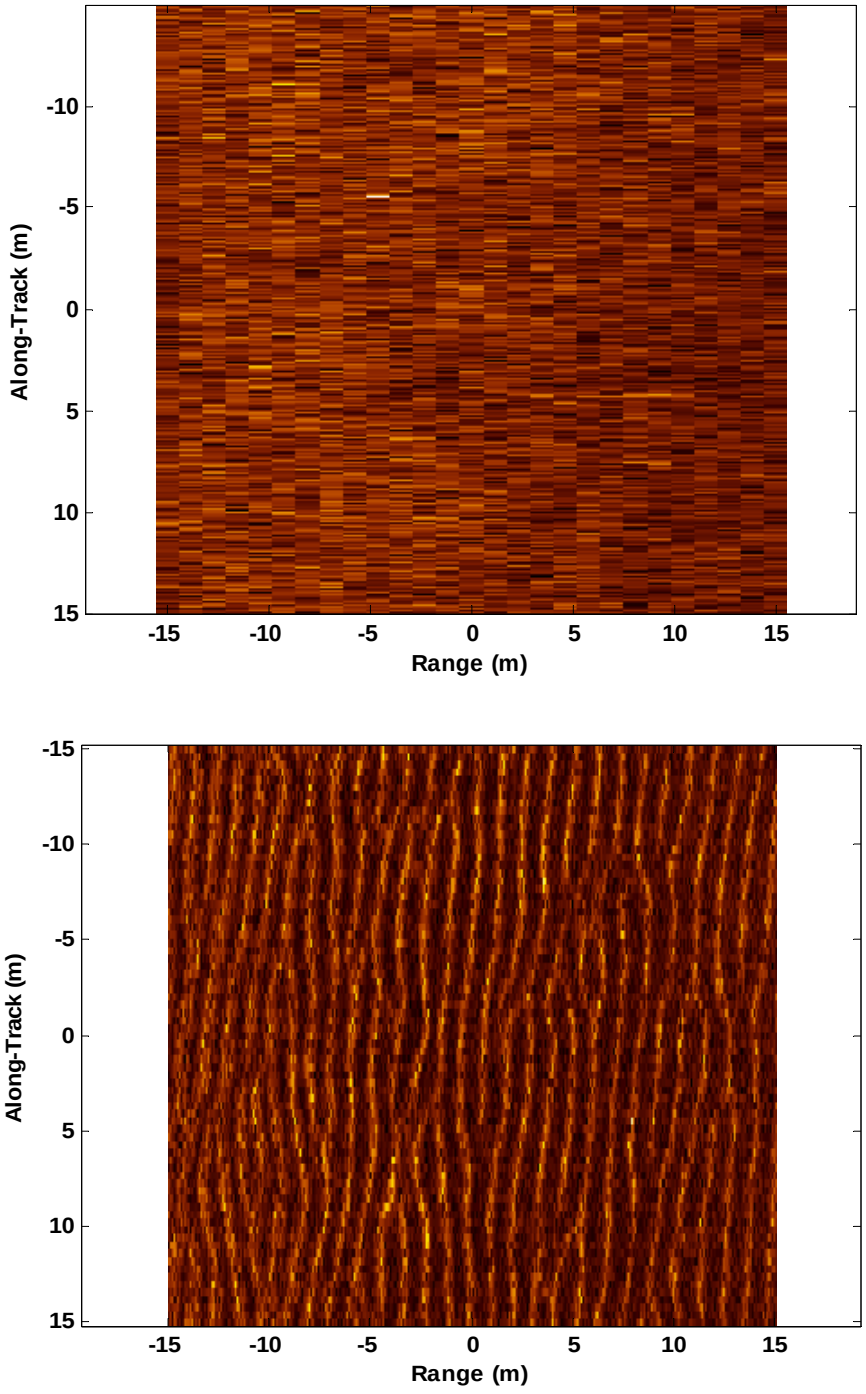

Figure 4.8: Resolution-reduced versions of Figure 4.6 using $1/10^{th}$ of the slant-range (top) and along-track (bottom) bandwidths.

Statistical analysis can also be performed by varying the resolution in both dimensions simultaneously producing any pixel dimensions desired (within the constraint that the final image is supported appropriately by the raw data and a useful final resolution). For the results presented here, integer divisions of original bandwidth were used creating integer multiples of the original image resolution cell size, although this need not be the case. Figures 4.9 and 4.10 show four images with various seafloor orientations collected with the HF band of the SSAM system on the left, and corresponding two-dimensional statistical analysis on the right (the synthetic aperture to ripple orientations of the images are Ψ = 6°, 69°, 78°, and 86°). The color plots on the right show *K* distribution shape parameter estimates for simultaneous two-dimensional resolution-reduction of the corresponding image which have been scaled by the estimate of the full resolution image. Beginning with the estimated shape parameter for the original full-resolution image at the lower left of the color plot, range resolution-reduction is performed and the results shown along the horizontal axis (this is the same as the blue dots of Figure 4.7). Similarly, cross-range resolution-reduction results are shown along the vertical axis, with simultaneous two-dimensional reductions along diagonals (this is the same as the red diamonds of Figure 4.7). For the top image of Figure 4.9 where the synthetic aperture is nearly parallel to the ripple crests, there is very little increase in shape parameter with cross-range reduction, while reduction in the range dimension produces significantly more Rayleigh-like image statistics (a result that is verified with the one-dimensional results of Figure 4.7 and Figure 4.8). As the angle between the aperture and ripple crest increases towards 90° (bottom image of Figure 4.10), the trends shift such that degradation produces nearly equal trends to

Rayleigh-like statistics in both dimensions. Here it is important to consider the geometry associated with the generation of the image, and the local acoustic slope that determines the local backscattering strength.

These trends in shape parameter can be considered in terms of acoustic scattering cross section, which determines inter-pixel image intensity and resulting image statistics. As resolution is degraded, more scattering patches are included in the area that determines individual pixel intensity, effectively 'smoothing' the high and low scattered intensities reducing the inter-pixel variance (or reducing the tails of an image's normalized envelope distribution). This phenomena has been reported in the literature as a 'directional filter of seabed texture' in [Bell *et al*. 1999], and is also seen in [Tang *et al*. 2002] where an acoustic image of sand ripples has a higher contrast when the acoustic propagation direction is perpendicular to the ripples compared to when the direction is parallel to the ripple crests. In both of these situations, this is the result of a low grazing angle combined with orientation of the sea-floor correlation to the Sonar.

In terms of applicability of the Central Limit Theorem, increasing the area increases the number of contributing scatterers or range of slopes which determines the backscattering strength for the case of sand ripples, thus making reverberation more Rayleigh-like given appropriate distributions of scatterer sizes or slopes and positions within the ensonified area. Yet again, we can return to the Random Walk analogy for reverberation, where each ripple crest can be viewed as biasing the walk in a particular direction. As we combine biased random walks associated with the same direction, the

net direction is essentially in the original direction. However, if we combine biased random walks where each walk is biased in a different direction, the net direction is much more random, and given a sufficient number of uniformly distributed biased random walks, the Central Limit Theorem can be applied with a resulting Rayleigh probability distribution about the origin.

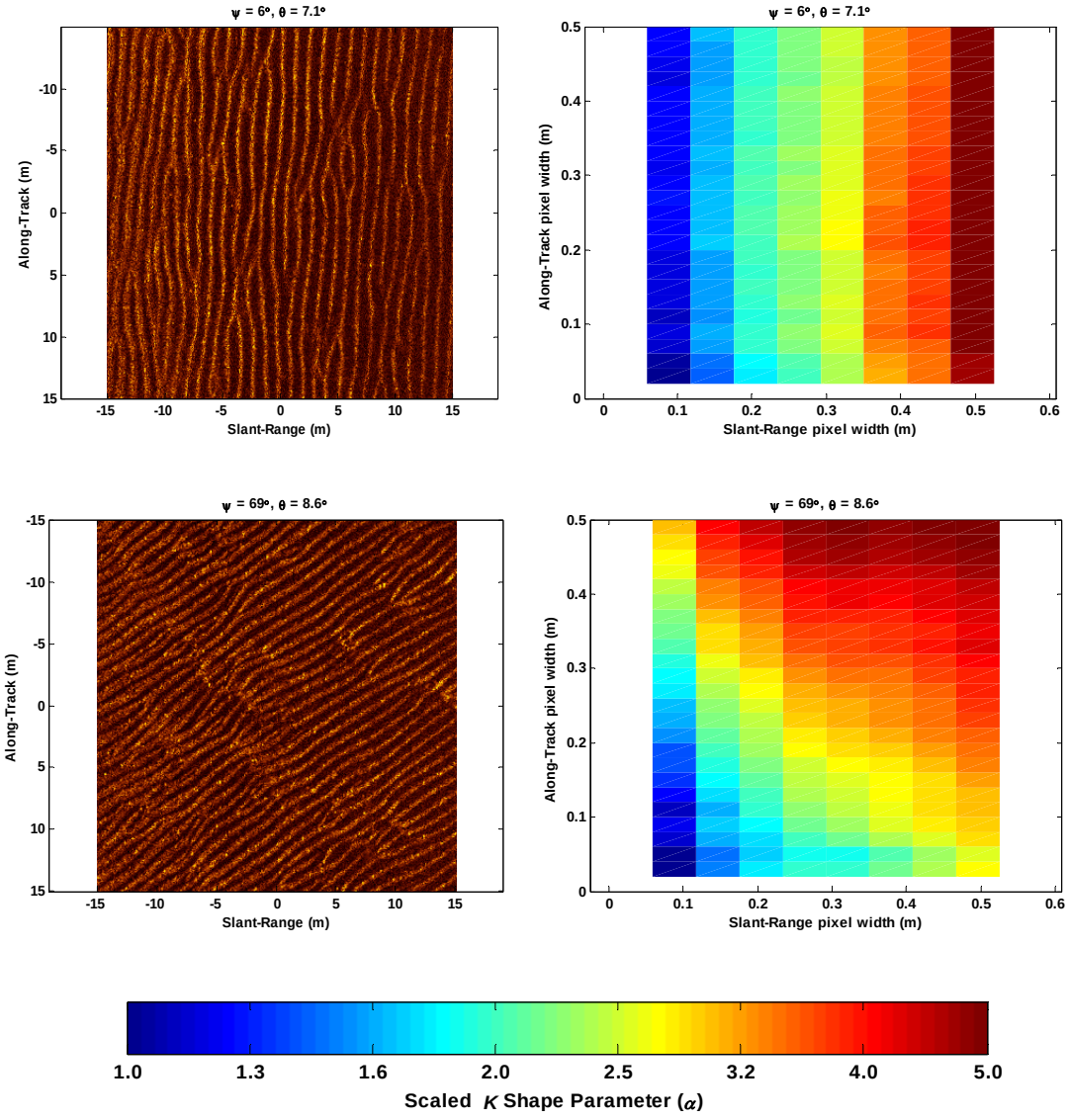

Figure 4.9: Shape parameter estimates vs. resolution in two-dimensions for experimental SAS images of seafloors with various aspects to the synthetic aperture: 6° (top) and 69° (bottom).

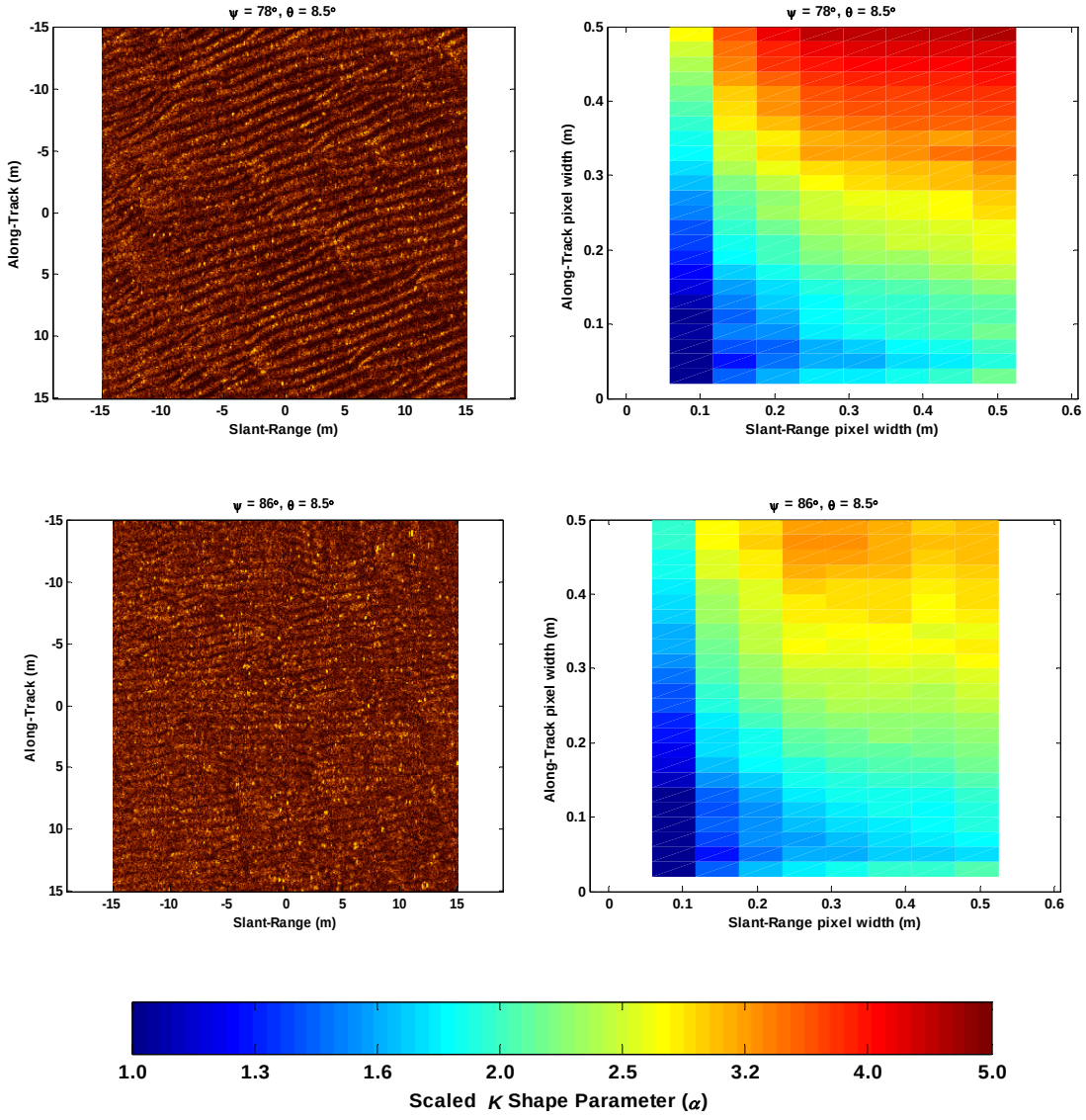

Figure 4.10: Shape parameter estimates vs. resolution in two-dimensions for experimental SAS images of seafloors with various aspects to the synthetic aperture: 78° (top) and 86° (bottom).

4.4 Simulation of Resolution Adjustment and Comparison

Utilizing the rippled-sand acoustic simulation of Section 2.4.2, surfaces with various aspect orientations can be simulated. Figures 4.11 and 4.12 show four simulated images with increasing angular rotation of the Sonar to a rippled seafloor (from the along-track direction being parallel to ripple crests on the where $\Psi = 0°$, top Figure 4.11, to the along-track direction being perpendicular to the ripple crests on the bottom where $\Psi = 90°$, bottom Figure 4.12). As in Figures 4.9 and 4.10, plots of the corresponding estimates of shape parameter versus two-dimensional resolution adjustment are shown on the right. Figure 4.13 shows the comparison of estimated shape parameter versus one-dimensional resolution adjustment for experimental data and numerical simulation for the extreme cases of the synthetic aperture parallel to ($\Psi = 0°$) and perpendicular to ($\Psi = 90°$) ripple crests. As anticipated, for both actual and synthetic data resolution adjustment shows greater symmetry between slant-range and along-track resolution adjustment when the synthetic aperture to ripple orientation is perpendicular, compared to parallel.

In general, the simulation provides good agreement both visually and statistically with the experimental data analysis results. The most noticeable difference is that the simulation estimates tends more towards Rayleigh-like statistics than does the experimental data estimates with simultaneous slant-range and along-track resolution reduction. Careful examination of the experimental versus simulated images reveals this is most likely caused by the location of the ‘speckles’ in the simulated images. Recalling

Section 2.4.2, a compound representation of multiplicative speckle was applied during the simulation of images. While this is a common method to simulate speckle [Goodman 2007], it drives the placement of speckles to locations where the image has a non-zero value, notably along the ripple crests which have higher acoustic backscattering than the troughs. While the spacing between the simulated speckles appears similar to experimental speckle, the experimental speckle persists in the troughs particularly for the perpendicular case (*i.e.* where Ψ approaches 90°), thus causing the experimental data to retain significantly non-Rayleigh statistics with resolution degradation compared to the simulation. While additive speckle produces a visually pleasing comparison the physical basis for this is unjustified, and without ground-truth to confirm or deny presence of sediment inhomogeneties or biological source (*e.g.*, shell fragments or sand dollars) that may be causing this result, multiplicative speckle is assumed. Analysis of image speckle with corresponding ground truth is required to proceed. Despite a difference in the placement of speckle, the agreement between experimental and simulated statistical results is striking.

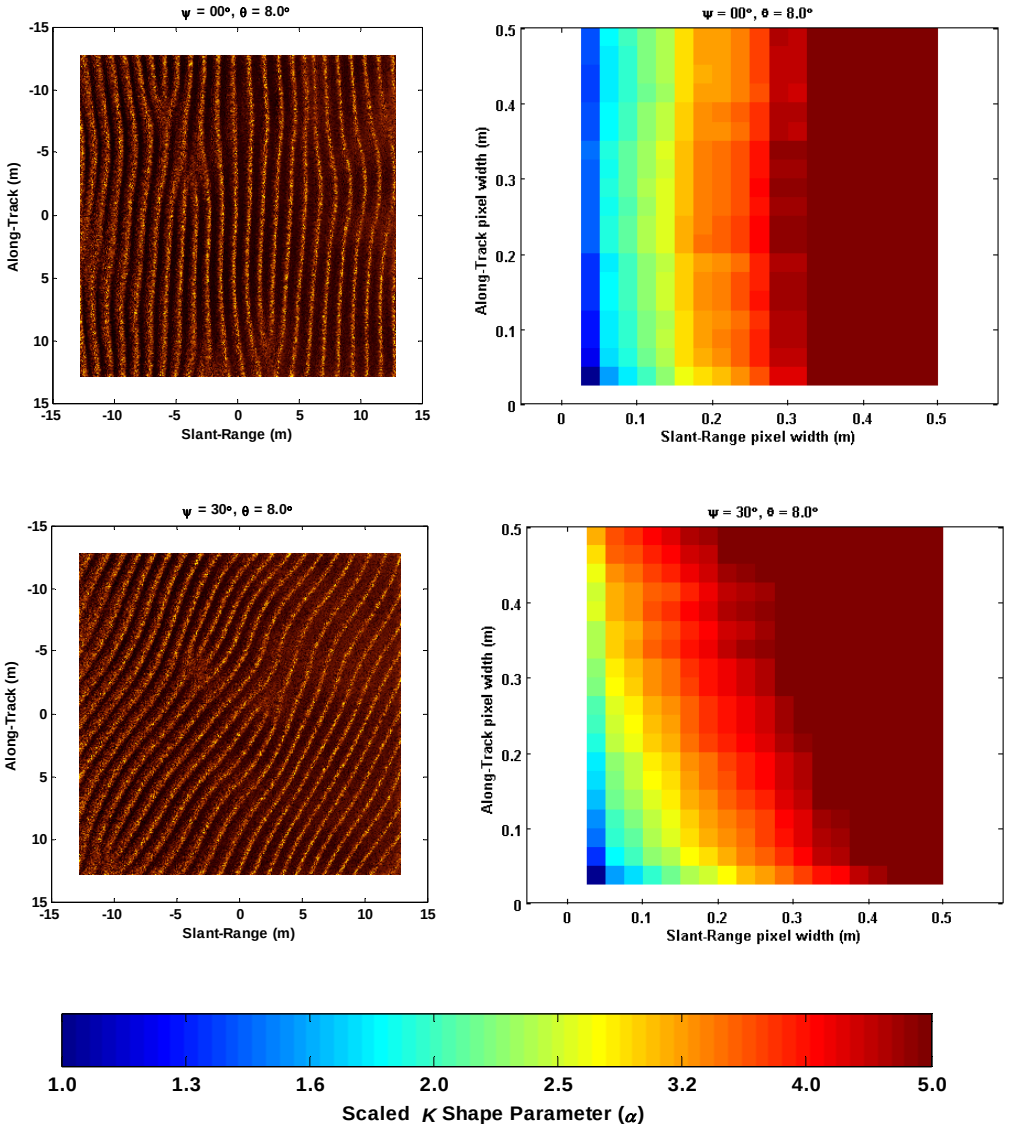

Figure 4.11: Shape parameter estimates vs. resolution in two-dimensions for simulated SAS images of seafloors with various aspects to the synthetic aperture: 0° (top) and 30° (bottom).

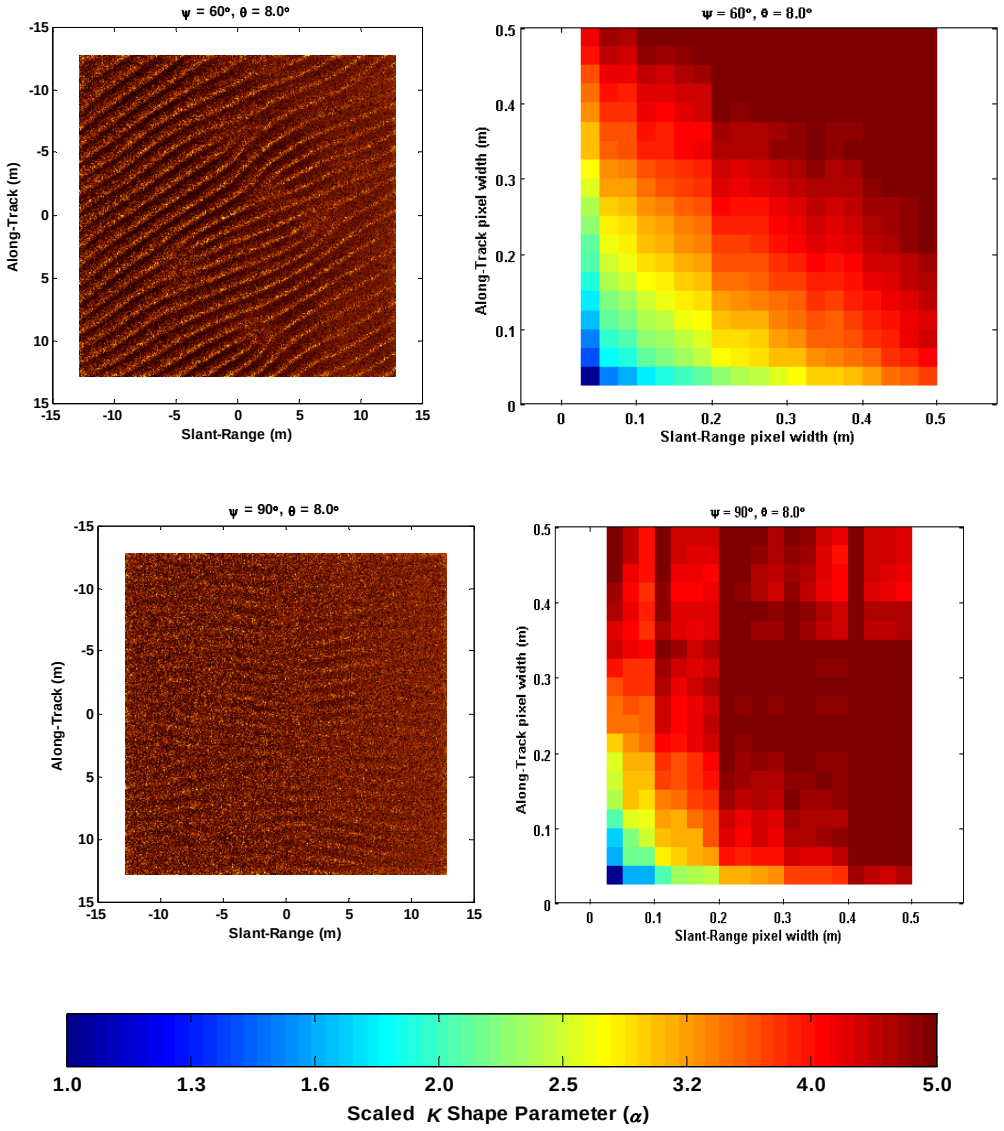

Figure 4.12: Shape parameter estimates vs. resolution in two-dimensions for simulated SAS images of seafloors with various aspects to the synthetic aperture: 60° (top) and 90° (bottom).

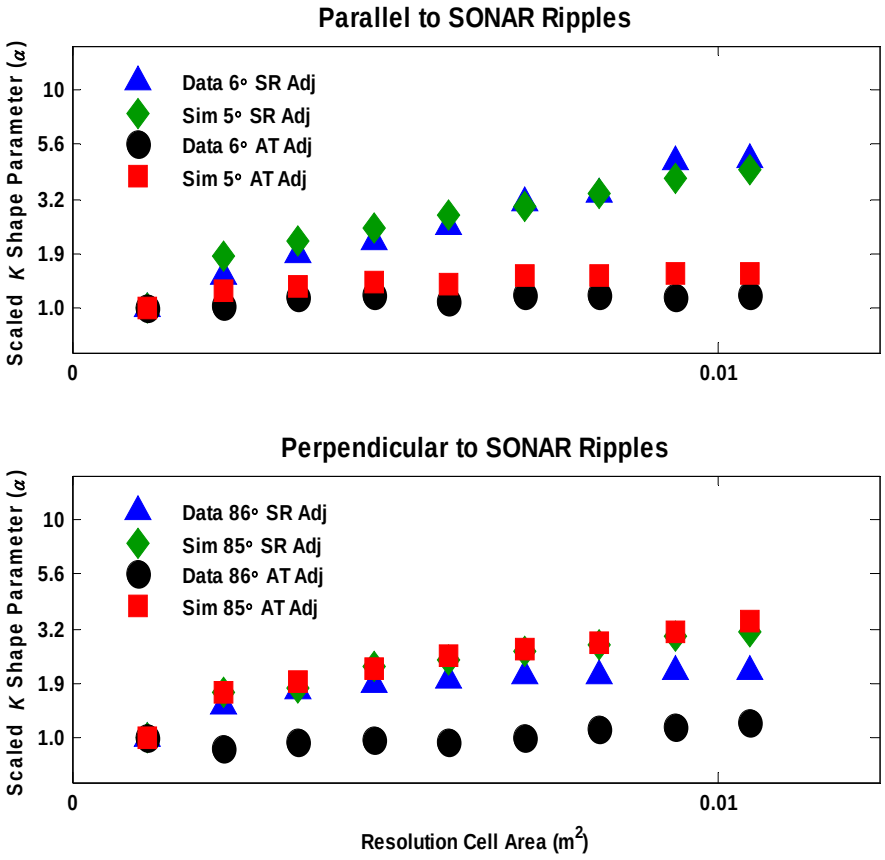

Figure 4.13: Comparison of shape parameter estimates vs. resolution in one-dimension for experimental data and numerical simulation.

Chapter 5

Summary and Conclusions

5.1 Summary and Conclusions

The work presented in this thesis consists of several varied explorations, all falling under the over-arching theme of Synthetic Aperture Sonar image statistics. The unique properties resulting from the synthetic aperture formation process, combined with two sets of experimental data, provided an opportunity for implementing new statistical analyses, models, and numerical simulation methods, furthering understanding of the interplay between the acoustic response of the ocean environment and Sonar system parameters. The K distribution shape parameter was used to represent the reverberation statistics with large values indicating a trend toward Rayleigh-distributed reverberation. A brief summary and conclusions for each of three major contributions of this work follow.

Although numerous techniques have been proposed, the problem of generating physics-based synthetic data continues to plague the Radar and Sonar communities. With the increased use of computer-aided detection and classification systems to help mitigate high data rates and increasing Probability of False Alarms with increasing system resolution, and an inability to collect training data for every sort of environment encountered, realistic simulation of cluttered reverberation is of paramount importance.

This work has introduced a new method for simulating acoustic reverberation from rippled sand which takes into account Sonar system parameters, sediment characteristics, and orientation to the sea-floor to produce synthetic acoustic images which agree well both visually and statistically with collected data.

Multipath contamination poses a challenge for Sonar system design, particularly when attempting to image at ranges greater than the water depth. Multipath tends to fill in shadows which are vital for classification algorithms, may ghost targets, or even cause unusable images by both reducing image quality and rendering certain data-driven motion compensation algorithms ineffective. Although this phenomenon is certainly not confined to Synthetic Aperture Sonar, SAS does provide a unique opportunity to explore the statistical impact of multipath because of the fixed-with-range along-track resolution. Previous work on this topic has been either theoretical or not definitively conclusive, and the majority of effort for high-frequency systems has been concentrated on development of advanced vertical beamforming techniques in an attempt to reject unintended off-axis reverberation.

Previous research has shown multipath to make reverberation statistics more Rayleigh-like, a result of multiple contemporaneous realizations increasing the statistical randomness. Analysis, modeling, and simulation of structural and environmentally induced multipath in this work confirmed this. Modeling and simulation also elucidated a requirement that the Sonar system configuration and environment must act together to

cause the multipath and direct-path power levels to be within approximately 10 dB of each other for multipath to have a significant impact on the reverberation statistics.

Recent advances in motion-compensation now afford Synthetic Aperture Sonar systems the ability to generate photograph-like imagery of the sea-floor. However, high-resolution imagery of this sort is often characterized by a decidedly non-Rayleigh pixel amplitude distribution, owing in part to the high-resolution nature of the Sonar but also to the coherent synthetic aperture formation process which may produce speckle. The technique of incoherently averaging lower-resolution images created from independent spatial frequency sub-bands to mitigate speckle is sometimes employed. In general, decreasing the image resolution makes image statistics more Rayleigh-like by reducing the tails of the envelope probability density. This work has also shown the potentially adverse effects on detection ability when multilook is applied to a wide-bandwidth SAS.

Optimum detection ability requires thorough understanding of not only the intended target, but also the background. This work has shown through both data analysis and numerical simulation that resolution adjustment can be performed in two-dimensions simultaneously by limiting the spatial wavenumber bandwidth of an image, with the image statistics depending upon both the resolution and the orientation of the Sonar to the sea-floor in the presence of a strongly correlated feature such as sand-ripples. In such a scenario, the orientation plays as significant a role to the image statistics as does the system resolution. Useful resolution adjustment for the purposes of improving statistical characteristics of a SAS image must take into account not only the

characteristics of the target, but also the environmental response and orientation. Within these limitations, opportunity to significantly improve the False Alarm rate by orders of magnitude in regions of high clutter has been demonstrated.

5.2 Continuing these Explorations

This work has shown that predicting anticipated Synthetic Aperture Sonar image statistics requires an accurate understanding of seafloor backscattering, including correlations and sediment inhomogeneties. This must then be coupled with an accurate understanding of the particular remote sensing system involved, and any artifacts that may be induced. Specifically elucidated in this work is the need to better quantify the causes of speckle in Synthetic Aperture Sonar images. While it has been hypothesized that speckle is simply a system artifact that can be ignored and can be smoothed over by averaging looks from either multiple squint angles or frequency bands, it has been shown here the potential for degraded performance exists with this sort of post-processing and may be avoided by implementation of *a priori* information concerning the target and background features. However, this requires first a better understanding of the sea-floor composition and ground-truth of actual SAS images to rule-out the potential for inhomogeneties such as sand dollars or debris that may cause speckle-like features. A second key component for improvement is modeling of the coherent imaging process when reflected and re-scattered by interaction with the time-varying sea-surface. This should be considered even when advanced beam-steering is employed as this work has shown statistical impact of multipath even when there is no visually apparent distortion

of the image. Only then can attention be turned to a more complete understanding of the causes of coherent imaging speckle with respect to SAS, specifically how the macroscopic representations arise from microscopic roughness in the presence of a dynamic environment, to ensure separation of system induced versus environmentally induced statistical properties. In conclusion, as our understanding of the interplay of environmental and Sonar system parameters continues to develop, so too does our ability to make effective use of the information collected by such systems.

Bibliography

Abraham, D. A.,1997. "Modeling non-Rayleigh reverberation," SACLANT Undersea Research Centre, La Spezia SR-266,

Abraham, D. A., 2007. "The effect of multipath on the envelope statstics of bottom clutter," *IEEE J. Ocean. Eng.,* vol. 32, October, pp. 848-861.

Abraham, D. A. and Johnson, S. F., 2008. "Statistical modeling of broadband clutter," in *International Symposium on Underwater Reverberation and Clutter*, P. L. Nielsen, C. H. Harrison, and J.-C. L. Gac, eds., Lerici, Italy, pp. 247-254.

Abraham, D. A. and Lyons, A. P., 2002a. "Reverberation envelope statistics and their dependence on sonar beamwidth and bandwidth," in *Impact of Littoral Environmental Variability on Acoustic Predictions and Sonar Performance*, N. G. Pace and F. B. Jensen, eds., Kluwer Academic Publishers, Lerici, Italy, pp. 536-546.

Abraham, D. A. and Lyons, A. P., 2002b. "Novel physical interpretations of K-distributed reverberation," *IEEE J. Ocean. Eng.,* vol. 27, October, pp. 800-813.

Abraham, D. A. and Lyons, A. P., 2004a. "Reverberation envelope statistics and their dependence on sonar bandwidth and scattering patch size," *IEEE J. Ocean. Eng.,* vol. 29, January, pp. 126-137.

Abraham, D. A. and Lyons, A. P., 2004b. "Simulation of non-Rayleigh reverberation and clutter," *IEEE J. Ocean. Eng.,* vol. 29, April, pp. 347-362.

Abraham, D. A. and Lyons, A. P., 2006. "Bootstrapped K-distribution parameter estimation," in *Oceans 2006* IEEE, Boston, Massachusetts, pp. 1-6.

Annis, C., 2008. http://www.statisticalengineering.com.

Becker, K. M., 2004. "Effect of various surface-height-distribution properties on acoustic backscattering statistics," *IEEE J. Ocean. Eng.,* vol. 29, April, pp. 246-259.

Bell, J. M., Chantier, M. J., and Wittig, T., 1999. "Sidescan sonar: a directional filter of seabed texture?," *IEE Proc. - Radar, Sonar Navig.,* vol. 146, February, pp. 65-72.

Bell, J. M. and Linnett, L. M., 1997. "Simulation and analysis of synthetic sidescan sonar images," *IEE Proc. - Radar, Sonar Navig.,* vol. 144, August, pp. 219-229.

Bellettini, A. and Pinto, M., 2002. "Theoretical accuracy of synthetic aperture sonar micronavigation using a displaced phase-center antenna," *IEEE J. Ocean. Eng.,* vol. 27, October, pp. 780-789.

Bellettini, A. and Pinto, M., 2008. "Design and experimental results of a 300-kHz Synthetic Aperture Sonar optimized for shallow-water operations," *IEEE J. Ocean. Eng.,* accepted.

Bellettini, A., Pinto, M., and Wang, L., 2003. "Effect of multipath on synthetic aperture sonar," in *World Congress on Ultrasonics 2003* Paris, France, pp. 531-534.

Bendat, J. S. and Piersol, A. G., 2000. *Random Data Analysis and Measurement Procedures*, 3rd ed., New York, Wiley.

Bennett, J. R., Cumming, I. G., Deane, R. A., Widmer, P., Fielding, R., and McConnell, P., 1979. "SEASAT imagery shows St. Lawrence," *Aviation Week and Space Technology,* February.

Bennett, W. R., 1956. "Methods of solving noise problems," *Proceedings of the IRE,* vol. 55, pp. 609-638.

Berman, D. H., 1991. "Simulations of rough interface scattering," *J. Acoust. Soc. Am.,* vol. 89, February, pp. 623-636.

Bisceglie, M. D., Galdi, C., and Griffiths, H. D., 1999. "Statistical scattering model for high-resolution sonar images: characterisation and parameter estimation," *IEE Proc. - Radar, Sonar and Navigation,* vol. 146, October, pp. 264-272.

Blacknell, D., 1994b. "New method for the simulation of K distributed clutter," *IEE Proc. - Radar, Sonar and Navigation,* vol. 141, February, pp. 53-58.

Blacknell, D., 1994c. "Comparison of parameter estimators for K-distribution," *IEE Proc. - Radar, Sonar Navig.,* vol. 141, February, pp. 45-52.

Blacknell, D., Blake, A., Lombardo, P., and Oliver, C. J., 1994a. "A comparison of simulation techniques for correlated Gamma and *K*-distributed images for SAR applications," in *IGARSS '94, International Geoscience and Remote Sensing Symposium* IEEE, Pasadena, CA.

Blacknell, D. and Tough, R. J. A., 2001. "Parameter estimation for the K-distribution based on [z log(z)]," *IEE Proc. - Radar, Sonar Navig.,* vol. 148, December, pp. 309-312.

Blake, A. P., Blacknell, D., and Oliver, C. J., 1995. "Texture simulation and analysis in coherent imagery," in *5th International Conference on Image Processing and its Applications* IEEE, pp. 772-776.

Brown, D., Cook, D., and Fernandez, J., 2006. "Results from a small Synthetic Aperture Sonar," in *Oceans 2006* IEEE, pp. 1-6.

Burdic, W. S., 2002. *Underwater Acoustic System Analysis*, 2nd ed., Los Altos, Peninsula Publishing.

Callow, H. J., 2003. "Signal processing for synthetic aperture sonar image enhancement," *Ph.D. Thesis in Electrical and Electronic Engineering*, University of Canterbury, Christchurch, New Zealand.

Carrara, W. G., Goodman, R. S., and Majewski, R. M., 1995. *Spotlight Synthetic Aperture Radar*, Boston, Artech House.

Chanussot, J., Maussang, F., and Hétet, A., 2002. "Scalar image processing filters for speckle reduction on synthetic aperture sonar images," in *Oceans 2002* IEEE, pp. 2294-2301.

Chen, Q., Xu, W., Pan, X., and Li, J., 2008. "Wideband multipath rejection in synthetic aperture sonar imaging," in *Oceans 2008* IEEE.

Chotiros, N. P., Boehme, H., Goldsberry, T. G., S. P. Pitt, Lamb, R. A., Garcia, A. L., and Altenburg, R. A., 1985. "Acoustic backscattering at low grazing angles from the ocean bottom. Part II. Statistical characteristics of bottom backscatter at a shallow water site," *J. Acoust. Soc. Am.,* vol. 77, March, pp. 975-982.

Chung, P.-J., Roberts, W. J. J., and Böheme, J. F., 2005. "Recursive K-distribution parameter estimation," *IEEE Trans. Signal Processing,* vol. 53, February, pp. 397-402.

Cobb, J. T. and Stack, J. R., 2007. "In situ adaptive feature extraction for underwater target classification," in *36th Applied Imagery Pattern Recognition Workshop* IEEE, pp. 42-47.

Cole, B., Davis, J., Leen, W., Powers, W., and Hanrahan, J., 2004. "Coherent bottom reverberation: modeling and comparisons with at-sea measurements," *J. Acoust. Soc. Am.,* vol. 116, October, pp. 1985-1994.

Conte, E., Bisceglie, M. D., and Galdi, C., 1993. "Modelling and simulation of bidimensional processes for remote sensing applications," in *Geoscience and Remote Sensign Symposium, IGARSS '93* IEEE, pp. 1993-1995.

Cook, D. A., 2007. "Synthetic Aperture Sonar motion estimation and compensation," *M.S. Thesis in Electrical and Computer Engineering*, Georgia Institute of Technology.

Cook, D. A., Christoff, J. T., and Fernandez, J. E., 2003. "Motion compensation of AUV-based synthetic aperture sonar," in *Oceans 2003* IEEE, pp. 2143-2148 Vol.4.

Cook, D. A., Stroud, J. S., Fernandez, J. E., and Lathrop, J. D., 2005. "Results from a hybrid synthetic aperture sonar motion estimation scheme," in *Oceans 2005 Europe* IEEE, pp. 1376-1381 Vol. 2.

Corsini, G., Manara, G., and Monorchio, A., 1996. "Simulation of RAR reflectivity maps of the sea surface for remote sensing applications," in *IGARSS '96, International Geoscience and Remote Sensing Symposium, Remote Sensing for a Sustainable Future* IEEE, pp. 290-292.

Crowther, P. A., 1980. *Fluctuation Statistics of Sea-Bed Acoustic Backscatter*, New York, Plenum.

Cumming, I. G. and Wong, F. H., 2005. *Digital Processign of Synthetic Aperture Radar Data*, Boston, Artech House.

Curlander, J. C. and McDonough, R. N., 1991. *Synthetic Aperture Radar, Systems and Signal Processing*, New York, Wiley.

Davidson, G., Griffiths, H. D., and Ablett, S., 2002. "Statistical analysis of high resolution land clutter," in *RADAR 2002* IEEE, pp. 434-438.

Davidson, G., Griffiths, H. D., and Ablett, S., 2004. "Analysis of high-resolution land clutter," *IEE Proc. Vision, Image and Signal Processing,* vol. 151, February, pp. 86-91.

Davis, B., Gough, P., and Hunt, B., 2002. "Sea surface simulator for testing a synthetic aperture sonar," in *Impact of Littoral Environmental Variability on Acoustic Predictions and Sonar Performance*, N. G. Pace and F. B. Jensen, eds., La Spezia, Italy, pp. 173-180.

Dobeck, G. J., 1999. "Fusing sonar images for mine detection and classification," in *Detection and Remediation Technologies for Mines and Minelike Targets IV*, A. C. Dubey, J. F. Harvey, J. T. Broach, and R. E. Dugan, eds., SPIE, pp. 602-614.

Dobeck, G. J., 2001. "Algorithm fusion for automated sea mine detection and classification," in *Oceans 2001* IEEE, pp. 130-134 vol.1.

Dobeck, G. J. and Cobb, J. T., 2002. "Fusion of multiple quadratic penalty function support vector machines (QPFSVM) for automated sea mine detection and classifcation," in *Detection and Remediation Technologies for Mines and Minelike Targets VII*, J. T. Broach, R. S. Harmon, and G. J. Dobeck, eds., SPIE, pp. 401-411.

Dobeck, G. J., Hyland, J. C., and Smedley, L. D., 1997. "Automated detection/classification of sea mines in sonar imagery," in *Detection and Remediation Technologies for Mines and Minelike Targets II*, J. T. Broach, R. S. Harmon, and G. J. Dobeck, eds., SPIE, pp. 90-110.

Dong, Y.,2004. "Clutter spatial distribution and new approaches of parameter estimation for Weibull and K-distributions," Defense Science and Technology Organization, Edinburgh, South Australia, Research Report

Elston, G. R. and Bell, J. M., 2004. "Pseudospectral time-domain modeling of non-Rayleigh reverberation: synthetis and statistical analysis of a sidescan sonar image of sand ripples," *IEEE J. Ocean. Eng.,* vol. 29, April, pp. 317-329.

Fernandez, J. E., Matthews, A. D., Cook, D. A., and Stroud, J. S., 2004. "Synthetic Aperture Sonar development for autonomous underwater vehicles," in *Oceans 2004* IEEE, pp. 1927-1933 Vol.4.

Fisz, M., 1978. *Probability Theory and Mathematical Statistics*, 4th ed., New York, Mac-millian.

Fortune, S. A., Hayes, M. P., and Gough, P. T., 2003. "Speckle reduction of synthetic aperture sonar images," in *World Congress on Ultrasonics 2003* Paris, France, pp. 669-672.

Franceschetti, G., Migliaccio, M., and Riccio, D., 1998. "On ocean SAR raw signal simulation," *IEEE Trans. Geosci. Remote Sens.,* vol. 36, January, pp. 84-100.

Gabor, D., 1972. "Holography, 1948-1971," *Science,* vol. 177, July, pp. 299-313.

Gascón, F. and Salazar, F., 2006. "A simple method to simulate diffraction and speckle patterns with a PC," *Optick,* vol. 117, pp. 49-57.

Gaumond, C. F., Soukup, R., and Baer, R. N., 2008. "Information requirements for active classification using physics-based signal models," in *International Symposium on Underwater Reverberation and Clutter*, P. L. Nielsen, C. H. Harrison, and J.-C. L. Gac, eds., Lerici, Italy, pp. 321-328.

Gazagnaire, J., Beaujean, P., and Stack, J., 2007. "Combining model-based and in situ performance prediction to evaluate detection & classification performance," *Proceedings of the Institute of Acoustics,* vol. 29.

Goodman, J. W., 1976. "Some fundamental properties of speckle," *J. Opt. Soc. Am.,* vol. 66, November, pp. 1145-1150.

Goodman, J. W., 2000. *Statistical Optics*, New York, Wiley.

Goodman, J. W., 2005. *Introduction to Fourier Optics*, 3rd ed., Englewood, Roberts & Company.

Goodman, J. W., 2007. *Speckle Phenomena in Optics, Theory and Applications*, Englewood, Roberts & Company.

Gordon, S. D. and Ritcey, J. A., 1995. "Calculating the K-distribution by saddlepoint integration," *IEE Proc. - Radar, Sonar Navig.,* vol. 142, August.

Gough, P. T. and Hawkins, D. W., 1997a. "Imaging algorithms for a strip-map synthetic aperture sonar: minimizing the effects of aperture errors and aperture undersampling," *IEEE J. Ocean. Eng.,* vol. 22, January, pp. 27-39.

Gough, P. T. and Hawkins, D. W., 1997b. "Unified framework for modern synthetic aperture imaging algorithms," *International Journal of Imaging Systems and Technology,* vol. 8, pp. 343-358.

Griffiths, H., Dulop, J., and Voles, R., 1997. "Texture analysis of sidescan sonar imagery using statistical scattering models," in *High Frequency Acoustics in Shallow Water*, N. G. Pace, E. Pouliquen, O. Bergem, and A. P. Lyons, eds., NATO SACLANTCEN, Lerici, Italy.

Griffiths, H. D., 2003. "Synthetic aperture imaging with sonar and radar: a comparison," in *World Congress on Ultrasonics 2003* Paris, France, pp. 511-518.

Harris, F. J., 1978. "On the use of windows for harmonic analysis with the discrete Fourier transform," *Proceedings of the IEEE,* vol. 66, pp. 51-83.

Hawkins, D. W., 1996. "Synthetic aperture imaging algorithms: with application to wide bandwidth sonar," *Ph.D. Thesis in Electrical and Electronic Engineering*, University of Canterbury, Christchurch, New Zealand.

Hayes, M. H., 2002. *Statistical Digital Signal Processing and Modeling*, New York, Wiley.

Hayes, M. P., 2004. "Multipath reduction with a three element interferometric synthetic aperture sonar," in *7th European Conference on Underwater Acoustics* Delft, The Netherlands.

Iskander, D. R., A. M. Zoubir, B. Boashash, 1999. "A method for estimating the parameters of the K distribution," *IEEE Trans. Signal Processing,* vol. 47, April, pp. 1147-1151.

Iskander, D. R. and Zoubir, A. M., 1996. "Estimating the parameters of the K-distribution using the ML/MOM approach," in *TENCON '96, Digital Signal Processing Applications* Perth, Australia.

Jackson, D. R., M. D. Richardson, 2007. *High-Frequency Seafloor Acoustics*, New York, Springer.

Jahangir, M., Blackwell, D., and White, R. G., 1996. "Accurate approximation to the optimum parameter estimate for K-distributed clutter," *IEE Proc. - Radar, Sonar Navig.,* vol. 143, December, pp. 383-390.

Jakeman, E., 1980. "On the statistics of *K*-distributed noise," *J. Phys. A: Math. Gen.,* vol. 13, pp. 31-48.

Jakeman, E., 1982a. "Fresnel scattering by a corrugated random surface with fractal slope," *J. Opt. Soc. Am.,* vol. 72, pp. 1034-1041.

Jakeman, E., 1982b. "Scattering by a corrugated random surface with fractal slope," *J. Phys. A: Math. Gen.,* vol. 15, pp. L55-L59.

Jakeman, E. and Pusey, P. N., 1975. "Non-Gaussian fluctuations in electromagnetic radiation scattered by a random phase screen. I. Theory," *Journal of Physics A - Mathematical and General,* vol. 8, pp. 369-391.

Jakeman, E. and Pusey, P. N., 1976. "A model for non-Rayleigh sea echo," *IEEE Trans. Antennas Propogat.,* vol. 24, Nov., pp. 806-814.

Jakeman, E. and Pusey, P. N., 1978. "Significance of K-distributions in scattering experiments," *Physical Review Letters,* vol. 40, pp. 546-550.

Jakeman, E. and Tough, R. J. A., 1988. "Non-Gaussian models for the statistics of scattered waves," *Advances in Physics,* vol. 38, pp. 471-529.

Jensen, F. B., 2008. *Sonar Acoustics Handbook*, La Spezia, Italy.

Johnson, K. A., Hayes, M. P., and Gough, P. T., 1995. "A method for estimating the sub-wavelength sway of a sonar towfish," *IEEE J. Ocean. Eng.,* vol. 20, October, pp. 258-267.

Johnson, S. F., Lyons, A. P., and Abraham, D. A., 2005. "Bandwidth dependence of high-frequency seafloor backscatter statistics," in *Boundary Influences In High Frequency, Shallow Water Acoustics*, N. G. Pace and P. Blondel, eds., University of Bath, UK.

Johnson, S. F., Lyons, A. P., and Abraham, D. A., 2008. "Dependence of synthetic aperture sonar image statistics on resolution," in *International Symposium on Underwater Reverberation and Clutter*, P. L. Nielsen, C. H. Harrison, and J.-C. L. Gac, eds., Lerici, Italy, pp. 217-224.

Johnston, S. F., 2005. "From white elephant to Nobel Prize: Dennis Gabor's wavefront reconstruction," *Historical Studies in the Physical and Biological Sciences,* vol. 36, pp. 35-70.

Joughin, I. R., Percival, D. B., and Winebrenner, D. P., 1993. "Maximum likelihood estimation of K distribution parameters for SAR data," *IEEE Trans. Geosci. Remote Sens.,* vol. 31, September, pp. 989-999.

Kay, S. M., 1998. *Fundamentals of Statistical Signal Processing, Detection Theory*, Upper Saddle River, Prentice Hall.

Kinsler, L. E., Frey, A. R., Coppens, A. B., and Sanders, J. V., 2000. *Fundamentals of Acoustics*, 4th ed., New York, Wiley.

Lawrence, P. E. and Szabo, A. P., 2003. "Clutter simulation in maritime environments," in *International Conference on Radar* IEEE, pp. 619-624.

LePage, K. D., 2004. "Statistics of broad-band bottom reverberation predictions in shallow-water waveguides," *IEEE J. Ocean. Eng.,* vol. 29, April, pp. 330-346.

Lurton, X., 2004. *An Introduction to Underwater Acoustics - Principles and Applications*, Berlin, Praxis.

Lyons, A. P. and Abraham, D. A., 1999. "Statistical characterization of high-frequency shallow-water seafloor backscatter," *J. Acoust. Soc. Am.,* vol. 106, September, pp. 1307-1315.

Lyons, A. P., Abraham, D. A., and Johnson, S. F., 2005. "Statistical analysis of synthetic aperture sonar reverberation," in *Boundary Influences in High Frequency, Shallow Water Acoustics*, N. G. Pace and P. Blondel, eds., University of Bath, UK.

Lyons, A. P., Fox, W. L. J., Hasiotis, T., and Pouliquen, E., 2002. "Characterization of the two-dimensional roughness of wave-rippled sea floors using digital photogrammetry," *IEEE J. Ocean. Eng.,* vol. 27, July, pp. 515-524.

Lyons, A. P., Johnson, S. F., and Abraham, D. A., 2009. "High-frequency envelope statistics of patchy seafloors," *IEEE J. Ocean. Eng.,* accepted.

Marsaglia, G. and Tsang, W. W., 2000. "A simple method for generating gamma variables," *ACM Transactions on Mathematical Software,* vol. 26, September, pp. 363-372.

McDaniel, S. T., 1990. "Seafloor reverberation fluctuations," *J. Acoust. Soc. Am.,* vol. 88, pp. 1530-1535.

Medwin, H. and Clay, C. S., 1998. *Fundamentals of Acoustical Oceanography*, Boston, Academic Press.

Middleton, D., 1999. "New physical-statistical methods and models for clutter and reverberation: the KA-distribution and related probability structures," *IEEE J. Ocean. Eng.,* vol. 24, July, pp. 261-284.

Moreira, A., 1990. "An improved multi-look technique to produce SAR imagery," in *IEEE International Conference on Radar*, pp. 57-63.

Moreira, A., 1991. "Improved multilook techniques applied to SAR and SCANSAR imagery," *IEEE Trans. Geosci. Remote Sens.,* vol. 29, pp. 529-534.

Mourad, P. D. and Jackson, D. R., 1989. "High-frequency sonar equation models for bottom backscatter and forward loss," in *Oceans 1989* IEEE, pp. 1168-1175.

Mourad, P. D. and Jackson, D. R., 1993. "A model/data comparison for low-frequency bottom backscatter," *J. Acoust. Soc. Am.,* vol. 94, Jul, pp. 344-358.

Ogilvy, J. A. and Merklinger, H. M., 1991. "Theory of wave scattering from random rough surfaces," *J. Acoust. Soc. Am.,* vol. 90, December, pp. 3382-.

Oliver, C. J., 1986. "The interpretation and simulation of clutter textures in coherent images," *Inverse Problems,* vol. 2, pp. 481-518.

Oliver, C. J., 1988. "Representation of radar sea clutter," *IEE Proc. -F Radar Signal Process.,* vol. 135, December, pp. 497-500.

Oliver, C. J., 1993. "Optimum texture estimators for SAR clutter," *Journal of Physics D - Applied Physics,* vol. 26, Nov, pp. 1824-1835.

Papoulis, A. and Pillai, S. U., 2002. *Probability, Random Variables and Stochastic Processes*, 4th ed., Boston, Mc Graw Hill.

Peebles, P. Z. J., 2001. *Probability, Random Variables and Random Signal Principles*, 4th ed., New York, Mc Graw Hill.

Pinto, M., Bellettini, A., Wang, L. S., Munk, P., Myers, V., and Pautet, L., 2004. "A new synthetic aperture sonar design with multipath mitigation," in *High-Frequency Ocean Acoustics Conference* La Jolla, CA.

Preston, J. R. and Abraham, D. A., 2004. "Non-Rayleigh reverberation characteristics near 400 Hz observed on the New Jersey shelf," *IEEE J. Ocean. Eng.,* vol. 29, April, pp. 215-235.

Pusey, P. N. and Jakeman, E., 1975. "Non-Gaussian fluctuations in electromagnetic radiation scattered by a random phase screen. II. Application to dynamic scattering in a liquid-crystal," *Journal of Physics A - Mathematical and General,* vol. 8, pp. 392-410.

Raghavan, R. S., 1991. "A method for estimating parameters of K-distributed clutter," *IEEE Trans. Aerosp. Electron. Syst.,* vol. 27, March, pp. 238-246.

Rayleigh, L., 1919. "On the problem of random vibrations, and of random flights in one, two, or three dimensions," *The London, Edinburgh, and Dublin Philosophical Magazine and Journal of Science,* vol. 37, April, pp. 321-347.

Redding, N. J.,1999. "Estimating the parameters of the K distribution in the intensity domain," Defense Science and Technology Organisation, Salisbury, Australia, Research Report

Rees, W. G., 2001. *Physical Principles of Remote Sensing*, 2nd ed., Cambridge, Cambridge University Press.

Richardson, M. D., Briggs, K. B., Bibee, L. D., Jumars, P. A., Sawyer, W. S., Albert, D. B., Bennett, R. H., Berger, T. K., Buckingham, M. J., Chotiros, N. P., Dahl, P. H., Dewitt, N. T., Fleischer, P., Flood, R., Greenlaw, C. F., Holliday, D. V., Hulbert, M. H., Hutnak, M. P., Jackson, P. D., Jaffee, J. S., Johnson, H. P., Lavoie, D. L., Lyons, A. P., Martens, C. S., McGehee, D. E., Moore, K. D., Orsi, T. H., Piper, J. N., Ray, R. I., Reed, A. H., Self, R. F. L., Schmidt, J. L., Schock, S. G., Simoney, F., Stoll, R. D., Tang, D., Thistle, D. E., Thorsos, E. I., Walter, D. J., and Wheatcroft, R. A., 2001. "Overview of SAX99: environmental considerations," *IEEE J. Ocean. Eng.,* vol. 26, January, pp. 26-53.

Roberts, W. J. J. and Furui, S., 2000. "Maximum likelihood estimation of K-distribution parameters via the expectation-maximization algorithm," *IEEE Trans. Signal Processing,* vol. 48, December, pp. 3303-3306.

Sherwin, C. W., Ruina, J. P., and Rawcliffe, R. D., 1962. "Some early developments in synthetic aperture radar systems," *IRE Transactions on Military Electronics,* vol. 6, April, pp. 111-115.

Skinner, T. J., 1963. "Surface texture effects in coherent imaging," *J. Opt. Soc. Am.,* vol. 53, p. 1350.

Soumekh, M., 1994. *Fourier Array Imaging*, Englewood Cliffs, Prentice-Hall.

Soumekh, M., 1999. *Synthetic Aperture Radar Signal Processing*, New York, Wiley.

Steward, E. G., 2004. *Fourier Optics, An Introduction*, Mineola, Dover.

Stokey, R. P., Roup, A., von Alt, C., Allen, B., Forrester, N., Austin, T., Goldsborough, R., Purcell, M., Jaffre, F., Packard, G., and Kukulya, A., 2005. "Development of the REMUS 600 autonomous underwater vehicle," in *Oceans 2005* IEEE, pp. 1301-1304 Vol. 2.

Stolt, R. H., 1978. "Migration by Fourier-transform," *Geophysics,* vol. 43, pp. 23-48.

Tang, D., Henyey, F. S., Hefner, B. T., and Traykovski, P. A., 2009. "Simulating realistic-looking sediment ripple fields," *IEEE J. Ocean. Eng.,* accepted.

Tang, D., Williams, K. L., Thoros, E. I., and Briggs, K. B., 2002. "Remote sensing of sand ripples using high-frequency backscatter," in *Oceans 2002* IEEE, pp. 2081-2085 vol.4.

Tough, R. J. A. and Ward, K. D., 1999. "The correlation properties of gamma and other non-Gaussian processes generated by memoryless nonlinear transformation," *J. Phys. D: Appl. Phys.,* vol. 32, pp. 3075-3084.

Urick, R. J., 1983. *Principles of Underwater Sound*, 3rd ed., Los Altos, Peninsula Publishing.

Van Trees, H. L., 1968. *Detection, Estimation, and Modulation Theory - Part I*, New York, Wiley.

Wachowiak, M. P., Smolíková, R., Zurada, J. M., and Elmaghraby, A. S., 2002. "Estimation of *K* distribution parameters using neural networks," *IEEE Trans. Biomed. Eng.,* vol. 49, June, pp. 617-620.

Waite, A. D., 2005. *SONAR for Practising Engineers*, Hoboken, Wiley.

Ward, K. D., Baker, C. J., and Watts, S., 1990. "Maritime surveillance radar. I. Radar scattering from the oceansurface," *Radar and Signal Processing, IEE Proceedings F,* vol. 137, pp. 51-62.

Ward, K. D., R. J. A. Tough, P. W. Shepherd, 1997. "Modelling sea clutter: correlation, resolution and non-Gaussian statistics," in *Radar 97 (Conf. Publ. No.449)* IEEE, Edinburgh, UK, pp. 95-99.

Warnick, K. F. and Chew, W. C., 2001. "Numerical simulation methods for rough surface scattering," *Waves Random Media,* vol. 11, pp. R1-R30.

Watts, S., 1987. "Radar detection prediction in K-distributed sea clutter and thermal noise," *IEEE Trans. Aerosp. Electron. Syst.,* vol. 23, 1987, pp. 40-45.

Wiley, C. A., 1985. "Synthetic aperture radars," *IEEE Trans. Aerosp. Electron. Syst.,* vol. 21, May, pp. 440-443.

Williams, K. L., Jackson, D. R., Thorsos, E. I., Tang, D., and Briggs, K. B., 2002. "Acoustic backscattering experiments in a well characterized sand sediment: data/model comparisons using sediment fluid and biot models," *IEEE J. Ocean. Eng.,* vol. 27, July, pp. 376-387.

Williams, K. L., Kargl, S. G., Tang, D., Jackson, D. R., and Briggs, K. B., 2009. "Acoustic backscattering from a sand and a sand/mud environment: experiments and data/model comparisons," *IEEE J. Ocean. Eng.,* accepted.

Williams, K. L., Kargl, S. G., Thorsos, E. I., and Tang, D., 2005b. "Synthetic Aperture Sonar (SAS) imaging and acoustics scattering strength measurements during SAX04 (sediment acoustics experiment - 2004): experimental results and associated modeling," in *Boundary Influences In High Frequency, Shallow Water Acoustics*, N. G. Pace and P. Blondel, eds., University of Bath, UK.

Williams, K. L., Light, R. D., Miller, V. W., and Kenney, M. F., 2005a. "Bottom mounted rail system for Synthetic Aperture Sonar (SAS) imaging and acoustics scattering strength measurements: design/operation/preliminary results," in *UA Measurements: Technologies & Results* ed. J. S. Papadakis & L. Bjorno, Heraklion, Crete, Greece.

VITA

Shawn F. Johnson

Education

Ph.D in Acoustics	Pennsylvania State University, State College, PA	2009
MA in Acoustics & Audio	Johns Hopkins University, Baltimore, MD	2002
BM in Recording Arts & Sciences	Johns Hopkins University, Baltimore, MD	2002
BM in Trombone Performance	Johns Hopkins University, Baltimore, MD	2001
New York State Regents Diploma	Iroquois Central Schools, Elma, NY	1997

Work Experience

Graduate Research Assistant	Pennsylvania State University, State College, PA	2002-09
Summer Research Assistant	NATO Undersea Research Centre, La Spezia, Italy	2005
Acoustical Consultant	Acoustical Design Collaborative, Baltimore, MD	2001-02
Acoustics Graduate Assistant	Johns Hopkins University, Baltimore, MD	2001-02
Audio Engineer	Peabody Recording Studios, Baltimore, MD	1997-02
Engineering Assistant	Polk Audio, Baltimore, MD	2000-01
Audio Engineer / Broadcast Tech.	National Public Radio, Washington DC	1999-00

Selected Publications

S.F. Johnson, A.P. Lyons, & D.A. Abraham, *The impact of multipath on high-resolution SAS image statistics,* IEEE J. Ocean. Eng., submitted, 2009.

A.P. Lyons, S.F. Johnson, D.A. Abraham, & E. Pouliquen, *High-frequency envelope statistics of patchy seafloors*, IEEE J. Ocean. Eng., accepted, 2009.

S.F. Johnson, A.P. Lyons, & D.A. Abraham, *Dependence of Synthetic Aperture Sonar image statistics on resolution*, International Symposium on Underwater Reverberation and Clutter, Lerici, Italy, September 2008.

S.F. Johnson, A.P. Lyons, D.A. Abraham, E. Pouliquen, & L. Pautet, *Bandwidth dependence of high-frequency seafloor backscatter statistics*, Boundary influences in high frequency, shallow water acoustics, University of Bath, UK, 5-9 Sept 2005.

Awards

ASA Best Student Paper in Underwater Acoustics, 2nd Place, New Orleans, LA – 2007
Simowitz Memorial Citation for published research – 2006
National Defense Science and Engineering Graduate Fellowship – 2005-08
NATO Undersea Research Centre Research Assistant Programme – 2005
Chancellor's List / National Dean's List – 2007, 2006, 2005, 2000, 1999, 1998
ASA Best Student Paper in Underwater Acoustics, 2nd Place, NYC, NY – 2004
National Defense Industrial Association Fellowship – 2003-2004
National Scholars Honor Society; Lifetime Member